Universitat Politècnica de Catalunya
Departament de Física

Effects of Vibrations Applied To Fluids at Different Gravity Levels

by

Anna Garcia-Sabaté

A thesis submitted for the degree of Doctor of Philosophy in Applied Physics

Advisors:
Ricard González-Cinca
Francesc Suñol

Castelldefels, April 2016

Summary

Due to the increasing interest in space exploration, management of two-phase flows in the absence of gravity has become a key aspect in improving the efficiency of technological applications for space missions. Understanding of two-phase flows is essential in the development of future applications and for the improvement of existing ones, not only in microgravity, but also in hypergravity conditions.

In this thesis, the effects of external factors such as high and low frequency vibrations, or rotations on two-phase flows are addressed, when these systems are at different gravity levels. A series of experimental setups were developed in order to explore a wide range of phenomena occurring at different gravity levels.

The effects of pressure fields on micron-sized particles in the levitation plane of an acoustic field are discussed. Furthermore, an analysis of the motions of two isolated particles is provided and a method to determine the forces between them is presented. The method allows us to experimentally obtain the order of magnitude of the forces, as well as indirectly provide a measurement of the acoustic pressure inside a micro-channel.

Two microgravity experiments adapted to a sub-orbital vehicle were designed and built in order to examine the effects of low frequency vibrations and rotation in two-phase flows. This thesis will further analyse the effects observed in bubbles in different liquids. Bubble shape oscillations have been observed at low vibration frequencies, even though bubble dynamics are affected by the walls of the cell. After vibrations were turned off, the aspect ratio of a bubble in high viscosity fluid decays exponentially. Bubble break-up has been observed in the case of lower surface tension and lower viscosity.

Focusing on the distribution of the air bubbles during high and low rotation rates, an analysis is presented on the effects on a low surface tension fluid. An investigation is presented on the injection trajectory of bubbles during rotation showing a reasonable agreement with analytical predictions.

The detachment and rise of bubbles and bubble trains while an acoustic field is applied in hypergravity conditions are also addressed. Different effects have been observed in this experiment. Focusing on detachment, we provide an expression for estimating the detachment diameter when an acoustic field is applied. In addition, the effect of bubble trains on terminal velocity is discussed. A numerical analysis is also presented and compared to the experimental data.

Acknowledgments

The journey to complete this thesis began many years ago, while I was still pursuing my bachelor's. Through all these years I have crossed paths with many people, from whom I have learned a great deal.

First of all, I wish to thank my supervisor Dr. Ricard González-Cinca. I have considered him my mentor since my Bachelor's degree. Through all these years, he has helped me, supported and encouraged me. I am also very thankful for the opportunities he has given me, involving me in many amazing projects, and for all the advice and discussions. A big thank you goes to Dr. Francesc Suñol, my co-supervisor, who actually encouraged me to pursue a PhD when I was close to finishing my masters. Not only do I want to thank him for that, but also for all the discussions, explanations and even the side projects.

I would like to thank my external referees and panel members Dr. Catherine Colin, Dr. Veronique Roig and Dr. Laureano Ramírez for taking the time to review this thesis and for their useful comments and feedback.

Thanks also go out to Dr. Mauricio Hoyos for all the support during my stay at the *École Supérieure de Physique et de Chimie Industrielles de Paris*, for his kind hospitality and his help and many ideas, especially for the development of Chapter 2.

I would like to thank Dr. Dominique Legendre for taking me in at the *Institut de Mécanique des Fluides de Toulouse* (IMFT). His deep knowledge in Computational Fluid Dynamics has been of great help - it formed the foundation of the second half of Chapter 5. I would like to thank him for making my stay possible, rewarding and most of all, enjoyable.

I simply cannot pass up this opportunity to thank the members, current and past, from the Microgravity Laboratory, specially Dr. Francesc Suñol, Dr. Santiago Arias and Mr. Oscar Maldonado. It has been a pleasure to share lab, conferences and campaigns with you, and I am taking with me many good memories from these times. A shout out to the BOILUS Team members, for the hard work, the nice meals... and the fun and intense workshops and campaign!

A big thank you to Dr. Natacha Callens for the support in all the ESA Education projects I have participated in, as well as all the constructive comments, advice and conversations. I would also like to thank Mr. Paul de Leon and Mr. Jerry Larson, for their time, input and hard work to ensure the success of the sRLV experiments.

I studied my Bachelor's and Master's degrees at the same university (I've been there so long that the school has even changed names since I started), so I went from

attending lessons, to having an office next door to my professors, and I wish to deeply thank everyone who has helped me along the journey. To Dr. Josep Rojas I owe a lot more than he probably knows, since he was the one who took all the students from one of his classes to a conference about student parabolic flights. Which brings me to the Acoubus Team: Eloi Cortés, Edu Fortes and Jordi Bas, with whom I started this adventure, and from whom I learned and keep learning a lot.

There's a very important bunch of very nice people that I really want to thank, for making every day at the office more enjoyable, for all the lunches and dinners (and other special occasions), thank you Estel, Gabriela, Araceli, Ruxandra, Chaoren (a.k.a. Charlie), Maria, Milad, Enrique, Fuqiang, Shervin, Mitra, Isa, Roger, Luisfer, Siddharth, Quarentin, Thirza, Anne Marie and Ruxandra's plants. Really special mention to *fondo sur*, for many reasons you probably already know.

At the IMFT I felt extremely welcome from day one, and a huge part of that is thanks to the amazing people I shared my time (and office!) with: Esli, Sebastien, Shanti, Romain, Paul, Nico and José Carlos, among others. I would also like to thank the people who made my ESPCI stay memorable Adam, Thomas, Thomasz and Angelica.

I wish to thank Toni Castillo and Jordi Lino, for their help when it seemed that computers had given up on working. Aurora, who made every early morning more cheerful. Dr. Jordi Gutierrez, Dr. Pilar Gil, Lluís Monfort, Teresa Sanjose, Susana Izquierdo and Ana Maria Ortega, thank you for your support.

I wish to thank the founding members of SELGRA, it has been a very exciting and rewarding experience to undertake this project with such a nice team. Speaking of new projects, I would like to thank Carlos Ferraz, for his enthusiasm on pursuing all of those crazy ideas of ours, making them real and giving them life.

Many, many thanks to everyone who has been there for me along the way and whose names are not mentioned here, friends and relatives who have helped take stress off my shoulders time and time again. Special thanks to Bronagh for the final touches on the manuscript. Big thank you to Sandra, for all the conversations and discussions about work, and many other stuff, for your excitement, enthusiasm and *perspectives*, you have been a big part of this adventure.

Last, but definitely not least, I wish to thank my family (especially my mother, aunt and sister) and Nienhan, who have unconditionally supported me in many ways through thick and thin, with infinite patience. I really could not have done it without you.

I would like to acknowledge the financial support from *Agència de Gestió d'Ajuts Universitaris i de Recerca* under the FI-DGR 2013 pre-doctoral grant.

Contents

List of Figures

List of Tables

List of Symbols

Roman Symbols

A	Amplitude / Area of the cross-section of the bubble
a	Acceleration / parameter
a_c	Centrifugal acceleration
a_r	Radial acceleration
b	Parameter
C_d	Drag coefficient
c	Speed of sound / constant
d	Inter-particle distance / diameter / distance
d_b	Distance of separation between bubbles
d_C	Inner diameter of the nozzle
d_c	Critical distance
d_e	Detachment diameter
d_h	Horizontal diameter
d_M	Major diameter
d_m	Minor diameter
d_v	Vertical diameter
E_{ac}	Average acoustic energy
e	Parameter
F_C	Coriolis force
F_c	Centrifugal force
F_{Bj}	Bjerknes force
F_{By}	Buoyancy force
F_d	Drag force
F_i	Inertial force
F_m	Gas momentum force
F_p	Pressure force
F_{PB}	Primary Bjerknes force
F_r	Force between two spheres
F_{SB}	Secondary Bjerknes force
F_{xy}	Transverse force
F_z	Force on particles in the direction of propagation of the wave

F_σ	Surface tension force
f	Frequency
f_M	Minnaert's frequency
f_s	Vortex shedding frequency
G	Acoustic contrast factor
g	Gravity
i, j	Indices
k	Wavenumber
l	Length
m	Mass
m_l	Mass of the displaced liquid
n	Unit normal to the interface
P	Pressure
P_0	Atmospheric pressure
P_{ac}	Acoustic pressure amplitude
p	Parameter
p_0	Hydrostatic pressure
p_{ac}	Acoustic pressure at a given position and time
Q	Flow rate / Dummy variable
R	Radius of bubble, particle or LDC
r	Position / Polar coordinate / Roots
R_0	Equilibrium or resonance radius
T	Temperature / Period / Event time
t	Time
U	Flow velocity
u	Velocity
u_0	Velocity amplitude of the incident acoustic wave
V	Volume / Voltage
v	Velocity
v_r	Radial velocity
v_t	Terminal velocity
x, y, z	Cartesian coordinates

Greek Symbols

β	Compressibility / angle
γ	Polytropic index
δ_I	Dirac distribution
δ_v	Viscous penetration depth in the host liquid
ϵ	Aspect ratio
η	Dynamic viscosity
λ	Wavelength

ν	Kinematic viscosity
ρ	Density
σ	Surface tension
ϕ	Velocity potential
φ	Polar coordinate
ω	Angular frequency

Subscripts

0	Ambient / equilibrium / initial
a	Air
ac	Acoustic
avg	Average
Bj	Bjerknes
By	Buoyancy
b	Bubble
C	Coriolis / inner nozzle diameter
c	Critical
cd	Critical distance
d	Drag
f	Final
FG	Function generator
g	Gas
in	Incident acoustic wave
L	Lift
l	Liquid
OSC	Oscilloscope
p	Particle
$p-p$	Peak to peak
r	Resonance / Relative / Polar coordinate
v	Viscous / Vapour
x, y, z	Cartesian coordinates

Dimensionless Numbers

Ar	Archimedes number
Bo	Bond number
Re	Reynolds number
We	Weber number

List of Acronyms

ESA	European Space Agency
ESPCI	*Ecole Supérieure de Physique et de Chimie Industrielles de Paris*
ESTEC	European Space Research and Technology Center
IMFT	*Institut de Mécanique des Fluides de Toulouse*
IMU	Inertial Measurement Unit
ISS	International Space Station
JADIM	Numerical code developed at IMFT
LDC	Large Diameter Centrifuge
LED	Light-emitting diode
LES	Large-Eddy Simulation
NASA	National Aeronautics and Space Administration
PCB	Printed Circuit Board
PCM	Payload Command Module ®
PMMH	*Laboratoire de Physique et Mécanique des Milieux Hétèrogenes*
PTS	Payload Transportation System
PZT	Lead Zirconate Titantate Transducers
SBF	Secondary Bjerknes Force
SLx	SpaceLoft XL, launch number X (Mission name)
SSD	Solid-State Drive
SYT	Spin Your Thesis
UPC	*Universitat Politècnica de Catalunya*

Chapter 1

Introduction

Multiphase flows are the simultaneous flow of different phases (states of matter), i.e. gas, liquid and solid. Two-phase flows, which are a particular case of multiphase flows, are formally described as a fluid flow which includes two of the three phases. In this thesis, the effects of external factors on the particular cases of liquid-solid and liquid-gas combinations are studied.

Two phase flows, namely liquid and gas, are essential in many microgravity applications such as energy transfer, heat transfer or transport of contaminants in environmental systems. The use of two phase flows greatly reduces the weight of the systems containing them. Specifically in space applications, situations where two-phase flows are subject to vibrations, or where they need to be controlled, can occur at different gravity levels in different stages of spaceflight (g-jitter, engine restart, spin, stage separation, etc). These might negatively affect the correct operation of the systems in which two-phase flows are enclosed. Vibrations, either at high (>20 kHz) or at low (<20 kHz) frequency, as well as rotation, have significant effects on two-phase flows.

This thesis aims to improve the general understanding of the dynamics of two-phase flows when high and low frequency vibrations, as well as rotation are applied at different gravity levels and from microgravity to hypergravity.

1.1 Motivation

Research on space applications has become a very active field in recent years. With the current trend of public entities and private companies to pursue space exploration, it has become important to analyse many systems in order to increase their efficiency and ultimately reduce the total cost of space missions.

Space systems in which multiphase flows can be found encompass Environmental Control and Life Support Systems (ECLSS) (Carrasquillo (2005); Carter (2010)) as well as other systems like liquid fuel tanks (Chato (2007); Behruzi et al. (2011)).

ECLSS include wastewater treatment, thermal control or oxygen generation amongst others.

Particularly, liquid fuel (i.e. cryogenic propellant) was already a focus of research during the early days of space exploration. From the research carried out during the 1940s, it was discovered that a cryogenic propellant (liquid hydrogen) could provide a 40% increase in payload capability over other propellant combinations (Tomsik (2000)), and thus it was used in the Apollo programme. Furthermore, Abramson & Silverman (1966) compiled a review of the research on the motion of propellants and other liquids contained in launch vehicles, discussing effects such as sloshing, vertical excitation and rotation.

Knowing the dynamics of two-phase flows at different stages of the mission, as well as knowing how to efficiently control one phase is critical. For example, on the ground, because of gravity, liquid and gas separate into two well defined layers: the liquid phase (denser) locates below the gas phase. However, in space this is not the case, as gas and liquid are mixed without any particular preferred position of either phase.

Acoustic fields have been proven to be an efficient method for controlling bubble dynamics (Leighton (1994); Abe et al. (2002); Fan & Cui (2005)). The study of acoustic forces has greatly been advanced recently due to the increasing number of applications, not only for space, but also for acoustically manipulating objects (acoustic separation of different species (Benes et al. (2001); Woodside et al. (1997)), acoustic levitation (Xie et al. (2006); Collas et al. (1989)) or contactless positioning), manipulation of drops and bubbles, and management of fluids in low gravity (Gao (1999)).

Furthermore, acoustic fields can be used in a wide variety of applications on the ground. For example, due to the use of ultrasound imaging in medicine being very extensive nowadays, there is considerable interest in the investigation of microbubbles as contrast agents (Calliada et al. (1998)) to obtain high contrast ultrasound images, and thus allowing for higher definition of images. The use of microbubbles and acoustics for drug delivery is also an emerging field (Tsutsui et al. (2004); Lum et al. (2006)).

Experiments on different phenomena are investigated in this thesis. First, the effects of acoustic fields on micro-particles (liquid-solid) are studied. Since an acoustic field can be a means to levitate a particle (and thus having simulated microgravity on ground), its effects on the plane of levitation need to be understood. Secondly, the effects of low frequency vibrations and rotation in microgravity in liquid-gas are studied, as these are external factors commonly found in spaceflight. Finally, the effects of acoustic fields on rising bubbles (liquid-gas) in gravity levels higher than $g_0 = 9.81$ m/s^2 are addressed. This is because physical phenomena in hypergravity are not fully understood, even though two-phase space systems are consistently subject to gravity levels different than microgravity.

1.2 Acoustic Forces

A standing wave is the sum of two travelling waves going in opposite directions. Figure 1.1 shows the sum of two travelling waves at different times during half a period ($T/2$), showing that only certain points always remain zero, i.e. the nodes. The positions of the wave that reach maximum amplitudes are called antinodes.

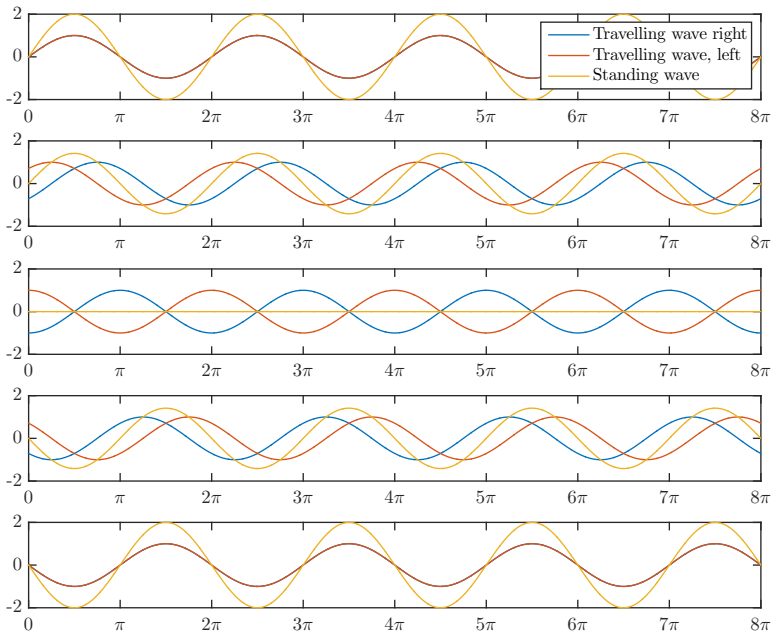

Figure 1.1: Two travelling waves at different times, and its sum, which corresponds to a standing wave.

Almost two centuries ago, Faraday pointed out that particles and bubbles undergo different forces when an acoustic field is applied (Faraday, 1831). Since then many studies have been carried out involving different aspects of this phenomenon, such as the observation of particle aggregation (Kundt & Lehmann, 1874), early theoretical analysis (Rayleigh, 1884), mathematical analysis of pulsating air bubbles (Bjerknes, 1904), or the development of a rigorous analytical expression for the acoustic radiation pressure on spheres (King, 1934). Except for Bjerknes' work, these investigations were mainly focused on the effects of the primary sound field on spherical objects without analysing any secondary forces. More recently research on secondary forces has been reported. Pioneering studies on the interaction forces between particles in an acoustic field were carried out, focusing on rigid spheres (Ny-

borg & Gershoy, 1973), and on bubbles (secondary Bjerknes force) (Crum, 1975).

Research on bubbles and solid particles in acoustic fields developed in parallel for an extensive period of time. Weiser et al. (1984) contributed to the field of interparticle forces by taking into consideration for the first time the secondary Bjerknes force in the study of the interaction between two compressible solid spheres. Ever since, many authors such as (Doinikov, 1999), (Pelekasis et al., 2004), (Yamakoshi & Koganezawa, 2005), (Yasui et al., 2008) or (Rabaud et al., 2011), have studied both experimentally and theoretically, the secondary Bjerknes force on bubbles. Although some research works on secondary forces on particles have been reported (Woodside et al., 1997; Benes et al., 2001), the magnitude of these forces has not been determined experimentally.

The force generated by an external acoustic field acting on drops, bubbles or particles, without considering the interaction between neighbouring objects, is known as the primary acoustic force. Yosioka & Kawasima (1955) and Gor'kov (1962) calculated the acoustic radiation pressure on a compressible sphere giving rise to the primary acoustic force for plane standing waves. In the direction of propagation of the wave, this force is given by

$$F_z = -\frac{4}{3}\pi R^3 E_{ac} k G \sin(2kz), \tag{1.1}$$

where R is the radius, E_{ac} is the average acoustic energy density (sum of the time-averaged kinetic and potential energy densities), k is the wave number, z is the distance from the nearest pressure antinode, and G is the acoustic contrast factor defined as

$$G = 1 - \frac{\beta_p}{\beta_l} + \frac{3(\rho_p - \rho_l)}{2\rho_p + \rho_l}, \tag{1.2}$$

where β is the compressibility, ρ is the density and subscripts p and l correspond to particle and liquid, respectively. For $G < 0$ (generally the case of gas bubbles), particles move to the pressure antinodes by the action of the primary acoustic force. However, if particles are denser than the surrounding fluid ($G > 0$), they are driven to the pressure nodes.

Standing waves with a non-uniform amplitude (due to diffraction effects or non-uniform performance of the transducer) generate energy gradients in the system which affect the movement of particles in a levitation plane perpendicular to the direction of propagation of the wave. In this case, a transverse component of the primary acoustic force has to be considered (Gor'kov, 1962),

$$F_{xy} = \frac{4}{3}\pi R^3 \nabla E_{ac} \left(\frac{3(\rho_p - \rho_l)}{2\rho_p + \rho_l} \cos^2(kz) - \left(1 - \frac{\beta_p}{\beta_l}\right) \sin^2(kz) \right). \tag{1.3}$$

The transverse component of the primary acoustic force moves particles towards the regions of maximum acoustic energy. Given that the axial component scales

with E_{ac} and the transverse component scales with the gradient of E_{ac}, the axial component is often at least one order of magnitude larger than the transverse one.

The research regarding acoustic forces on bubbles started to gain momentum in the early 20th century. C.A. Bjerknes and his son V.F.K. Bjerknes carried out a mathematical analysis of pulsating air bubbles in stationary sound fields (Bjerknes (1904)). They described two forces (usually named after these two Norwegian scientists): the first one being the tendency of a bubble to move towards or away the pressure antinode (primary Bjerknes force), and the second one the mutual attraction or repulsion between air bubbles (secondary Bjerknes force). The general expression of the Bjerknes force is

$$F_{Bj} = -\langle V(t)\nabla p_{ac}(r,t)\rangle, \tag{1.4}$$

where $\langle\cdot\rangle$ denotes average over a cycle, $V(t)$ is the time-dependent volume of the bubble and $p_{ac}(r,t)$ is the acoustic pressure at a given position r and time t. One might consider that the resulting force should be zero because it is the average over a cycle. However, over a cycle, the bubble size undergoes non-linear oscillations (following the Rayleigh-Plesset equation) and thus the net force on the bubble (dependent on the radius) averaged over a cycle is not zero (Leighton (1994)). If the field considered in p_{ac} is the one generated by the incident acoustic wave, the primary Bjerknes force (F_{PB}) will be obtained. Furthermore, if the field in p_{ac} is the one generated by a pulsating bubble, then the resulting force will be the secondary Bjerknes force (F_{SB}).

Equation 1.4 assumes a spherical, small bubble compared to the wavelength of the sound field, and surrounded by an ideal liquid (non-viscous and non-heat-conducting). The centroid of the bubble is located at position r at time t and spatial change of ∇p_{ac} within the volume of the bubble is negligible because of its size.

A bubble of a certain size immersed in a liquid will have a resonance which is defined by the Minnaert resonance frequency f_M,

$$f_M = \frac{1}{\pi d_0}\sqrt{\frac{3\gamma p_0}{\rho_l}}, \tag{1.5}$$

where d_0 is the equilibrium diameter of the bubble, p_0 is the hydrostatic pressure outside the bubble, ρ_l is the liquid density and γ is the polytropic index for adiabatic conditions (for air $\gamma = 1.4$).

Equation 1.5 is essential to the study of the dynamics of the bubbles in acoustic fields. Depending on the equilibrium radius R_0 of the bubble with respect to the resonance radius R_M that would correspond to the frequency applied, the bubble will tend to go to the pressure nodes ($R_0 > R_M$) or antinodes ($R_0 < R_M$) of the standing wave field.

Take the case of a bubble larger than the resonance radius. If the bubble was initially located in the pressure antinode, its position is that of unstable equilibrium.

Any slight variation from its initial position will make it move towards the pressure node, due to the primary Bjerknes force. The opposite can be considered for bubbles smaller than the resonance radius.

Leighton (1994) derived an expression of the primary Bjerknes force for small amplitude variations of the bubble radius, which is also valid for any field containing a pressure gradient.

$$F_{PB} = F_{Bj} = -\frac{4\pi k R_0 P_{ac}^2 \sin(2ky)}{\rho_l} \frac{\omega_0^2 - \omega^2}{(\omega_0^2 - \omega^2)^2 + (2\beta_{tot}\omega)^2}, \tag{1.6}$$

where P_{ac} is the acoustic pressure amplitude, $k = \omega/c$ is the wavenumber (c is the speed of sound in the medium), y is the position in the axis of propagation of the field, ω is the angular frequency of the incident field, $\omega_0 (= 2\pi f_M)$ is the resonance angular frequency of the bubble with equilibrium radius R_0 as obtained from equation 1.5 and β_{tot} is the total resistive constant leading to damping. For the cases discussed in this thesis, it is considered that $\beta_{tot} \ll \omega$ therefore the term $2\beta_{tot}\omega$ in equation 1.6 can be neglected (Eller (1968)), which, for bubbles larger than resonance (i.e. $\omega_0 < \omega$), leads to

$$F_{PB} = -\frac{4\pi k R_0 P_{ac}^2 \sin(2ky)}{\rho_l} \frac{1}{\omega_0^2 - \omega^2}, \tag{1.7}$$

and for bubbles smaller than resonance (i.e. $\omega_0 > \omega$) equation 1.7 drops the negative sign. As stated in Leighton (1994) this force is treated as uni-axial, so that the vector of the force is included into the sign of F_{PB}.

Pulsating bubbles generate a secondary acoustic field which makes bubbles attract or repel each other. Expressions for the secondary Bjerknes force are usually given as a function of the change in volume of the particle or bubble (Crum, 1975; Weiser et al., 1984; Andersen et al., 2009), which can be difficult to estimate. An alternative expression considering the compressibility of the spheres can be written as (Apfel, 1988)

$$F_{SB} = -\frac{2\pi\rho_l}{9}(\beta_l \omega P_{ac})^2 \left(1 - \frac{\beta_{p1}}{\beta_l}\right)\left(1 - \frac{\beta_{p2}}{\beta_l}\right)\frac{R_{p1}^3 R_{p2}^3}{d^2} \tag{1.8}$$

where R_{p1} and R_{p2} denote the radius of each particle taking part in the process, and d is the inter-particle distance.

The interaction force between two rigid spheres oscillating in an acoustic field can also be considered. Two different expressions for this force are given in Weiser et al. (1984) depending on the angle between the straight line connecting the particles and the direction of the propagating field. The force between two spheres with equal radius lined up in the direction of propagation of the sound field is repulsive and given by

$$F_r = \frac{4\pi(\rho_p - \rho_l)^2 v_{ac}^2 R_p^6}{3\rho_l d^4}, \tag{1.9}$$

where v_{ac} is the velocity (assumed uniform) of the incident acoustic wave at the position of the spheres. When particles are lined up perpendicular to the wave propagation, the force is attractive and given by

$$F_r = -\frac{2\pi(\rho_p - \rho_l)^2 v_{ac}^2 R_p^6}{3\rho_l d^4}. \tag{1.10}$$

When an acoustic wave is present in the medium, acoustic streaming may occur. Acoustic streaming is a flow of the liquid due to the incident acoustic field and in the direction of the acoustic field (Leighton (1994)). Therefore, it is important to consider whether acoustic streaming effects can be neglected in the studied cases. To do so, the bubble equilibrium radius needs to be compared to the viscous penetration depth in the host liquid δ_v, where $\delta_v = \sqrt{2\nu/\omega}$ (ν is the kinematic viscosity). If $R_0 \gg \delta_v$, then acoustic streaming can be ignored. For the experiments carried out at 2.8 MHz the viscous penetration depth order of magnitude is $\mathrm{O}(\delta_v) \simeq 10^{-7}$ m, the smallest particle radius was 2.5 µm, and thus acoustic streaming effects on this experiment are negligible. In the case of the experiments carried out at frequencies of 53 kHz and 60 kHz, the viscous penetration depth order of magnitude is $\mathrm{O}(\delta_v) \simeq 10^{-6}$ m, and the injected bubbles radius are 0.45 mm $< R_0 <$ 0.75 mm. Thus, acoustic streaming can be neglected for the experiments presented in this thesis.

1.3 Low Frequency Vibrations

Vibrations under microgravity conditions change the dynamics of the two-phase flows. Research on common effects during spaceflight such as g-jitter (Monti et al. (1997)) or sloshing (Utsumi (2000); Veldman et al. (2007); Pal (2009)) has been previously carried out. However, to better understand phenomena occurring in these cases, it is important to understand how controlled and random vibrations affect two-phase flows. Many studies have provided numerical results (Marston (1980); Straube et al. (2006); Shklyaev & Straube (2009)), and also experimental results of vibrations on the ground (Risso & Fabre (1998); Zoueshtiagh et al. (2006); Kim et al. (2013)), and in microgravity (Falcon et al. (1999); Beysens (2004); Farris et al. (2004); Yoshikawa et al. (2010)).

The processes undergone by bubbles under such external conditions (e.g. g-jitter, sloshing) are diverse, some of the effects which have been reported include: wall attraction/repulsion, shape oscillations or break-up. Beysens (2004) observed heterogeneities perpendicularly to the direction of vibration, specifically wall attraction and deformation of an H_2 bubble vibrated at $f = 20$ Hz. The motion of bubbles under sinusoidal vibrations in microgravity was also investigated by Farris et al.

(2004), displaying a strong wall effect and that the ratio between displacement of the bubble and the displacement of the container is independent from the container's displacement amplitude. Different mechanisms of detachment from vibrating walls have been reported by Kim et al. (2013) who also observed surface modes (i.e. regular reproducible shapes) on bubbles depending on the vibration.

Deformation of bubbles adopting regular shapes has been previously observed. Surface modes have been reported when applying high frequency oscillations (ultrasound) (Leighton (1994); Trinh et al. (1998); Versluis et al. (2010); Sommers & Foster (2012)) or under the presence of a turbulent flow (Risso & Fabre (1998)). Furthermore, break-up of vibrated bubbles has formerly been described (Risso & Fabre (1998); Zoueshtiagh et al. (2006); Yoshikawa et al. (2010)).

1.4 Rotation

Experiments on the equilibrium of liquid rotating, held together by capillary tension were first reported by Plateau (1857). Subsequenly, Rayleigh (1914) discussed the dynamics of an infinite mass of liquid. Rayleigh showed that a bubble flattens under the effects of rotation, while when there is no rotation and in the absence of gravity, the bubble is spherical.

In some stages of a spaceflight rotation can occur, for instance due to the ballistic phase of a rocket. The effects of rotation on two phase flows should then be taken into account. Rotating liquids have been studied in the past with different focuses. Rosenthal (1962) considered the shape stability of a bubble on the axis of rotation, with the aim of using this method to study the surface tension of the liquid. Siekmann & Johann (1976) analyzed the motion of bubbles under simulated weightlessness in a rotating system, obtaining analytical expressions for their motion. Trajectories and drag forces were studied consequently by Annamalai (1982), Ruggles et al. (1988) or Rastello et al. (2011).

Moreover, since the early days of space exploration, a number of studies has focused on slosh and rotation on space applications (Abramson & Silverman (1966); Hung & Long (1995); Behruzi et al. (2011), that specifically aim to acquire a better understanding of the behaviour of fluids inside liquid fuel tanks.

1.5 Microgravity and Hypergravity Platforms

Microgravity, also referred as weightlessness, is the state in which the gravitational force is the only one acting on a body. Whenever an object is in free fall, microgravity conditions can be achieved. An object falling on ground or in space experience the same acceleration. In space, an astronaut in the space station is falling at the same rate as the station itself and thus it appears that the astronaut is floating in a microgravity environment.

There are currently different platforms that provide microgravity conditions, and each of them allow different experimental durations and quality of microgravity. Sabbatini (2014) provides a concise review of the different available platforms and their characteristics.

Orbital platforms (e.g. ISS) provide ideal conditions for experimentation because they offer the best quality ($10^{-4}g_0$ to $10^{-6}g_0$) and longest duration. However, access to these platforms is expensive and the preparation of experimental setups is arduous and complex. If the payload is on the ISS, astronauts can interact with it. Typically, telemetry is used to send and receive data. Still, payloads for these platforms should be mostly autonomous.

Other platforms, that are generally referred to as "on-ground platforms", offer similar conditions and are more accessible. Parabolic flights use an adapted aircraft that follows a series of parabolas (usually around 31 per flight and each campaign has typically three flights), offering about 22 s of reduced gravity ($10^{-2}g_0 \sim 10^{-3}g_0$) during each parabola. Experiments on parabolic flights do not need to be fully automatised, since researchers can also be on the aircraft and can actively interact with their experimental setup. The advantage of parabolic flights is that larger payloads can be loaded onto the aircraft and they allow for a wider range of fields of experimentation, as this is the only sub-orbital platform where human research can be performed.

Drop towers also provide microgravity conditions, by letting experiments fall from a certain altitude. Taking the ZARM drop tower (Bremen, Germany) as an example, it can offer $10^{-6}g_0$ up to about 10 s. To emulate these conditions, all the air in the chamber is evacuated (thus eliminating drag and friction forces) then the payload is dropped from the top of the chamber. Experiments can weigh up to 264 kg and approximately 400 drops per year are carried out. The experiments should be fully automatised, however the experimental setup can be adjusted between each drop.

Finally, sounding rockets describe a parabolic trajectory that reaches altitudes above 80 km, but does not go into orbit, hence they carry out sub-orbital trajectories. Sounding rockets (which means "to take measurements" from the nautical term "to sound") have been used for research of the upper atmosphere for years. However, they also offer conditions of microgravity ($10^{-3}g_0 \sim 10^{-6}g_0$) during the top part of the parabolic flight profile, for 3 to 13 min depending on the rocket. Experiments for such platforms should be as lightweight as possible (10 to 20 kg for small rockets, 260 to 480 kg for larger rockets) and fully automatised. They have telemetry capabilities, i.e. signals to activate the experiments can usually be sent from the ground segment and data can be received from the experiment.

Sometimes sounding rockets are included in the sub-orbital reusable launch vehicle category (sRLV) because part of the rocket can be reused. These vehicles do not go into orbit either and can be fully or partially reused. Even though UP Aerospace's SpaceLoft XL and Masten Space Systems's Xaero and Xombie are already opera-

tional, most sRLV are currently under development e.g. Virgin Galactic's SpaceShipTwo or SpaceX's Falcon-9R. Reusable vehicles can offer microgravity conditions similar to sounding rockets and can be launched several times per year. Access to sRLV can be achieved, for example, through the NASA Flight Opportunities Program. The weight restriction for the payloads can be larger than some sounding rockets and should also be fully automatised. Except in the case of SpaceShipTwo, when exceptionally a researcher can be in the vehicle actively interacting with the experiment or even performing human research.

One option to obtain hypergravity conditions is just before and after the 20 s of microgravity in a parabolic flight, which reaches gravity levels between $1.5g_0 \sim 1.8g_0$. Yet, it is not possible to reach higher gravity levels on this platform. Platforms that allow controlled hypergravity conditions are centrifuges. A centrifuge generates a force by rotating around a fixed axis and this centrifugal force can be adjusted by controlling the angular velocity of the centrifuge. The Large Diameter Centrifuge (LDC) in ESA-ESTEC facilities (Noordwijk, The Netherlands) reaches gravity levels up to $20g_0$. It has a diameter of 8 m and it can run experiments for as long as six months (provided they do not exceed 80 kg) (Sabbatini (2014)).

Effects of vibrations at different gravity levels in two-phase flows phenomena are studied and discussed in this thesis. Platforms that offer microgravity and hypergravity conditions were thus required. Specifically, results in microgravity were obtained on small sounding rockets, providing $\sim 10^{-3}g_0$ for almost 4 minutes. Hypergravity conditions were obtained at the LDC, were gravity levels from $2g_0$ to $\sim 20g_0$ were explored. Typical times to prepare payloads for these platforms vary between 6 to 12 months.

1.6 Objectives

The main objective of this thesis is to strengthen the current knowledge on two-phase flows at different gravity levels under the effects of external vibrations and rotation. In particular, the goals of this theses are to:

- Experimentally determine the magnitude of the forces acting on particles on the levitation plane of an acoustic field on the ground.
- Design, build, automatise and test laboratory experimental setups to fit in a sounding rocket to perform experiments in microgravity.
- Analyse the effects of low frequency vibrations on two-phase flows with different physical properties in low gravity conditions.
- Investigate the behaviour of two-phase flows in a rotating body during microgravity.

- Measure and analyse the effects generated by an acoustic field of high frequency on the detachment and rise of bubbles in hypergravity.
- Perform numerical simulations on the interaction of an acoustic field with a rising bubble and to compare them to the experimental results.

1.7 Manuscript Outline

This thesis has been divided in three main chapters covering ground experiments, microgravity experiments and hypergravity experiments. Each chapter contains an introduction to the phenomena studied and a description of the experimental setup used for each platform.

Chapter 2 discusses the experimental results on particles in micro-channels while applying an acoustic field. The effects on forces acting on the levitation plane are discussed.

In Chapter 3 the results on low frequency (30 - 50 Hz) vibrations applied on two-phase flows with different physical properties in microgravity are discussed.

Chapter 4 presents the effects of rotating fluids at high and low velocity on a low surface tension liquid in microgravity.

Chapter 5 is focused on hypergravity experiments, mainly on the effects of acoustic fields on injected rising bubbles. An analysis of the experimental data is carried out and is complemented by a numerical analysis in Section 5.6.

Finally, in Chapter 6 a summary of the main conclusions of each chapter is presented. Difficulties that were encountered during the development of the thesis are reviewed. As well as a series of recommendations, work currently being carried out and future work are addressed.

Chapter 2

Elastic Particle Interaction in an Acoustic Field

In this chapter we will focus on ground experiments, specifically on micro-particles, presenting a method for the experimental determination of inter-particle forces (secondary Bjerknes force) generated by the action of an acoustic field in a resonator micro-channel (Garcia-Sabaté et al. (2014)). The acoustic radiation force created by an ultrasonic standing wave moves suspended particles towards the pressure nodes and the acoustic pressure induces particle volume oscillations. Once particles are in the levitation plane, transverse and secondary Bjerknes forces become significant. Experiments were carried out in a resonator filled with a suspension composed of water and latex particles of different sizes (5-15 μm), at different concentrations. Ultrasound was generated by means of a 2.5 MHz nominal frequency transducer. We show the results of the measured forces and the critical interaction distance for various cases. Inter-particle forces of the order of 10^{-14} N have been measured by using this method.

2.1 Background

Considering the introduction to the acoustic forces in Section 1.2, the forces acting on a particle in an acoustic field are illustrated in Figure 2.1. Axial and transverse forces from a standing wave generated by a transducer can be distinguished in Figure 2.1, as well as secondary forces.

Table 2.1 shows the orders of magnitude of these forces considering polystyrene ($\rho_p = 1056$ kg/m^3, $\beta_p = 1.71\times10^{-10}$ Pa^{-1}) particles of 10 μm diameter in water ($\rho_l = 1000$ kg/m^3, $\beta_l = 7.21\times10^{-6}$ Pa^{-1}) and a frequency of 2.830 MHz. The axial and transverse acoustic forces shown were obtained for a setup with similar conditions in Woodside et al. (1997) considering $E_{ac} = 18$ J/m^3. We have used this value of the acoustic energy to estimate F_r, F_{PB} and F_{SB}. In addition, in order to determine F_{PB}

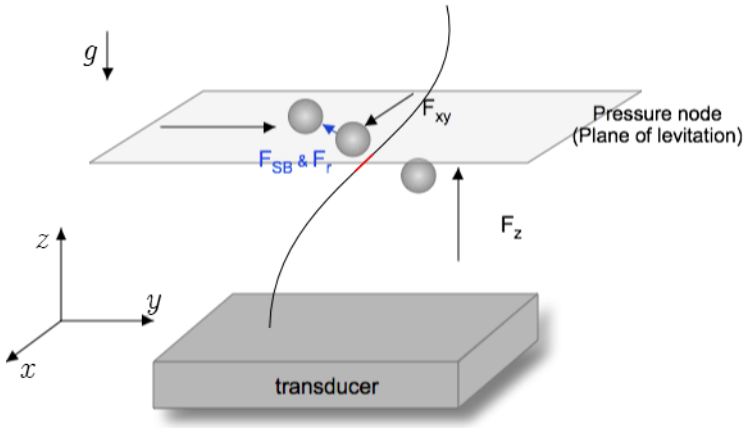

Figure 2.1: Acoustic forces acting on a pair of particles.

	Force	Plane of Action	Described for	Magnitude (N)
Primary Acoustic Field	Axial Acoustic Force F_z	Axial	Particles	10^{-11}
	Primary Bjerknes Force F_{PB}	Axial	Bubbles	10^{-5}
	Transverse Acoustic Force F_{xy}	Transversal	Particles	10^{-13}
Secondary Acoustic Field	Secondary Bjerknes Force F_{SB}	Transversal	Particles and Bubbles	$10^{-13}/10^{-5}$
	Force Between Two Rigid Spheres F_r	Transversal	Particles	10^{-14}

Table 2.1: Orders of magnitude of the acoustic forces acting on a pair of particles/bubbles of radius $R = 5\mu$m separated 20 µm.

and F_{SB} the following expression for the acoustic pressure has been used (Andersen et al. (2009)):

$$P_a = c\sqrt{4\rho_l E_{ac}}, \tag{2.1}$$

where c is the speed of sound in the fluid and ρ_l is the the density of the medium. Finally, the relation $E_{ac} = (\rho_l v_{ac}^2)/2$ is used to obtain $v_{ac} = 18.9$ cm/s in order to determine F_r.

The main objective of the work presented in this chapter is to experimentally obtain the magnitude of the forces that arise between solid micro-particles, when an acoustic field is applied. In Section 2.2 and 2.3 we present the experimental setup and the procedure used to perform these experiments. The data analysis technique

to determine the magnitude of the inter-particle forces is detailed in Section 2.4, as well as the results obtained from the study of different cases with particular characteristics. Finally, the main conclusions from this chapter are presented in Section 2.5.

2.2 Experimental Setup

A schematic of the experimental setup is shown in Figure 2.2. Experiments were carried out in a Hele-Shaw cell with an inner channel of thickness 250 μm. Its top view dimensions were 42 mm × 10 mm. The cell is a resonator made of a glass plate separated from a stainless steel plate by means of Mylar spacers. A rectangular (10 mm × 20 mm × 560 μm) piezoelectric transducer (PZ27 Ferroperm Piezoceramics, Denmark) with a nominal frequency of 2.5 MHz was glued with conductive epoxy (Chemtronics ITW, USA) to the stainless steel plate. The transducer was excited in each test by a function generator (Tabor Electronics WW1072, Israel) whose signal was amplified by a voltage amplifier (Tabor Electronics 9250, Israel) with 10× fixed gain, which was also connected to a digital oscilloscope (ISO-TECH IDS 8064, Hanan-Israel). A pressure node was created approximately at the center of the channel. The channel was observed through a reflective microscope (Zeiss Axiotech Vario 100HD), using 50× (Olympus SLMPlan) and 20× (PL Nachet LD) objectives. A camera (Moticam 2000) was mounted on the microscope through a 0.5× objective and connected to a computer, which recorded videos between 5 and 26.7 fps.

2.2.1 Test Cell

The experiments to be performed required a test cell in which the behaviour of the flow could be known and predicted. This condition could be achieved by using a channel whose flow would behave as a Hele-Shaw flow. A Hele-Shaw flow is a low Reynolds number flow ($\mathrm{Re} \ll 1$), which means that viscous forces are dominant compared to inertial forces, and thus a laminar flow will exist all along the cavity. This situation occurs when a flow fills a narrow gap existing between two parallel plates, whose thickness is considerably smaller than the length or the width.

It had to be taken into account that each material has a different reflection or transmission coefficient. Hence, calculating the resonance frequency become too complex, and the resonance of the channel had to be experimentally determined.

The cell used to carry out the experiments was manufactured in the laboratory. The channel was built by mounting layers of different materials one over the other. The lower layer was a stainless steel plate where two holes had been drilled, to be used as inlet and outlet of the channel. On the metal plate there was a layer of Mylar of 250 μm which had been carefully glued with neoprene glue. The desired shape of the cell was cut off the Mylar. Finally, a glass was glued at the top so that the inner part of the channel was visible through a microscope.

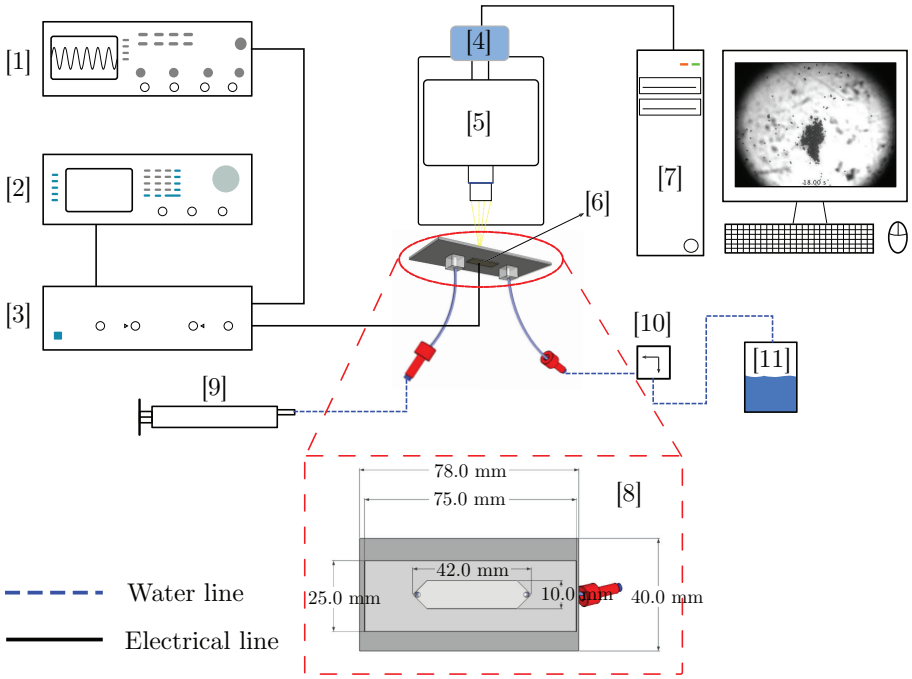

Figure 2.2: Experimental setup. [1] Oscilloscope, [2] function generator, [3] amplifier, [4] camera, [5] microscope, [6] PZT, [7] PC, [8] microchannel, [9] syringe, [10] two-way valve and [11] waste flask

At the end of the process, the total inner thickness of the channel resulted in 250 µm. Once the glue has dried, several tests were performed in order to ensure that no leaks existed in the channel.

2.2.2 Transducer

Below the metallic plate, a squared piezoelectric transducer was glued. The transducer had two electrodes, one on each side. Electrically exciting the transducer, resulted in mechanical motion generating the acoustic wave desired.

The transducer was glued with conductive epoxy to the metallic layer of the channel and two cables were soldered. The first one on the visible electrode of the transducer. The second one was glued with conductive epoxy on the metallic plate.

The transducer was 10 mm x 20 mm, and 84 µm thickness. It had a nominal frequency of 2.5 MHz, which was the optimal frequency for the transducer to work, and it was close to the resonance frequencies required for the test cell.

2.3 Experimental Procedure

A solution of water and latex particles was injected in the channel by means of a syringe. A two-way valve was placed at the cell outlet to ensure stationary conditions inside the cell during the experiments, and to flush the suspension to a waste flask after each test. The channel was initially cleaned with a solution of soap and deionised water. In special cases, when a more thorough cleaning was needed, ethanol 76% was injected. Deionised water was used to rinse and fill up the channel. Once the channel was full of water, the resonance frequency of the system was determined. Figure 2.3 shows the amplitude obtained at different frequencies between 2.0 and 3.5 MHz (where V_{osc} is the voltage measured by the oscilloscope, and V_{FG} is the voltage at the output of the amplifier). The highest peak corresponds to the resonance frequency, which is the optimal one to levitate particles, although it is not necessarily the optimal one for aggregation.

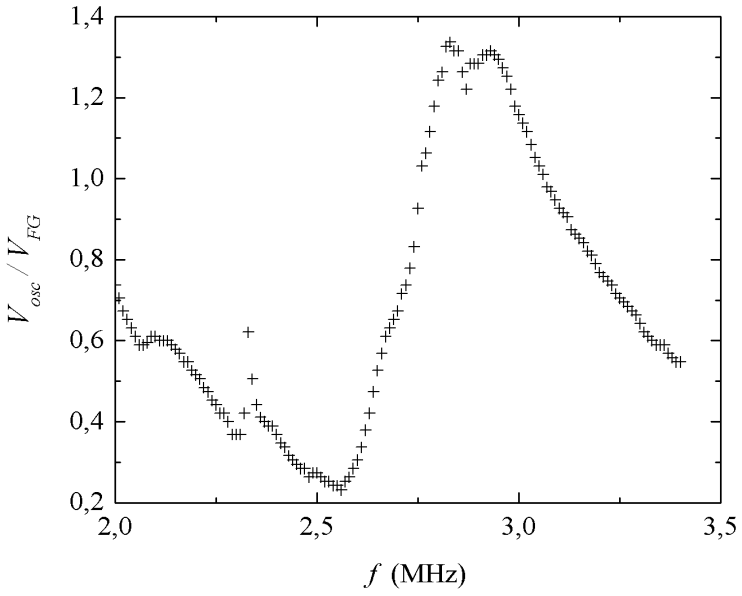

Figure 2.3: Amplitude response of the transducer at different frequencies.

Monodisperse latex beads (Micromod - Rostock, Warnemunde Germany) of different diameter (5, 7, 10 and 15 μm) were diluted in deionised water at different concentrations and injected into the channel. Once particles were injected, the two way valve was closed and particles were let to sediment for some minutes. Afterwards, the ultrasound generation system was turned on at the desired frequency and

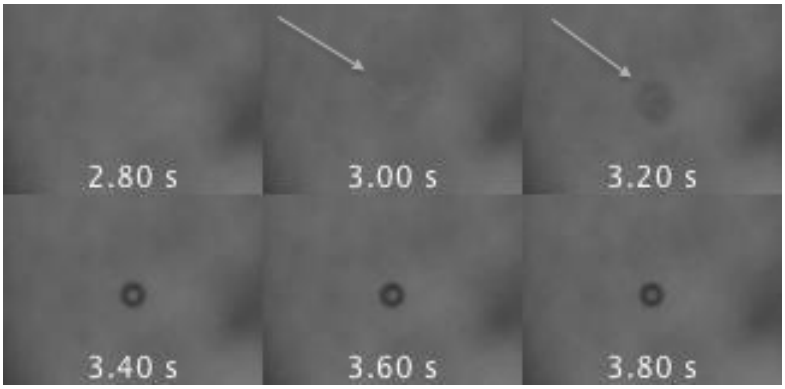

Figure 2.4: Particle levitation due to the axial force.

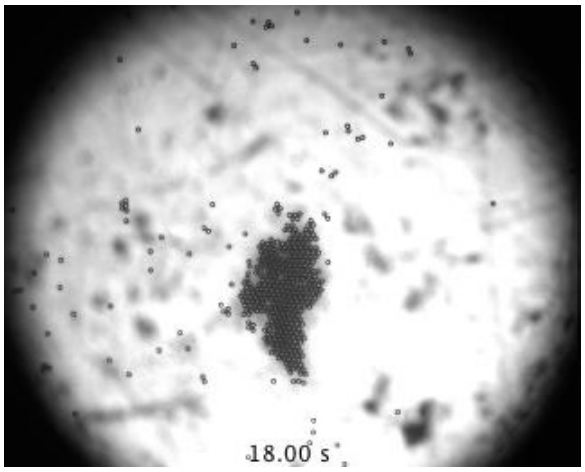

Figure 2.5: Particle aggregation at the plane of levitation due to transverse forces.

videos were recorded by the camera through the microscope.

Figure 2.4 illustrates the particle movement towards the plane of levitation due to the action of the acoustic axial force when the ultrasound generation system is turned on. Once in this plane, particles tend to form aggregates under the action of transverse forces (Figure 2.5).

The films recorded in each test were saved in grayscale and processed by means of the open-source software Fiji (ImageJ) (Schindelin et al., 2012). In order to obtain the position of the particles at each frame, we used the plug-in MTrack2. This plug-in needs a threshold stack to properly track the particles, hence it was necessary to process the video before using the tracking plugin. A z-projection of the maximum intensity pixels was obtained and subtracted from the entire stack

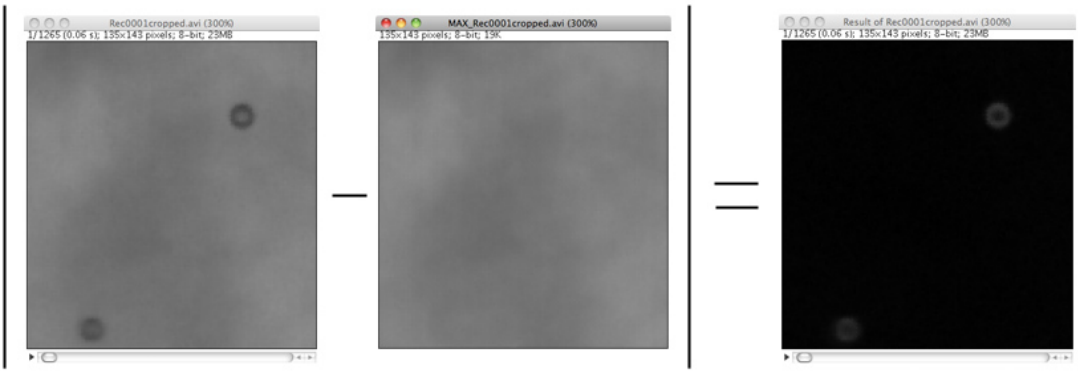

Figure 2.6: Resulting stack from the image calculator.

using the image calculator (Figure 2.6). A threshold stack was obtained and used for tracking the position of the particles frame by frame.

2.4 Results

2.4.1 Data Analysis Method

More than 100 films were recorded by the camera, 9 of which containing analysable cases. These cases (17 in total) show two particles approaching each other in the levitation plane due to the effects of the transverse acoustic force and the secondary Bjerknes force. The low number of analysable cases can be explained by the fact that the secondary Bjerknes force is considerably weaker than the transverse acoustic force. Thus, the cases where the effects of the secondary Bjerknes force can be observed are difficult to identify. In addition, the field of view of the microscope through which the channel was observed only allowed the observation of a limited number of cases.

F_{SB} could not be measured directly since direct measurements of the acoustic pressure inside the channel cannot be made. Therefore, an indirect method based on the balance of forces acting on a particle in the plane of levitation was considered. The force balance can be expressed as

$$\left(\rho_p V_0 + \frac{\rho_l V_0}{2}\right) \frac{dv}{dt} = F_{xy} + F_d + F_{SB}, \tag{2.2}$$

where V_0 is the static particle volume, v is the particle velocity, and F_d is the drag force. Since the Reynolds number in the channel is small, Stokes' drag can be considered,

$$F_d = -6\pi\eta R v, \tag{2.3}$$

where η is the dynamic viscosity.

Since particle position and velocity can be obtained at each video frame, Eq. 2.2 contains two unknown terms, F_{xy} and F_{SB}. In order to determine these forces, we need to identify the regions where each force is acting. This identification can be carried out from the analysis of the time evolution of the particle velocity. We observed in the selected films that the dynamics of two particles moving closely suffered an abrupt change at a critical distance between particles, d_c. At this point, a change in velocity and sometimes in direction (approaching each other) was observed in both particles. We consider that this change in the dynamics is the evidence of the effects of F_{SB}.

To accurately determine in each case the time t_{cd} at which particles are at a distance d_c, the velocity of each particle was obtained for a few seconds. In most of the cases the particles were accelerating, which added some difficulty to determine the time at which d_c was reached. In order to avoid the problem we only considered the cases where one of the particles was moving at a constant velocity before aggregating. Figures 2.7a and 2.7b show the particle trajectories and velocity profiles, respectively, of one of this cases. We consider that particles are at the critical distance d_c when the particle moving at constant velocity (particle 1) undergoes a change (usually a velocity increase) that lasts until the aggregation of both particles. Dotted line in Figure 2.7b shows the time at which d_c is reached.

Just before d_c, the velocity of particle 1 is approximately constant and thus $\frac{dv}{dt} \approx 0$, and since the two particles are still far, F_{SB} is weak enough to be neglected, $F_{xy} = -F_d$. Therefore, we can calculate F_{xy} from the average velocity obtained along the period during which it is considered constant. F_{xy} is due to the propagation of the field, and since the area where this process occurs is small, F_{xy} should not change significantly just after d_c is reached. We can then obtain the averaged F_{SB} from the average velocity (between t_{cd} and t_f (when aggregation occurs)) of particle 1, assuming that $F_{SB} = -(F_{xy} + F_d)$, where F_d is now calculated using the average velocity between t_{cd} and t_f. Finally, once F_{SB} is known, we can also obtain P_a from Eq. 1.8.

2.4.2 Particle Dynamics

Among the seventeen selected cases, only in four of them a particle moving at constant speed was observed. The following subsections describe the dynamics of the pairs of particles under a given frequency of the external acoustic field in the four cases.

5 μm particles and 2.830 MHz.

Figures 2.7a and 2.7b show the particle trajectories and velocity in the plane of levitation, respectively. The closest third particle to the point of aggregation of the pair of particles was approximately at 250 μm. From Figure 2.7b we obtain $t_{dc} \approx 22$ s. During the 10 s before t_{cd} particle 1 is moving at an approximately constant velocity, while particle 2 is moving towards particle 1 in a decelerated movement. After t_{cd} both particles accelerate towards each other. The attractive secondary Bjerknes force measured in this case is 6.78×10^{-14}N.

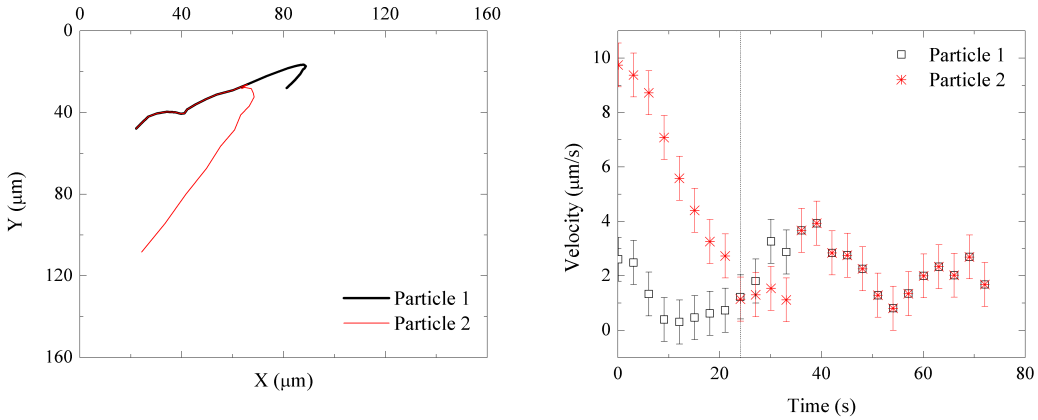

(a) (b)

Figure 2.7: (a) Trajectories, and (b) velocity profile of two 5 μm particles. Dotted line shows the time at which d_c is reached.

7.5 μm Particles and 2.830 MHz.

Figures 2.8a and 2.8b show the particle trajectories in the plane of levitation and the velocity evolution in time, respectively. In the instant just after $t_{dc} \approx 7$ s, velocity of particle 1 slightly increased while particle 2 reached a steady state. The pair of particles aggregated at $t \approx 17$ s. Right after the aggregation of the two particles, three new particles appeared in the field of view, finally forming a 5-particle aggregate. The secondary Bjerknes force obtained for the initial pair of particles is 7.02×10^{-14} N.

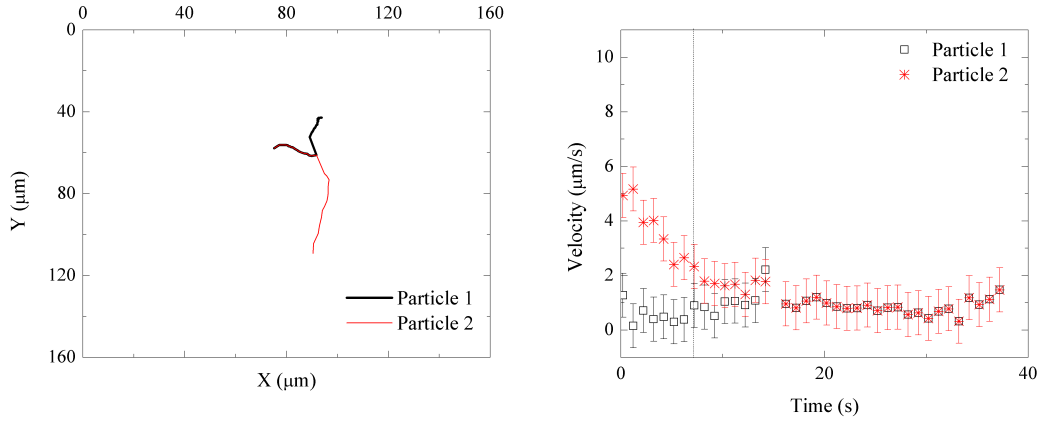

(a) (b)

Figure 2.8: (a) Trajectories, and (b) velocity profile of two 7.5 μm particles. Dotted line shows the time at which d_c is reached.

5 μm Particles and 2.866 MHz.

The aggregation of six particles was observed at the point where the pair of particles aggregated just before their aggregation took place. The larger aggregate immediately moved to another point of aggregation with higher acoustic energy. Figures 2.9a and 2.9b show the particle trajectories (the dashed trajectory corresponds to the path covered by particle 1 before particle 2 was tracked) in the plane of levitation and the velocity, respectively. Particle 1 entered the field of view at a high velocity and rapidly decelerated when it reached the region of aggregation. Particle 2 entered a few seconds later with a velocity similar to the velocity of particle 1. After $t_{dc} \approx 126$ s, particle 1 accelerated and changed its trajectory before aggregating with particle 2. Once the aggregate was formed, it accelerated towards the region with higher acoustic energy. The measured secondary Bjerknes force was 5.07×10^{-14} N.

3.5 μm and 5 μm Particles and 2.830 MHz.

Figures 2.10a and 2.10b show the particle trajectories in the plane of levitation and the velocity evolution in time, respectively. In this case, particle 1 remained approximately at the same position throughout the whole process. Other particles were observed close to the point of aggregation, and an aggregate was created 100 μm from the position where this case occurred. Particle 2 entered the field of view with a decelerating movement, while velocity of particle 1 slightly decreased and the particle remained almost quiescent from $t = 18$ s. The determination of the critical

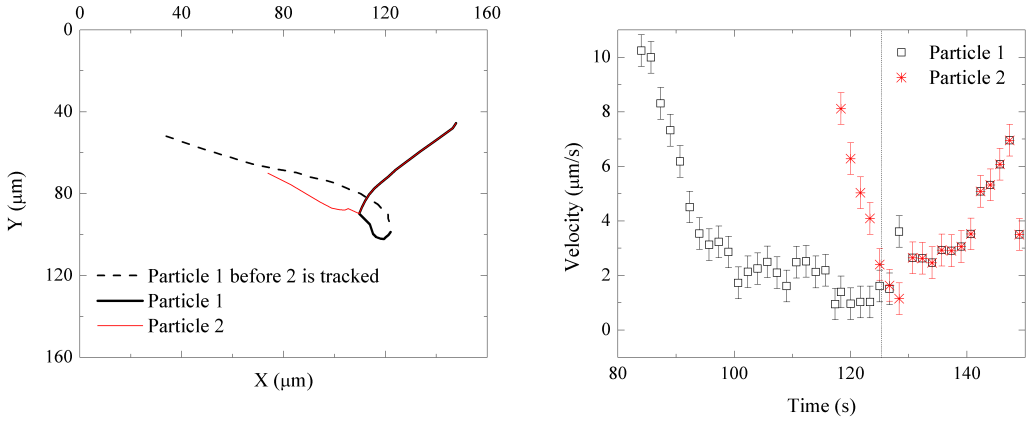

(a) (b)

Figure 2.9: (a) Trajectories, and (b) velocity profile of two 5 μm particles. Dotted line shows the time at which d_c is reached.

distance in this case is less clear than in the previous ones. Some differences can be observed in the dynamics of both particles from $t_{dc} = 26$ s since the velocity of particle 2 kept around 2 μm/s, while particle 1 slightly accelerated. The value of the secondary Bjerknes force measured in this case was 2.49×10^{-14} N.

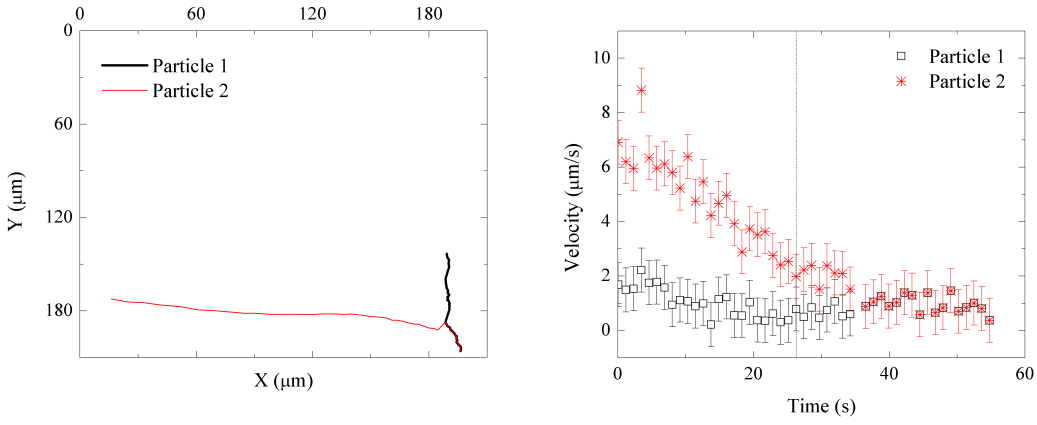

(a) (b)

Figure 2.10: (a) Trajectories, and (b) velocity profile of 3.5 μm and 5 μm particles. Dotted line shows the time at which d_c is reached.

2.4.3 Secondary Bjerknes Force

Table 2.2 shows the critical distance as well as the transverse and secondary Bjerknes forces measured in Section 2.4.1 for the four considered cases. The acoustic pressure obtained from Eq. 1.8 and the acoustic energy density calculated with Eq. 2.1 are also shown. The values of F_{xy} and F_{SB} at the critical distance obtained in each case are compatible with the expected values shown in Table 2.1. Moreover, when comparing the two cases with particles of 5 µm, F_{SB} is larger in the case of smaller d_c, in accordance with Eq. 1.8.

Particle size	d_c (µm)	F_{xy} (N)	$\lvert F_{SB}\rvert$ (N)	P_a (Pa)	E_{ac} (J/m^3)
5 µm	24.1	4.75×10^{-14}	6.78×10^{-14}	3.92×10^{5}	17.10
7.5 µm	39.2	5.75×10^{-14}	7.02×10^{-14}	1.92×10^{5}	4.09
5 µm	24.4	1.01×10^{-13}	5.07×10^{-14}	3.38×10^{5}	12.70
5 µm/3.5 µm	23.1	4.90×10^{-14}	2.49×10^{-14}	3.88×10^{5}	16.70

Table 2.2: Critical distance, forces, acoustic pressure and acoustic energy obtained in each case analysed.

The different values obtained for the acoustic pressure and energy can be explained by the fact that each case was carried out under different experimental conditions. Therefore, the particle attraction and aggregation took place in regions of the levitation plane with different values of the acoustic energy density. Nevertheless, the range of values of the acoustic energy density is very similar to the one reported by Woodside et al. (1997) (13-18 J/m^3). The order of magnitude of the values of the Secondary Bjerknes force is within the theoretically predicted range. Moreover, one can observe from Table 2.2 that the pair of largest particles (7.5 µm) generates the largest F_{SB}, while, for same size pairs of particles, the largest F_{SB} is generated at the shortest d_c, as predicted by Eq. 1.8.

Assuming that the region where particles move after reaching d_c does not contain significant variations of the acoustic pressure, Eq. 1.8 is used to predict the value of the force until the pair of particles aggregates. Figure 2.11 shows the computed secondary Bjerknes force as a function of the dimensionless distance between particles. The values of the force are within the theoretically predicted range.

Figure 2.12 shows the distance between particles normalised by the diameter as a function of the time normalised by the time between t_{cd} and the particles aggregation, t_f. The four cases analysed present a smooth evolution of the length ratio with time. The ratio turns out to be smaller in the case of larger particles, even though they start interacting at larger distances than small particles do.

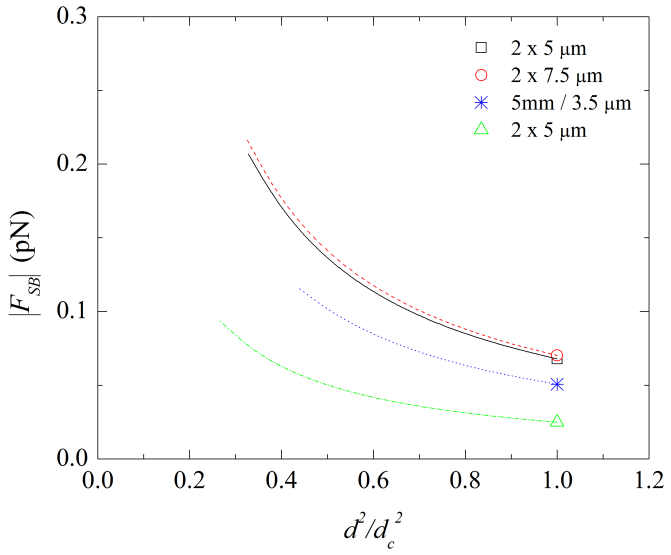

Figure 2.11: Secondary Bjerknes force as a function of the square of the dimensionless distance between particles.

2.5 Conclusions

In this chapter we have presented a series of experiments that were carried out at the PMMH, ESPCI (Paris, France). We have provided a description of the phenomena, detailing magnitudes and timeframes.

From all the videos obtained, we were able to isolate cases with only two or three particles interacting. Although each case presented slightly different characteristics, all of them clearly showed particles interacting due to inter-particle attractive forces.

We have presented a method to experimentally determine the transverse force on particles in an acoustic field as well as the secondary Bjerknes force between elastic solid particles. Moreover, this methodology provides an indirect measurement of the acoustic pressure, which qualitatively agrees with previous experiments.

We have applied the method in selected cases where particles levitated in a plane perpendicular to the direction of the acoustic field. The magnitude of the forces obtained is consistent with the theoretical predictions. The work presented here is, as far as we are aware, the first experimental determination of the secondary Bjerknes force between solid particles.

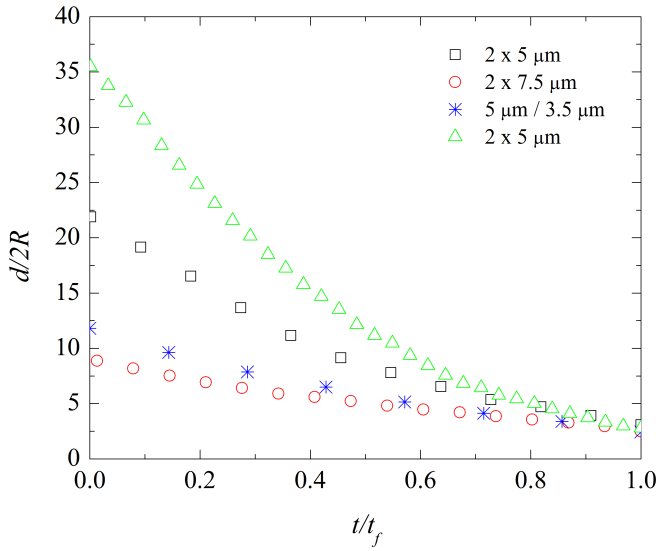

Figure 2.12: Distance between particles normalised by the particle diameter as a function of the time normalised by the time between t_{cd} and the particles aggregation.

Chapter 3

Low Frequency Vibrations on Two Phase Flows

We present an experimental setup to study the effects of low frequency vibrations on liquid-gas flows in low gravity conditions. The experiment was carried out on a sub-orbital vehicle, and the duration of microgravity was 4 minutes. The effects of high amplitude oscillations on two-phase flows with different physical properties are discussed, showing that at high viscosity the gas phase does not break-up and decays exponentially during relaxation. Moreover, shape oscillations have been observed, as well as bubble translation along the walls, due to the applied vibrations.

This experiment was carried out in the framework of a project selected by NASA: *"Application of controlled vibrations to multiphase systems for space applications"*. The aim of this project is to obtain enough information for characterising the technology in a wide range of configurations, specifically types of fluids, volume fractions, test cell geometry, bubble generation methods, frequency and amplitude. Ultimately, the phenomena studied throughout the duration of this project could be useful for the active management of multiphase flows in space.

It should be noted that the greatest challenges for developing experiments for a sounding rocket are in miniaturising and automating setups that are usually quite voluminous on ground. Moreover, since the experiment was to be launched on a rocket, live interaction and observation of the experimental phenomena was not possible. This therefore requires the automatisation of the experiment and planning the experimental protocol in a way that optimises the microgravity time. The setup also needed to meet all of the launch provider's requirements and to integrate with the other payloads without interference.

The experimental setup is described in Section 3.1. The experimental procedure and details on the flight campaign are shown in Section 3.2. Methods used to process the data are described in Section 3.3. The analysis of the obtained results is presented in Section 3.4. Finally, the main conclusions of this experiment are discussed in

Section 3.5.

3.1 Experimental Setup

The experimental setup (Figure 3.1) presented here was a continuation of earlier work done at the Microgravity Laboratory. Most of the experiment had already been constructed, but some parts had to be slightly redesigned in order to meet the launch provider's requirements.

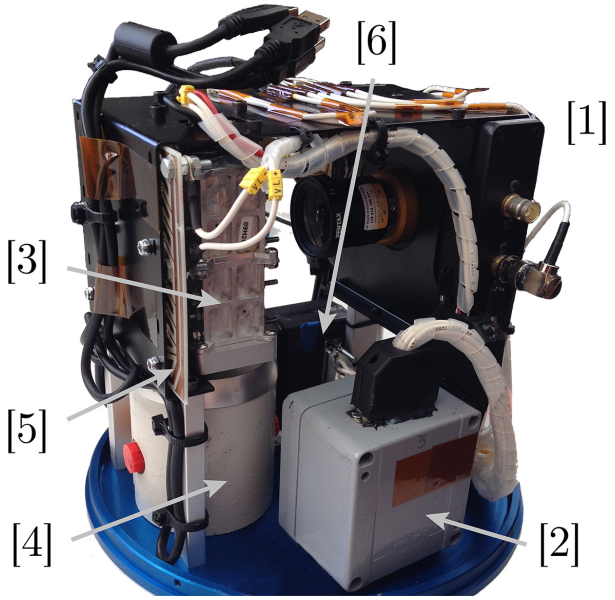

Figure 3.1: Experimental setup in flight configuration. [1] Camera, [2] amplifier, [3] test cell, [4] shaker, [5] LEDs, [6] Arduino boards. The PC was bolted down on the upper bulkhead (not in the picture).

The setup consisted of an aluminium test cell with four cylinders (25 mm diameter and 25 mm depth) and PMMA windows for illumination (through a diffusor sheet), with a 3×4 LED matrix for each cell. The process was recorded with a high-speed camera (ProcImage 240) using a Pentax C60402 TV lens with a horizontal view angle of 86.77°, meaning that post-processing of the image was required in order to remove the lens distortion from the video. The test cell was vibrated by a shaker (Brüel & Kjær LDS V201), which received a signal generated by an Arduino and amplified by a TDA2005 amplifier. A main Arduino board was used to control the function generator board, acquire data from the accelerometer, receive a discrete signal for activating the experiment and to send a payload status signal to ground control. The camera and the main Arduino board were controlled by a mini PC (Fit PC2), where all the experimental data was saved.

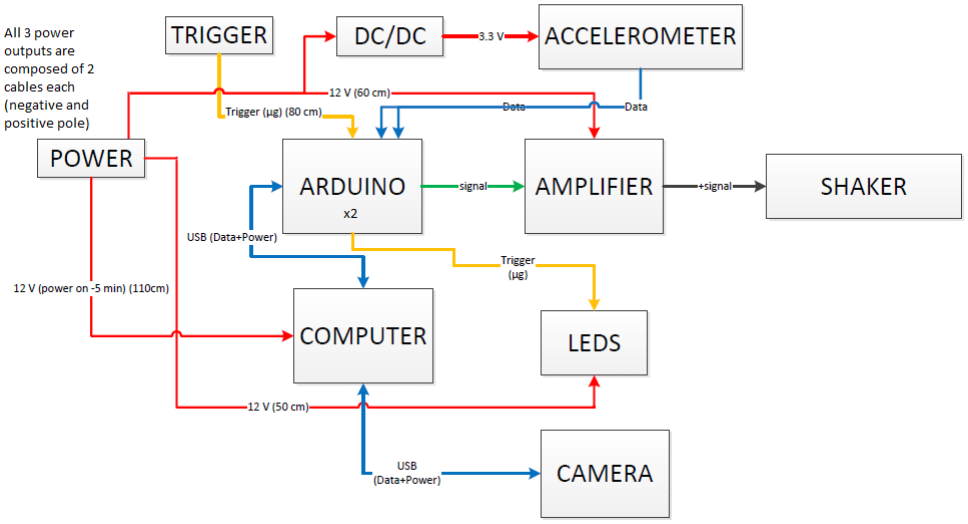

Figure 3.2: Equipment and wiring diagram.

The experiment was built inside an UP Aerospace PTS-10 canister with a 24.8 cm diameter and 23.5 cm inside height, with the total weight of the experiment being kept as low as 7.2 kg. The experiment was fed by 12 V (100 W) custom-made batteries manufactured by UP Aerospace, Inc., which powered the experiment, including the initial power peak from the mini PC switching on.

Moreover, an FTDI chip was implemented in the later phases of manufacturing, which would send a signal to the ground segment to indicate the status of the payload. A wiring diagram of the experiment can be observed in Figure 3.2, which shows all the different connections. The coding of the experimental protocol needed to be implemented in the secondary Arduino, which was a function generator, and it was controlled by the main Arduino board. Furthermore, the main Arduino board switched on most of the devices when a discrete signal (3 V or higher) from the ground segment was received.

Each cell was filled with a different liquid in order to study the effects of the low-frequency vibrations, during which the liquids have different physical properties. Table 3.1 shows the physical properties and volumes of the liquids selected for each of the cylindrical cells in Figure 3.3. We used distilled water (two different volumes), a solution of water and fluorosurfactant (0.1% of Zonyl FS-300 in distilled water) and silicon oil (FS-50). Taking water as our reference fluid, the others were selected in order to observe the effects of a larger volume of fluid, surface tension (fluorosurfactant solution) and viscosity (silicon oil). The diameters of the bubbles in each cell are slightly different: 10.9±0.3 and 9.2±0.3 mm, respectively, in cells 1 and 2, which

contained different volumes of water; and 13.7±0.3 and 13.9±0.3 mm, respectively, in cells 3 and 4, which contained a surfactant solution and silicon oil.

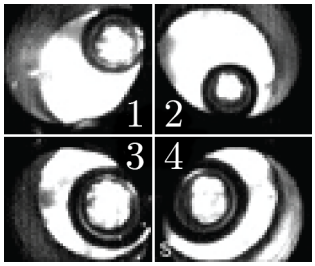

Figure 3.3: Numbered test cells, each containing a different fluid.

	Distilled water	Surfactant solution	Silicon oil
σ (dyn/cm)	72	23	20.7
ρ (kg/m^3)	997.07	997.07	960
ν (mm^2/s)	0.8928	0.8928	50
η (mPa·s)	0.8902	0.8902	48
V (ml)	7.6/8.2	7.6	7.6

Table 3.1: Physical properties (surface tension σ, density ρ, kinematic viscosity ν and dynamic viscosity η) of the liquids used in each cell. The values in the table are at 25°C. We also show the volume of each fluid.

3.2 Experimental Procedure

The experimental setup flew in UP Aerospace's SpaceLoft XL, mission SL-8. The launch took place on November 12, 2013 and reached an altitude of 117 km. The microgravity phase of the flight started at T+56 s (T being the time of launch) and a discrete signal was sent to the payload at T+60.25 s. The discrete signal activated the experiment, the camera started recording and the shaker started to apply the different vibration frequencies of 30, 40 and 50 Hz. 10 s of rest were considered between each frequency sequence in order for the bubbles to reach stable conditions. Booster separation occurred at T+240s, after which the shaker continued working, and the rocket still provided 20 s more of microgravity, as observed from our accelerometer data. Table 3.2 shows the sequence of experimental events that took place during the campaign. Information about the rocket and loads can be found in Appendix A.

Figure 3.4 shows the data obtained from our accelerometer, which was mounted on top of the test cell so that it could record the vibrations caused by the shaker as

Time	Event
T-2 days	Fluid top-off
T-5 min	Power ON
	a PC switched ON
	b Arduino resets to begin a new experiment
T	Launch
T+60.25	Discrete signal to start experiment
	a Camera automatically records
	b LEDs switched ON
	c Shaker started vibration sequence
T+6 min	Camera stopped recording

Table 3.2: Sequence of events during SL-8 launch campaign.

well as the gravity-level when the shaker was not active. The data shows a 40 Hz vibration sequence applied along the z-axis during the microgravity phase (which can be observed before and after the vibration). Low amplitude oscillations exist on the x and y axes, which are a consequence of the primary oscillations along the z-axis. However, the amplitude of these vibrations for the sequences analysed is at least one order of magnitude lower than those on the z-axis. Due to the characteristics of the accelerometer, sinusoidal waves cannot be observed in this plot.

3.3 Data Processing

Two sets of data were obtained: a high-speed video and a file with all the experimental events and accelerometer data. The video was converted into an uncompressed format in order to process it with the video analysis software. We used a plugin for Fiji that corrects the radial distortion by means of a simplified version of Brown's distortion model. In order to precisely correct the lens distortion, two images of a squared grid and a matrix of dots were taken with the camera. Two parameters controlling the distortion model were adjusted until the image in both cases showed straight lines and round circles, respectively. Figure 3.5 shows the image of a dot matrix taken with the camera, before and after correction. Moreover, the software Tracker was used to track the oscillatory movements of the test cell. An FFT analysis of the tracked paths was carried out and correlated to the accelerometer data file in order to check that the desired frequencies were applied.

The output data of our experiment was a five-minute video recorded at 180.6 fps, of which 183 seconds are under microgravity conditions. The video allowed

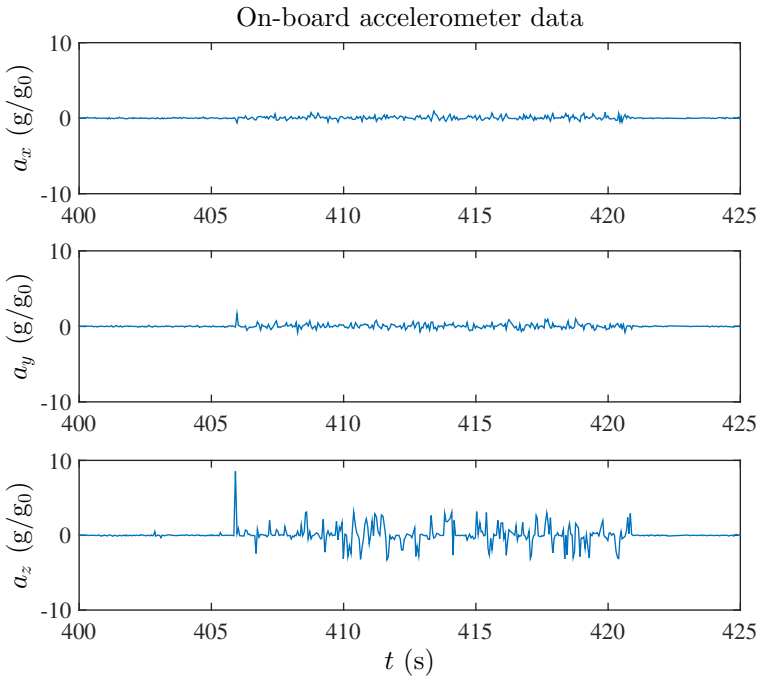

Figure 3.4: On-board accelerometer data ($g_0 = 9.81\text{m/s}^2$).

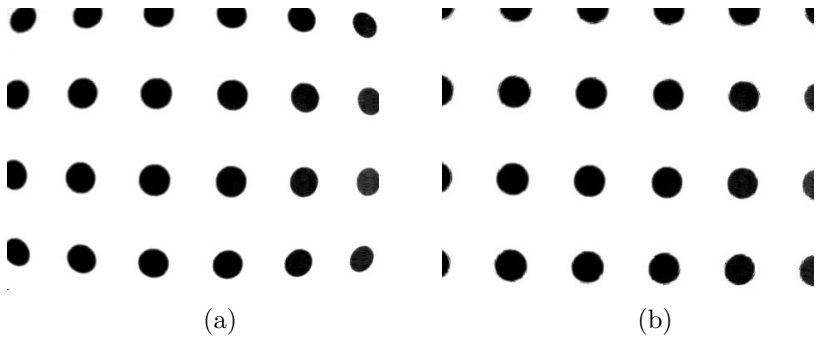

Figure 3.5: Dot matrix used for the lens distortion correction. (a) uncorrected image, (b) corrected image.

us to distinguish the behaviour of the two-phase flows depending on the motion of the shaker and the phase of the flight. We have observed that at low amplitude vibrations (A <0.4 mm), bubble dynamics are either barely altered or they undergo slight volume oscillations (i.e. expansion and compression). At higher amplitudes of oscillation, bubbles might break if a very high peak occurs (we define peak as a short vibration without a clear frequency that lasts for a short period of time); otherwise, they undergo shape oscillations and translation along the test cell wall. In

the discussion below, we will focus on the phenomena occurring at higher vibration amplitudes.

For each bubble in each cell, we have calculated the Minnaert frequency (f_M) using equation 1.5. This leads to frequencies ranging from 400 to 700 Hz, which is one order of magnitude greater than the vibration frequencies applied to the cells. This is an important consideration to take into account, since it shows that we are not driving the bubbles at (or close) to their resonance frequencies.

Effects of the rocket spin are discarded, since the bubbles remain stationary during microgravity as long as no vibration is applied. Moreover, the slower spin during the microgravity phase does not affect the bubbles either. Bubbles remain at a fixed position inside the cells, without moving towards the axis of rotation.

In order to select the frequencies to study, we carried out an analysis of the video to correlate the observations with the accelerometer data and with each event during flight. A fixed spot of the test cell has been tracked in order to obtain the amplitude of the movement. The exact frequency of the sequence was obtained by means of an FFT analysis of the signal that was obtained from this analysis. We have identified the time during which each frequency was applied. We have measured the amplitude of the movement of the test cell at each selected sequence. Table 3.3 shows the parameters corresponding to each sequence.

	Sequence 1	Sequence 2	Sequence 3	Sequence 4
f (Hz)	30	40	40	50
A (mm)	$0.125 < A_1 < 0.25$	$0.15 < A_2 < 0.235$	$0.48 < A_3 < 1.2$	$0.15 < A_4 < 0.6$
Δt (s)	11.94	4.83	14.93	16.46

Table 3.3: Frequency (f), range of amplitude (peak to peak) (A) and duration of each of the selected sequences from the video.

Figure 3.6 shows the tracked cell movement obtained from each of the analysed video sequences presented in Table 3.3. An FFT analysis of each of these signals gives the frequencies shown in Table 3.3, which corresponds to the frequencies planned in the experimental protocol.

3.4 Results

3.4.1 Overview

We have observed different phenomena during each of the selected sequences, which seem influenced by the amplitude of the applied vibrations. During sequence 1, the bubbles undergo shape oscillations while the vibration is applied. This is observed specially in cell 3, which contains a solution of water and a surfactant. Cell 1 seems to

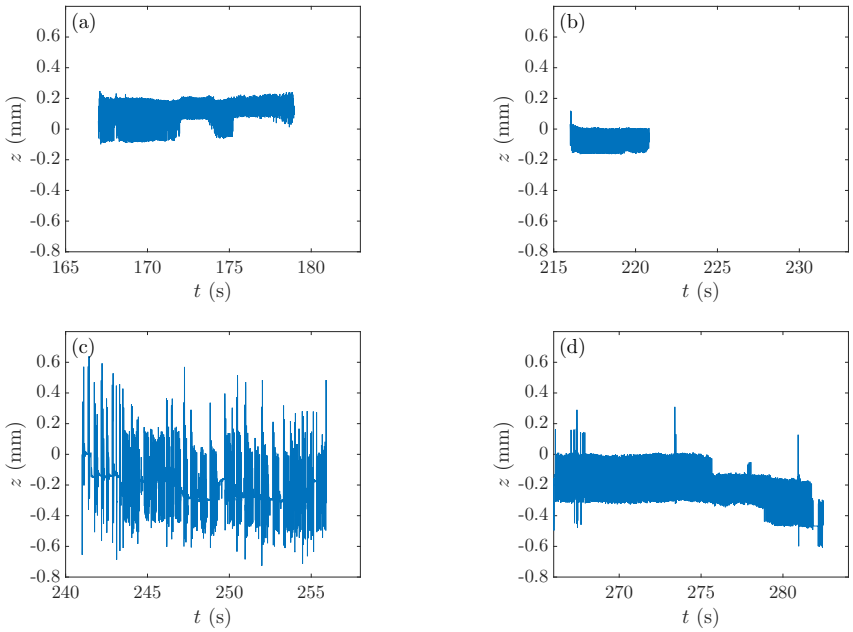

Figure 3.6: Tracked motion of the test cell during the different video parts selected. (a) to (d) correspond to sequences 1 to 4, respectively. For reference, $t = 0$ corresponds to the rocket lift-off.

contain more visible effects towards the end of the video. No translation or break-up of the bubbles is observed. The bubbles remain at their initial position throughout the sequence.

In sequence 2 we can also observe shape oscillations in all the bubbles. The bubble in cell 1 oscillates between a horizontal stretching and a vertical stretching.

Sequence 3 corresponds to the time during and right after the booster separation, which generates a peak of amplitude, and is followed by oscillations generated by the shaker. Bubble behaviour depends on whether they are affected by a short shock or a long shock of a few seconds at constant amplitude. The observed phenomena include bubble break-up, shape oscillations and translation.

In sequence 4, some effects of the rocket descent can be observed. In addition, the 50 Hz vibrations still have a strong effect on the bubbles, especially in the cell with lower surface tension liquid, where various bubble shapes can be distinguished.

All the phenomena described below were observed in sequence 3.

3.4.2 Vibrations at Constant Frequency: Bubble Shape Oscillations

We analysed 9 periods of $\Delta t \simeq 0.4$ s each, where vibrations are applied along the axis of the shaker (z-axis) at $f = 40$ Hz and nearly constant amplitude.

We obtained the average amplitude (peak to peak) of displacement for each period and from the standard deviation of the tracked video data $\bar{A}_{pp} = 2\sigma$. This value gives a good approximation of the average motion of the shaker during the time considered.

When comparing the average vibration amplitude to the bubble behaviour shown in the videos (e.g. cell 1 in Figure 3.8), we observe bubble shape oscillations with sharper edges within a sufficiently large amplitude of vibrations. The threshold value was determined to be approximately 0.37 mm.

In the selected periods of time, we observed different behaviours in each cell. It should be noted that right before the start of each time period, the bubbles were stationary and showing a nearly spherical shape. In cell 1 we observed that bubbles deformed and adopted shapes similar to previous observations which consisted of triangular or quadrilateral shapes. They were also separated from the walls. Leighton (1994), Trinh et al. (1998), Versluis et al. (2010) and Sommers & Foster (2012) reported surface modes when applying high frequency oscillations (ultrasound), and Risso & Fabre (1998) reported shape oscillations due to turbulent flows. In Figure 3.8.1, mode $n = 4$ can be clearly distinguished. The bubble in cell 2 seems to be affected by the vibrations, but it is unclear whether it undergoes any surface mode oscillations, since its location in the cell does not allow full observation of the bubble. However, the visible side of the bubble shows a slight deformation, depending on the amplitude of the applied vibration. The bubble in cell 3, shows a rather unpredictable behaviour by adopting shapes like one with high peaks on the upper side, which do not correspond to any surface mode oscillation. The bubble in cell 4 adopts an elongated shape on the axis that is perpendicular to the axis of vibration (Figure 3.7). For each vibration amplitude, there is a maximum bubble deformation and, once it is reached, it is maintained even if the shaker keeps vibrating. A similar behaviour is observed when amplitude peaks are applied, which is explained in Section 3.4.3. In general, the shape adopted by the bubble is generally affected by the cylindrical geometry of the cell.

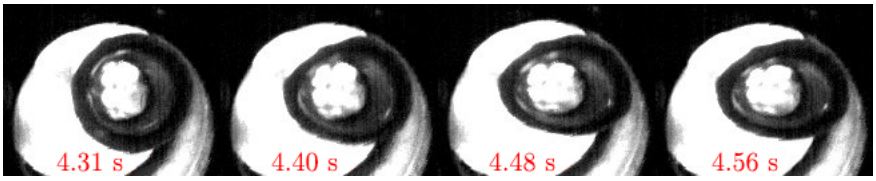

Figure 3.7: Sequence of the deformation observed in the case of silicon oil.

We will now focus on cell 1, since it is the only cell where surface oscillation modes can be distinguished. Figure 3.8 shows five of the nine time periods analysed. During period 1, the bubble undergoes the highest peak-to-peak vibration amplitude, $\bar{A}_{pp1} = 0.42$ mm, showing sharper shape deformations of mode $n = 4$. When a longer time period than the one shown in Figure 3.8.1 is considered, the shape is observed

to oscillate at 25 Hz while the shaker frequency is 40 Hz. Periods 2 and 3 correspond to $\bar{A}_{pp2} = 0.37$ mm and $\bar{A}_{pp3} = 0.39$ mm, respectively. Shape oscillations of either mode $n = 3$ or $n = 4$ are observed in these periods. In all of the time periods, the observed shapes seem to repeat periodically and are less apparent towards the end of the period. Bubbles in periods 4 and 5 show little shape deformation compared to the previous cases. In period 4, the bubble vibrates at mode $n = 4$, but the edges are quite smooth. Sequence 4 is right above the 0.37 mm threshold that we have identified ($\bar{A}_{pp4} = 0.37$ mm), which explains why the shapes are not as sharp. In period 5 ($\bar{A}_{pp5} = 0.36$ mm), no surface mode oscillation can be distinguished.

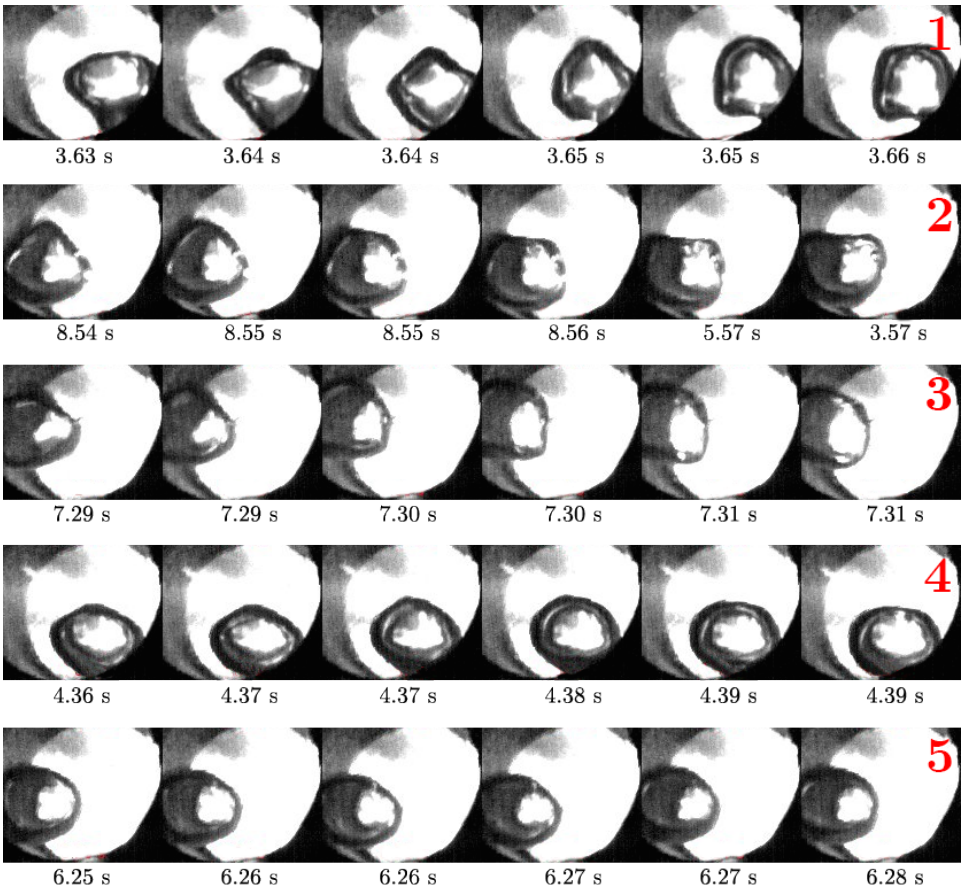

Figure 3.8: Shape oscillation in cell 1.

3.4.3 Decaying Vibrations: Shape Oscillation Relaxation

We have selected seven periods of irregular oscillations (different amplitudes and no fixed frequency) from sequence 3 of the video (Figure 3.9) in order to analyse the

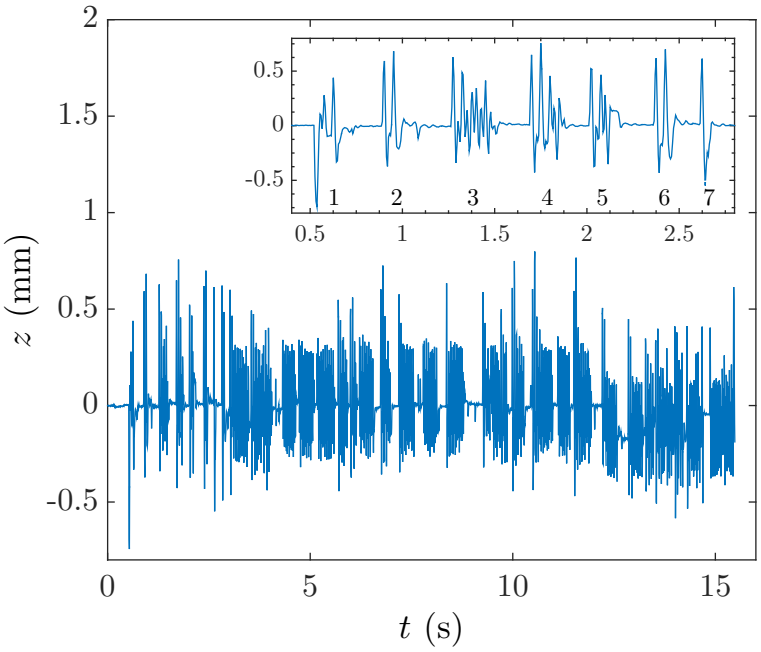

Figure 3.9: Tracked path of Part 3. Zoom on the seven peaks studied in this section.

dynamics of the bubbles when the test cell stops moving after a peak. In the case of cells 1 and 2, the bubble oscillates smoothly, expanding and compressing until it reaches a spherical shape (Figure 3.10). The observed expansion and compression are a visual effect due to the lighting and the position of the bubble. The eccentricity ($\varepsilon = \sqrt{1 - d_M^2/d_m^2}$) oscillates (although not always in the same manner, and thus it is not reproducible) while decaying (to 0) and it goes back up to deform again. The bubble in cell 3 generally shows an irregular shape very far from an ellipse after the vibrations stop. At later times, the bubble shape is close to an ellipse oscillating from highly eccentric to less eccentric.

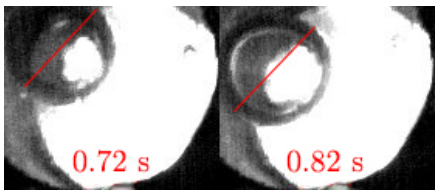

Figure 3.10: Bubble expanding after a vibration peak.

The bubble in cell 4 (silicon oil) responds to peaks by adopting a very eccentric shape, stretching its shape along the plane perpendicular to the axis of vibration.

Afterwards, the bubble slowly recovers its spherical shape. Since the aspect ratio ($\epsilon = d_M/d_m$) is a parameter commonly used in the study of bubble shape, it will be used to quantitatively study the silicon oil bubble. The aspect ratio decays similarly in all of the studied periods. Figure 3.11 shows the aspect ratio at each period. Even though the initial value of ϵ varies between them, they all tend toward sphericity ($\epsilon = 1$) in a similar way. The difference between curves is possibly related to the amplitude of the vibration experienced by the bubbles, which generates a different ϵ when the vibration stops. Vibrations are not uniform (frequency not constant), and the time between each peak varies slightly from one to another, as can be seen in Figure 3.9. This means that, in some cases, the time between peaks is too short for the bubbles to become spherical, although they are always close to it. Although all the cases show similar behaviour, in Figure 3.11 we only present those that reach $\epsilon = 1$.

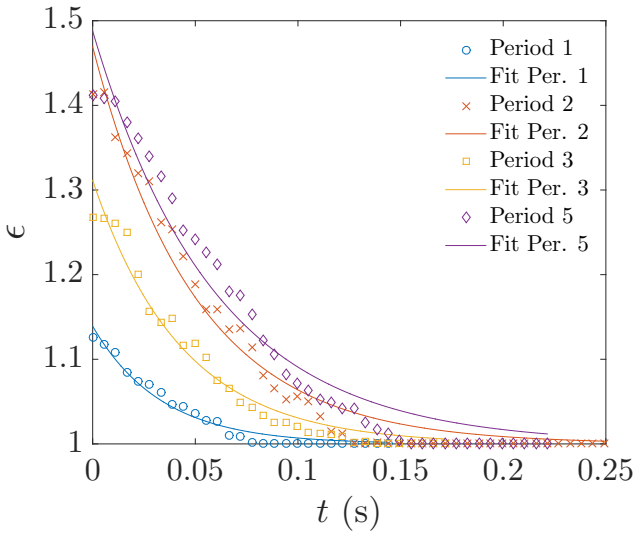

Figure 3.11: Aspect ratio (ϵ) *vs.* time for the after-peak periods studied. Lines correspond to data fitting to Equation 3.1.

Figure 3.11 shows that the behaviour of ϵ exponentially decays:

$$\epsilon = ce^{rt} + 1, \tag{3.1}$$

where c and r are constants.

Figure 3.11 shows the fitting of the experimental data to Equation 3.1. It can be observed that, depending on the initial conditions of the bubble (i.e. ϵ at $t = 0$), the relaxation time lies between 80 and 150 ms. The fitting coefficients for each period can be found in Table 3.4.

	c	r
Period 1	0.139	29.92
Period 2	0.4692	19.95
Period 3	0.3115	23.18
Period 5	0.4877	16.81

Table 3.4: Fit coefficients for the curves in Figure 3.11.

3.4.4 Short Vibration Peaks: Bubble Break-Up

The dynamics of a bubble after a peak (see Figure 3.12 right) are significantly different from the dynamics when a vibration of constant amplitude and frequency is applied. Bubbles react to the first (see 1 in Figure 3.12) observed peak (1.2 mm peak to peak) differently, depending on the fluid (Figure 3.12 left). Boundary (cell geometry) effects can affect the bubble behaviour. In Figure 3.12 at the left, for instance, the shape of the bubbles is conditioned by the cylindrical shape of the cell. Depending on the initial position of the bubble before breaking up, it adopts a certain shape. Bubbles in cells 2 and 3 were initially in the center of the cell, and they adopt a cashew nut shape. If a larger amplitude was applied, the bubble would break-up in two parts with approximately the same volume. Bubbles in cells 1 and 4 are slightly shifted to the right and left of the cell, respectively. These bubbles do not deform from the centre, unlike the other two; but they are more deformed on the side, which could lead to the bubble breaking up into two parts with different volumes. A qualitative description of the break-up process, depending on the fluid, can be found below.

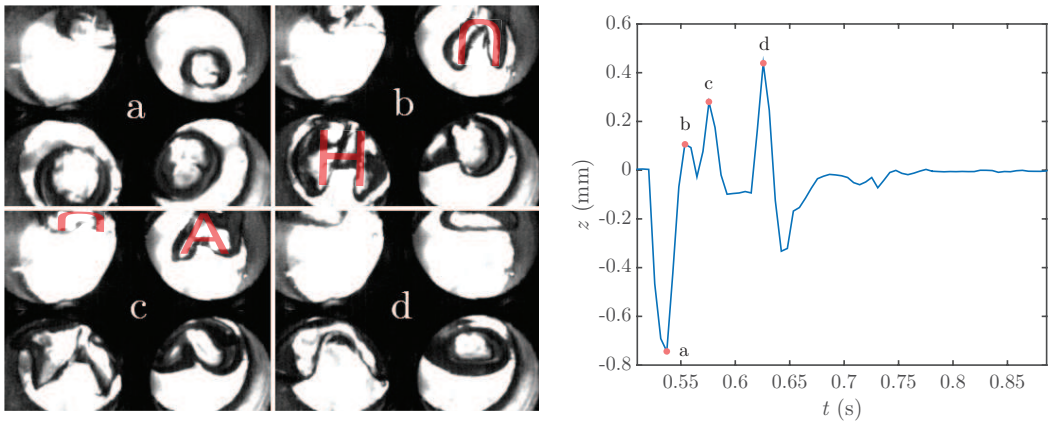

Figure 3.12: Bubbles in the cell at the time of booster separation. Bubble shape depends on the fluid.

The bubble in cell 1 is initially on the right side of the cell, forming an inverted "U" with one side larger than the other. The bubble does not seem to fully split. However, it can be seen that a small quantity of air breaks off from the main bubble.

Before breaking up, the bubble in cell 2 adopts an inverted "U" or cashew nut shape similar to that reported by Yoshikawa et al. (2010). The two sides do not separate completely but instead start to coalescence at the bottom, forming an "A" shape. After coalescence, the bubble undergoes shape oscillations, reaching an almost rectangular shape with rounded corners at times.

The bubble in cell 3 consists of two vertically stretched bubbles joined at the centre, like an "H" shape. The bubble finally breaks up. This case is the one that is most sensitive to the shaker vibrations, as was expected due to the lower surface tension of the fluid.

The bubble in cell 4 behaves similarly to the one in cell 1. This bubble, which is of high viscosity, has a cashew nut shape at the left of the cell. The bubble is slightly pinched inwards, which deforms it into the inverted "U" or cashew nut shape, with the right side of the bubble slightly larger than the left side. The bubble quickly recovers its spherical shape after the peak.

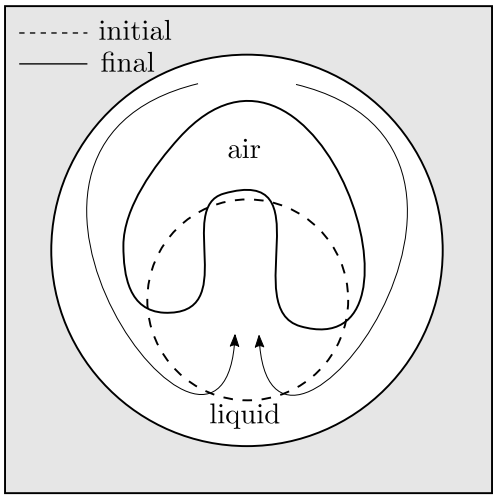

Figure 3.13: Conceptual sketch of the break-up process of the bubble.

The cashew nut shape observed in some of the cells can be explained as follows (see sketch in Figure 3.13). The bubble is initially at the bottom, due to the downward movement of the cell. Right afterwards, the air is pushed up and the liquid down as the test cell moves upwards. Due to the cylindrical geometry of the cell, the liquid flows back up through the centre of the bubble, forcing it to adopt the cashew nut shape.

3.4.5 Long-Period Vibrations: Bubble Translation

When studying a time scale that is longer (e.g. the one shown in Figure 3.9) than the ones considered in the previous subsections, we can observe that bubbles move from one side of the test cell to the other. This translation of the bubble typically occurs when the cell is vibrated and the bubble always stays close to the cell walls. The bubble crawls along the wall back and forth, without doing a complete revolution in the cell.

Due to the shape oscillations of the bubble, we can distinguish two phenomena, i.e. translation and separation from the wall, which are similar to the observations reported by Beysens (2004). When the test cell is vibrated, the bubble undergoes shape oscillations, as seen in Section 3.4.2, which highly deform it from its spherical shape.

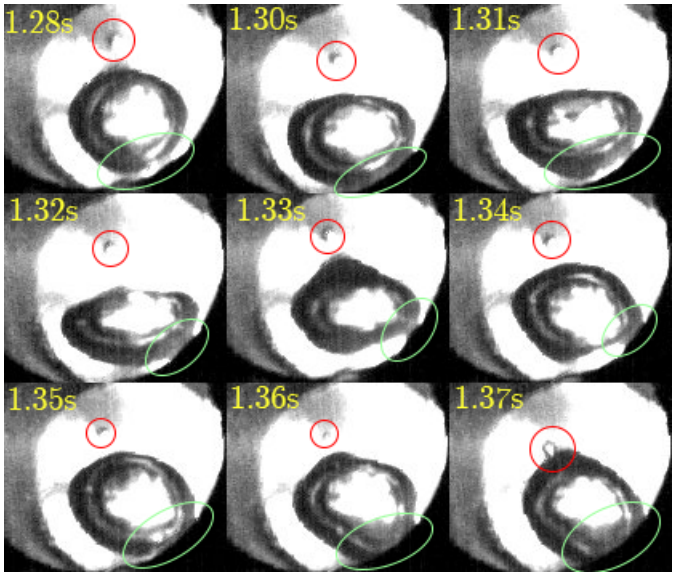

Figure 3.14: A sequence showing the bubble deforms and separates from the wall in cell 1. Red circles show a small bubble interacting with the larger one. Green circles show the contact point of the bubble with the wall.

At the start of a typical sequence, the bubble of spherical shape is very close to the wall on one side of the cell. As the bubble shape deforms due to vibrations, it moves slightly away from the wall, bouncing with the wall, and returns at a slightly different position than it was initially. Figure 3.14 shows this phenomenon for the case of water. We have observed a similar behaviour in the other cells but at different displacement velocities. The larger the deformations, the greater the distance the bubble displaces along the wall of the cell. In the case of cell 3, the motion is slower compared to water, which can be understood as an effect caused by

the lower surface tension. The bubble deformation in cell 3 is more unpredictable, and does not present sharp and long edges (as in the case of water) but instead smaller deformations. Thus, the displacement of the bubble along the wall is slightly slower than in the case of water. A conceptual sketch of this process can be observed in Figure 3.15, showing the difference in the displacement between lower (a) and higher surface tension (b). Although the direction of the movement in the sketch is towards the bottom of the cell, bubbles can move in the opposite direction too, depending on the deformation presented.

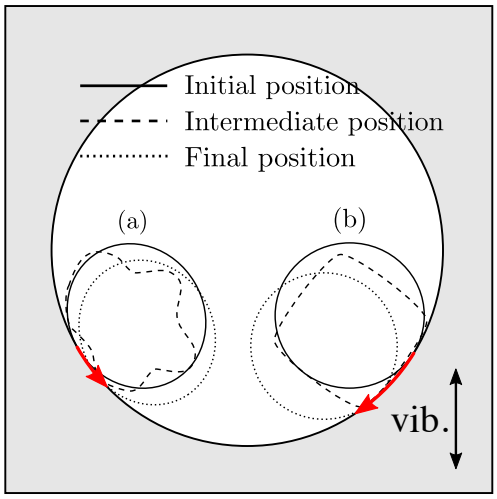

Figure 3.15: Conceptual sketch for the translation process of the bubble where (a) corresponds to the behaviour of the bubble in cell 3 and (b) corresponds to cell 1.

No movement of the bubble towards the upper half of the cell was observed. This can be due to the direction of the cell vibration itself, its amplitude, or to residual vibrations in the perpendicular plane.

One case of a bubble moving while the test cell is not vibrating was observed (cell 1, water) when the shaker paused for about 500 ms. Figure 3.16 shows the x and z components and $r = \sqrt{x^2 + y^2}$ of the bubble movement throughout sequence 3 of the video. The time when the bubble moves without the cell vibrating can easily be identified between t = 8 s and t = 10 s, where a steep slope without vibration is observed in Figure 3.16. The bubble is initially located on the left side of the cell, where it vibrates and moves until it almost reaches the bottom part. At this time the shaker stops vibrating, and the bubble moves towards the right side of the cell while in contact with the wall at all times (Figure 3.17). The approximate mean velocity of the bubble displacement at this point is 13.3 mm/s, which is about four times faster than the mean velocity measured in the other translations observed in the sequence. It is, however, difficult to observe whether the bubble is rotating along the wall or is translating. Effects of gravity causing the movement along the other

axis can be ruled out, since the acceleration along the other axis does not present any disturbance that is different from the previous cases. Moreover, none of the other three bubbles show this behaviour during this pause.

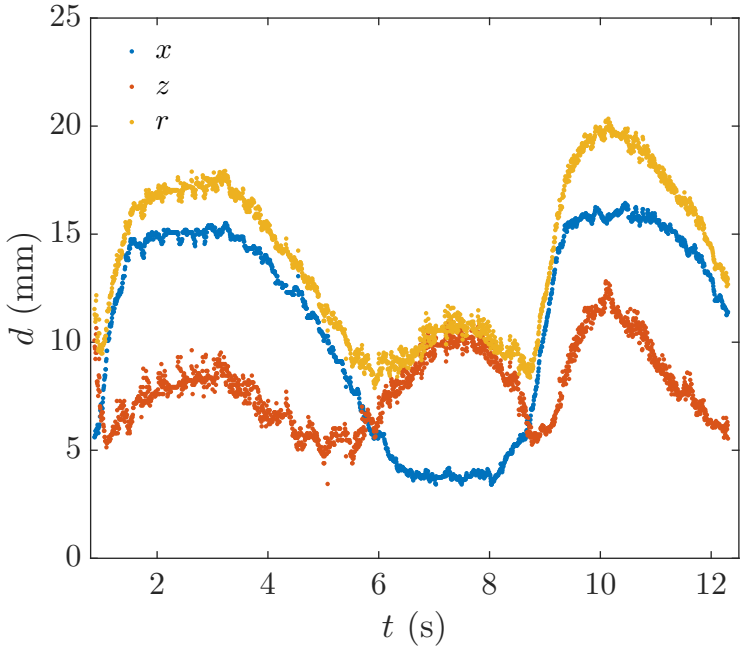

Figure 3.16: Manual track of the bubble geometrical center (visually obtained) throughout sequence 3 of the video, showing the motion along the x-axis, z-axis, and r.

3.5 Conclusions

We designed and built an experimental setup to generate low amplitude, low frequency vibrations on four cells containing different liquids in microgravity conditions. We then carried out a study of the generated phenomena by means of image analysis.

While considering a small time scale ($\sim$ 100 ms), we observed bubble break-up and provide a qualitative explanation of the flow behaviour that ultimately caused the bubble to split up if the vibration amplitude was sufficiently large. Silicon oil (higher viscosity) is the less susceptible to break-up. It should also be noted that wall effects are significant in this experimental setup.

The shape oscillations observed are similar to those previously reported (Leighton (1994), Trinh et al. (1998), Risso & Fabre (1998), Versluis et al. (2010) and Sommers & Foster (2012)), and they cause the bubble to separate from the wall and translate.

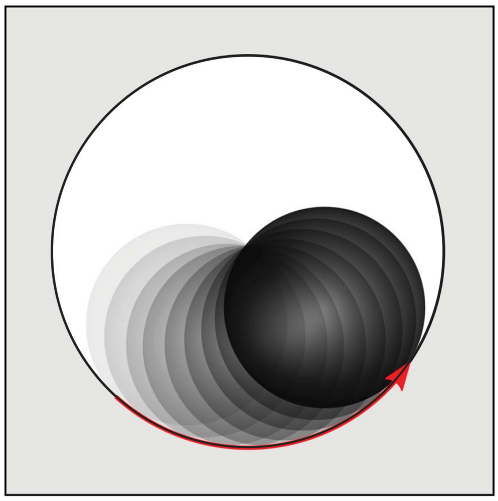

Figure 3.17: Conceptual sketch of the translation process of the bubble in cell 1 when no vibrations are applied.

Nevertheless, most of the works reporting shape oscillations (¡ 1 mm) focus on smaller bubbles under acoustic fields (¿ 10 kHz). Thus, our observations prove that shape oscillations can also take place in large bubbles and with lower vibration frequencies. Depending on the abruptness of the shape oscillations, the bubble will move longer or shorter distances.

Finally, once the vibration stops, each bubble shape relaxes differently, depending on the fluid. In the case of silicon oil, the bubble diameter exponentially decays until it recovers its spherical shape. Shape oscillations are observed in water, while the low surface tension case is more unpredictable. Further experimentation should be carried out to study each effect individually.

Chapter 4

Effects of Spin on Two-Phase Flows

This chapter focuses on how high and low rotation velocities affect a low surface tension fluid in microgravity conditions. The behaviour of injected bubbles moving towards the centre of rotation and the shape of a large bubble in a rotating fluid were studied. Moreover, we observed other effects (gas injection, rise, rotation and displacement) during the microgravity phase, as well as when a high amplitude peak is applied in order to break up the air bubble.

The goal of this experiment is to study the dynamics of a rotating fluid. A detailed description of the experimental setup is provided in Section 4.1. The preliminary study conducted on the ground for determining the experimental protocol is presented in Section 4.2, as well as the details on the launch campaign and the final experimental protocol. An overview of the phenomena observed and a detailed analysis of the results is presented in Section 4.3. Finally, the conclusions of this experiment are discussed in Section 4.4.

This experiment was carried out in the framework of a project selected by NASA: *"Application of controlled vibrations to multiphase systems for space applications"*, which is explained in Chapter 3.

4.1 Experimental Setup

We present an experimental setup (Figure 4.1) that was built and designed for studying the effects of high frequency vibrations on air bubbles in a low surface tension fluid after injecting them through different orifices. The setup was designed to meet the launch provider's requirements by fitting it into two cylinders of 24.8 cm diameter and 23.5 cm height.

This experiment comprised a test cell, where the studied phenomena took place, and three additional subsystems: bubble injection, acoustic wave generation and

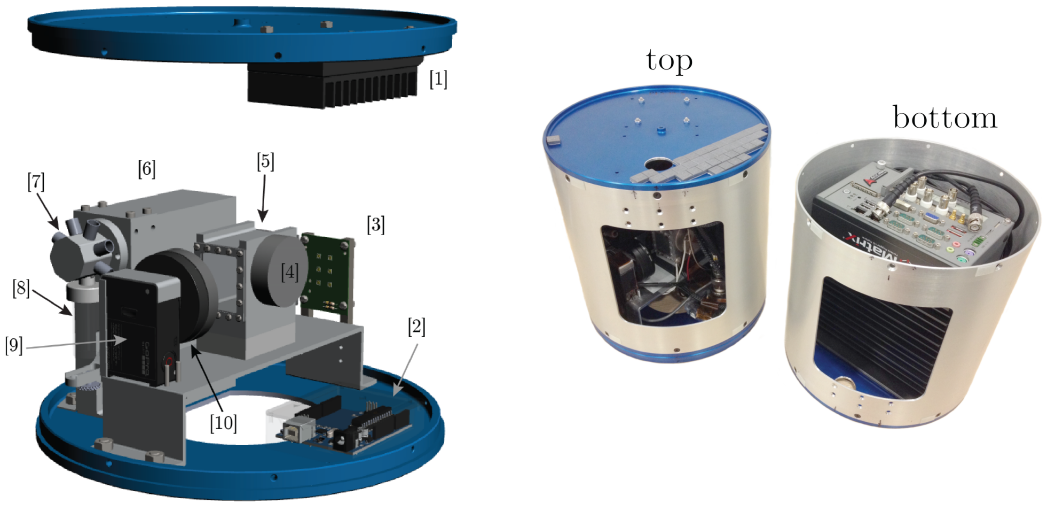

Figure 4.1: CAD and picture of the experimental setup. The CAD shows: [1] DC-DC converter, [2] Arduino UNO, [3] LEDs, [4] PZT, [5] test cell, [6] syringe pump, [7] rotary valve, [8] syringe, [9] GoPro camera and [10] BlurFix and macro lenses. The PC is bolted down on the bottom canister and the waste tank is mounted next to the LEDs (not in the picture). The picture shows the experimental setup in flight configuration. Bottom canister: PC with integrated function generator and amplifier. Top canister: The rest of the experimental equipment.

data acquisition. The injection subsystem generated bubbles inside the test cell at the required flow rate. Once inside the test cell, the acoustic waves were generated while the whole process was recorded. Throughout the flight, data was acquired from the accelerometer.

Two UP Aerospace PTS-10 canisters were used for this experiment (Figure 4.1). The lower canister contained the PC. The upper canister contained the camera, the test cell, the accelerometer, the Arduino board, the DC-DC converter, the LEDs and the waste tank.

A wiring diagram of the experiment is shown in Figure 4.2, which illustrates the different power connections (red and black), data signal connections (yellow and green) and air tubing (blue). Both the PC and syringe pump were powered at 24 V, while the rest of the equipment was powered at 12 V from the DC-DC converter. The power source for the experiment was custom-made by UP Aerospace Inc. to provide 150 W at 24 V. The PCM (Payload Command Module) served as an interface between the experiment and the rocket, which sent a payload status signal to the ground station, which in turn responded with a discrete signal to activate the experiment. A more detailed description of the components and subsystems that compose the experimental setup can be found in the following paragraphs.

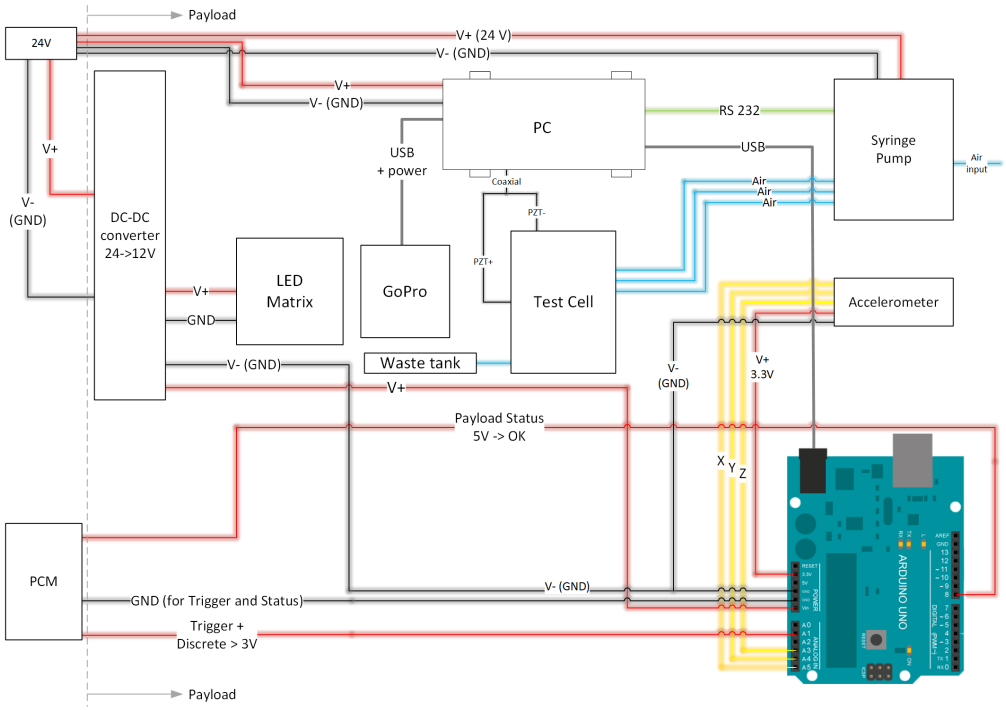

Figure 4.2: Equipment and wiring diagram.

4.1.1 Test Cell

The test cell was designed with Solid Works. The external dimensions of the test cell were 60 mm × 37.25 mm × 53 mm (H×W×L), and the inner dimensions were 50 mm × 27.15 mm × 53 mm (H×W×L), built in aluminium. It has two windows through which the cavity is illuminated, and the process is recorded. The windows of the test cell were made of transparent PMMA. Sixteen M2 screws were used on each side to fix the windows, frames and diffuser to the test cell. There were four threaded M6 orifices at the bottom to mount the test cell on the bulkhead. Moreover, it has three orifices for injection (one at the side and two at the top) and a fourth orifice used as a pressure control and to take the excess fluid to the waste tank. The internal diameters of the injection orifices were 100 µm and 25 µm. Each orifice has an anti-return valve to avoid the fluid from flowing in the opposite direction. A 3D image of the test cell (together with the cylindrical PZT) is presented in Figure 4.3.

The cell was filled with low surface tension liquid in order to study the effects of the acoustic field on bubble detachment and dynamics after detachment. Table 4.1 shows the physical properties of the chosen liquid, a solution of water and fluorosurfactant (0.1% of Zonyl FS-300 in distilled water).

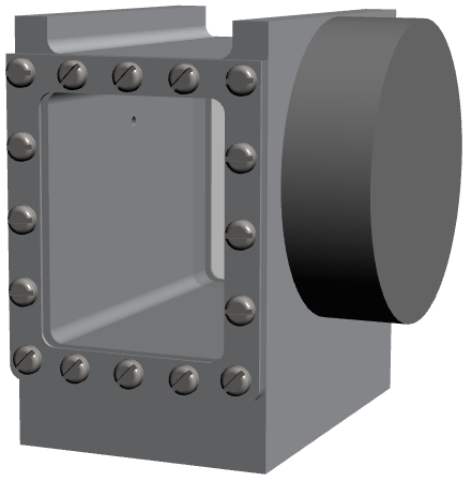

Figure 4.3: 3D image of the test cell and the cylindrical PZT attached to one wall of the cell.

	Surfactant solution
σ (dyn/cm)	23
ρ (kg/m^3)	997.07
ν (mm^2/s)	0.8928
η (mPa·s)	0.8902

Table 4.1: Physical properties (surface tension σ, density ρ, kinematic viscosity ν and dynamic viscosity η) of the liquid used in the test cell. The values in the table are at 25°C.

4.1.2 Bubble Injection

We used the bubble injection system to generate bubbles inside the test cell. This system was composed of:

- *Syringe Pump.* This device, PSD/4 (Hamilton) allowed control of the gas flow rate. It was not originally intended for this use as it was part of a larger medical device; thus, there was neither software nor drivers for controlling it. Drivers were programmed in LabView, and with this software we were able to use the mini-PC to control the different functions of the syringe pump.

- *Syringe.* A syringe was attached to the syringe pump, which contained the desired amount of gas. We chose a commercially available 5 mL glass syringe from Hamilton, which was used during the ground tests. However, we had a PMMA replica custom made for the flight configuration, since glass is not suitable for a sounding rocket flight.

- *Rotary Valve.* This valve allowed air to be injected into the different orifices of the test cell, one at a time. Thus, we were not able to simultaneously inject through different orifices.
- *Tubes.* We used UpChurch PEEK tubing of different diameters to guide the injected air into and out of the test cell.
- *One Way Pressure Valve.* Pressure valves were used on each orifice to ensure that air flowed in the proper direction when a certain critical pressure was reached.
- *Gas Outlet.* The test cell included an escape valve to avoid any overpressure in the system.
- *Waste Tank.* The outlet tube was fed lead to a waste tank to store the fluid coming out of the test cell, if any.

4.1.3 Acoustic Wave Generation

By applying an electrical signal, we were able to generate a standing wave inside the test cell. The following devices constituted this system:

- *Function Generator.* A PCI bus single-channel arbitrary waveform generator (Tabor Electronics 5325) allowed the frequency and voltage amplitude of the sine wave to be generated and controlled. This device was controlled by means of LabView.
- *Amplifier.* The function generator produced a very low output voltage amplitude, which led to very low acoustic pressures inside the test cell. In order to obtain higher amplitudes, a 10× voltage amplifier (Tabor Electronics 3322) was used, which also served as a PCI card. The amplifier could provide up to 20 or 40 V_{p-p}, depending on the manufacturing configuration.
- *Piezoelectric Transducers (PZTs).* The output from the amplifier was directly connected to a piezoelectric transducer, which was attached to a wall of the test cell with a nominal frequency of 160 kHz. It transformed the electrical signal into mechanical vibrations. It was connected by means of coaxial cables that were attached to the transducer using conductive epoxy. The PZT was a cylinder with a diameter of 43 mm and thickness of 12.5 mm (material Pz26, Meggitt (Ferroperm)).
- *PC.* The function generator and the amplifier were PCI cards mounted inside a mini computer (MXC - 4000/2G, AdLink Technology Inc.), which had no moving parts. The PC powered the function generator and the amplifier while also controlling them.

- *DC-DC Converter.* To regulate the voltage from the batteries and to convert it to the required voltage for the equipment, a DC-DC converter was used.

4.1.4 Data Acquisition

Videos were recorded in order to obtain data from the phenomena taking place inside the test cell. To this end, the following devices were required:

- *Camera.* A GoPro Hero 3+ Black Edition camera was placed facing one of the windows and recorded 720p (1280×720 pixels) at 120 fps. A solid state relay was used to turn the camera ON and OFF. Macro lenses (+4 and +10) were mounted on the camera by means of the BlurFix attachment. The obtained videos were saved in a micro SD card inside the GoPro camera, making it independent from the PC.
- *LED Matrix.* A 2 × 3 matrix of LEDs illuminated the test cell from the opposite side of the camera. A diffuser sheet provided homogeneous background illumination. The PCB was designed and built in our laboratory.
- *Accelerometer.* A three-axis accelerometer from Freescale Semiconductor was used to obtain the acceleration data during all the flight phases. The accelerometer was previously calibrated in the lab.
- *Arduino UNO.* This was used as an interface to send and receive signals to and from the ground segment, and also as a data acquisition device for the accelerometer.

4.2 Experimental Procedure

In order to determine the experimental protocol, we carried out preliminary tests on ground to determine the orifice positions, the final design of the test cell, the gas flow rate and the frequencies to be used. Tests were carried out on a preliminary test cell designed for ground tests and also on the final flight test cell.

4.2.1 Preliminary Study

We used a hydrophone (HCT-0300, Onda Corporation) together with an acoustic meter (MCT-1010, Onda Corporation) to measure the acoustic pressure inside the preliminary test cell (Figure 4.4). The preliminary test cell, was designed with an open wall (at the top) to carry out pressure measurements, and it had several injection orifices to determine the best ones for the final test cell. We took 21 series of measurements, each series consisting of measurements from points a to b (as shown in Figure 4.4) in steps of 0.1 or 0.2 mm, which were controlled with a syringe pump

(KDS Legato 180) that was adapted for this application. On the y-axis, we took the positions of the pre-drilled injection points as a reference and took measurements at -1 cm, 0 and 1 cm. Finally, we marked 7 positions on the z-axis, from the bottom of the test cell, to the free surface in steps of 0.5 cm.

The tests were carried out by applying a frequency of 167 kHz in distilled water at a voltage of 1 V, which was amplified to 19.7 V. The frequency was chosen by measuring the maximum acoustic pressure (p_{ac}) inside the test cell. According to the hydrophone calibration chart, the sensitivity at that frequency is 0.34202 V/MPa.

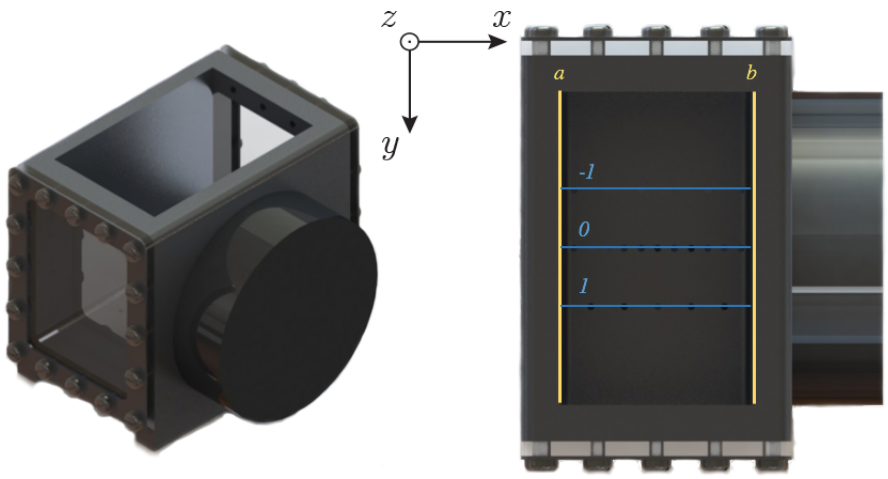

Figure 4.4: Preliminary test cell used for ground testing, isometric (left) and top (right) views.

The acoustic wave inside the test cell was generated with the same PZT that was mounted on the flight test cell. After switching on the output of the function generator, the PZT was left to work for about 10 minutes in order to ensure avoiding the transient state of the piezo during the measurements. The transient state was found to be almost negligible.

We interpolated the experimental data on every z-plane, obtaining the contour shown in Figure 4.5 (the remaining contours on different z-planes can be found in Appendix B).

From the different pressure distributions on different z-axis planes in Appendix B, it can be observed that the pressure increases as we get closer to the bottom of the test cell, then decreases again when reaching the bottom plane. Moreover, we also observe that there was a pressure antinode right at the opposite wall of the PZT, which confirms the presence of a standing wave inside the test cell. Due to the thickness of the hydrophone needle tip, the pressure cannot be measured exactly on the walls. From the pressure distributions obtained, regardless of small variations, the wave inside the cell was almost one dimensional.

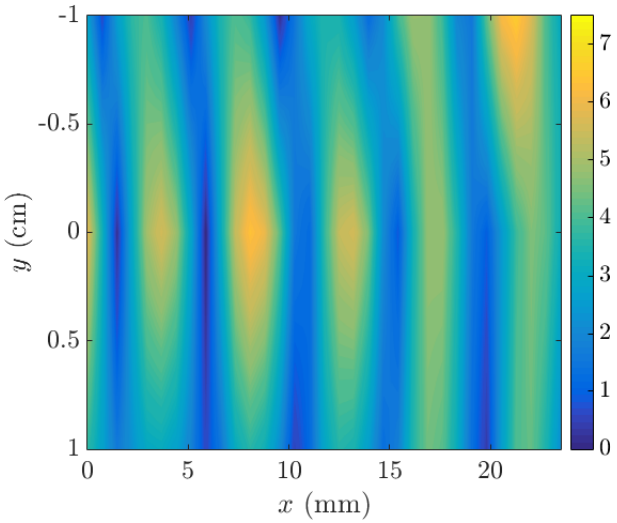

Figure 4.5: Pressure contour at 1 cm from the bottom of the test cell for $f = 167$ kHz (units in kPa).

The inner distance from wall to wall of the preliminary test cell was 26.6 mm, as measured with a caliper. Taking into account that the speed of sound, c, in distilled water at 20°C is 1482.36 m/s, the wavelength, λ, for $f = 167$ kHz is 8.876 mm. Hence, we can confirm that there were 3λ (26.6 mm) inside the test cell.

We plotted the contour of the yz plane at $x = 0$ (which was the closest point to the wall that we were able to measure). Overlaying it on a CAD drawing of the test cell (Figure 4.6), we could approximately associate the measured zone with the corresponding physical area, which helped us determine the final location of the injection orifice on that wall. Bubbles injected would be large enough that the acoustic field would push them to the nodes. The orifices were thus planned to be located at the points of maximum acoustic pressure (antinodes).

We also carried out a series of measurements on the preliminary and final designs of the test cell when the fluid has lower surface tension, i.e. solution of 0.1% of Zonyl FS-300 in distilled water. The measurements showed that the lower surface tension liquid does not have any major effect on the acoustic field, as it exhibited the same wavelength and same range of pressure values.

The final test cell was designed to have a width of 27.15 mm (3.03λ at 25°C), since we initially observed that the pressure response in the preliminary test cell was higher at 163.7 kHz. However, when we started testing on the final model, 167 kHz showed the highest response. This might be due to inaccuracies resulting from the ambient temperature, the exact width, or the width of the aluminium walls. Thus, the final frequency chosen for the flight configuration was 167 kHz.

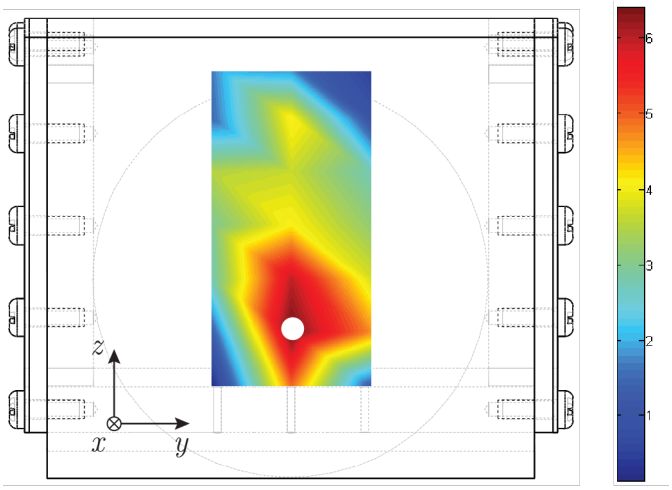

Figure 4.6: The acoustic pressure contour overlaid on the preliminary test cell CAD drawing (units in kPa). yz-plane on $x = 0$ (wall opposite to the PZT). The white circle denotes the injection orifice position.

From the measurements on these two cells, it was possible to determine the final location of the injection orifices. The lateral orifice was placed close to the area of maximum acoustic pressure in Figure 4.6. The orifices at the top of the cell were located close to the second and fourth maximum (antinode) from the PZT wall (Figure 4.7).

In parallel with determining the injection orifices of the test cell, we also carried out a theoretical study for estimating the flow rates, bubble detachment diameters (with and without acoustic field) and velocities.

First of all, we calculated the resonance radius corresponding to $f = 167$ kHz from the Minnaert equation (equation 1.5), obtaining $R_0 = 39.35$ μm, which means that the injected bubbles would most likely be larger ($R > R_0$) and would thus be located in the nodes of the pressure field.

In order to determine the flow rate and detachment diameter, we considered previous bubble injection experiments in microgravity. Carrera et al. (2006) observed detachment for all Weber numbers ($We = \rho_g v_g^2 d_C/\sigma$) on a plate orifice with a nozzle diameter of $d_C = 0.51$ mm. Pamperin & Rath (1995) observed detachment only for We>8 for an orifice of $d_C = 0.39$ mm, and neither did Tsuge et al. (1997) observe detachment for small flow rates. However, all of these works agree that the higher the flow rate, the lower the bubble detachment diameter in microgravity. This was important for our experiment, because we wanted to ensure that bubbles would not be larger than λ inside the tank and to also avoid a large amount of gas inside the cell by the end of the experiment.

In order to estimate of the relation between the detachment diameter and the

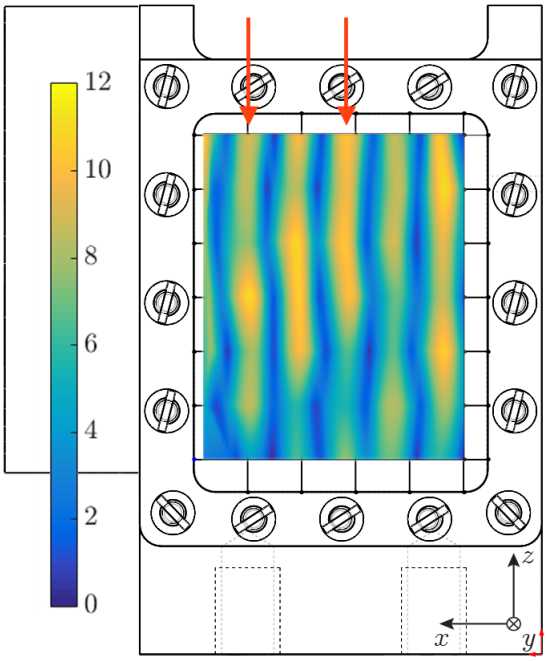

Figure 4.7: Overlay of the acoustic pressure contour on the final test cell CAD drawing (units in kPa). $f = 167$ kHz, xz-plane on $y = 0$ (centre of the cell). The red arrows show the selected positions of the injection orifices.

applied flow rates, we used Gaddis & Vogelpohl (1986) model. According to the review from Kulkarni & Joshi (2005), this is the most suitable for estimating bubble diameters in stagnant liquids. This model does not consider acoustic fields, which will be added in for the calculations. Their model assumes constant volumetric gas flow, quiescent liquid and spherical bubbles; and it also takes into account the buoyancy force F_{By}, surface tension force F_σ, drag force F_d and inertial force F_i. Moreover, they also consider the pressure force F_p and gas momentum force F_m, which can be neglected in our case since they are very small. In also considering the acoustic force (F_{Bj}), the force balance then becomes $F_{By} + F_{Bj} = F_\sigma + F_d + F_i$, where, from Gaddis & Vogelpohl (1986), the forces can be written as

$$F_{By} = \rho_l g V, \tag{4.1}$$

where ρ_l is the density of the liquid, g is the gravity and V is the bubble volume. F_{Bj} is presented in equation 1.7 as

$$F_{Bj} = -\frac{4\pi k R P_{ac}^2 \sin(2ky)}{\rho_l} \frac{1}{\omega_0^2 - \omega^2}, \tag{4.2}$$

where P_{ac} is the acoustic pressure amplitude, k is the wavenumber, y is the

position on the axis of propagation of the field, ω is the angular frequency of the incident field, ω_0 is the resonance angular frequency of the bubble with radius R,

$$F_\sigma = \pi d_C \sigma, \tag{4.3}$$

where d_C is the inner nozzle diameter and σ is the surface tension,

$$F_d = \frac{1}{2} C_d \rho_l v_b^2 \pi R^2, \tag{4.4}$$

where C_d is the drag coefficient, v_b and

$$F_i = (\rho_g V - \rho_l V_l) a, \tag{4.5}$$

where Q is the flow rate, ρ_g is the density of the gas, V_l is the liquid volume associated with the bubble motion and a is the bubble acceleration.

First of all, we solved the model at g_0 for water and for the low surface tension fluid, then compared the results with experimental data obtained from a low surface tension water-Zonyl solution (Figure 4.8). The estimation when an acoustic field was applied was also obtained (considering the obtained experimental acoustic pressures), but in g_0 $F_{By} > F_{Bj}$, and the effects of such a field on the bubble size are negligible.

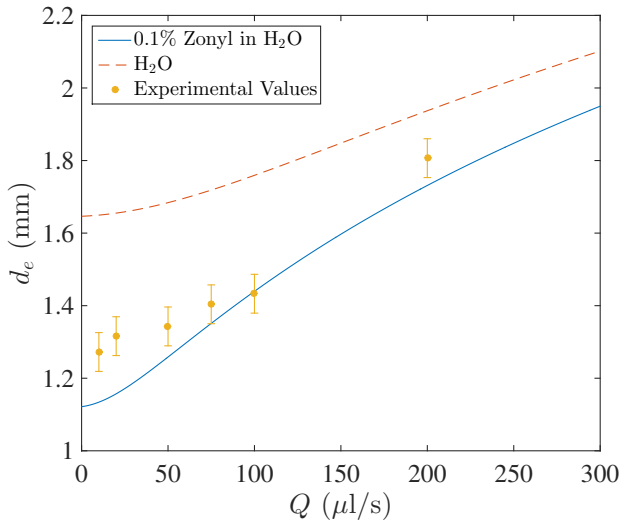

Figure 4.8: Detachment diameters as a function of the flow rate at g_0 without acoustic field, solving Gaddis & Vogelpohl (1986) model. Theoretical, water and Zonyl solution detachment, as well as experimental data for Zonyl.

If the detachment diameter in microgravity is considered (Figure 4.9), then applying an acoustic field in the test cell and assuming that the bubble resonance

frequency is much larger than the acoustic frequency ($\omega_0 \gg \omega$), the detachment diameters are around 5 mm for tubes with $d_C = 25$ µm and $d_C = 100$ µm. Assuming $p_{ac} = 12$ kPa, the largest detachment diameter for $d_C = 100$ µm would be 6 mm, and for $d_C = 25$ µm it would be 4.5 mm. If the amount of air injected were to obtain exactly 6 and 4.5 mm bubbles, we would run the risk that bubbles might not detach. Therefore, to ensure that bubbles would be detached in microgravity, we took into account bubbles that were 0.5 mm larger, which correspond to gas volumes of 44 µl for the 100 µm tube and 26 µl for the 25 µm tube. The syringe pump was configured to inject these volumes for 1 second; thus, the final flow rates used during the experiment were 44 µl/s and 26 µl/s.

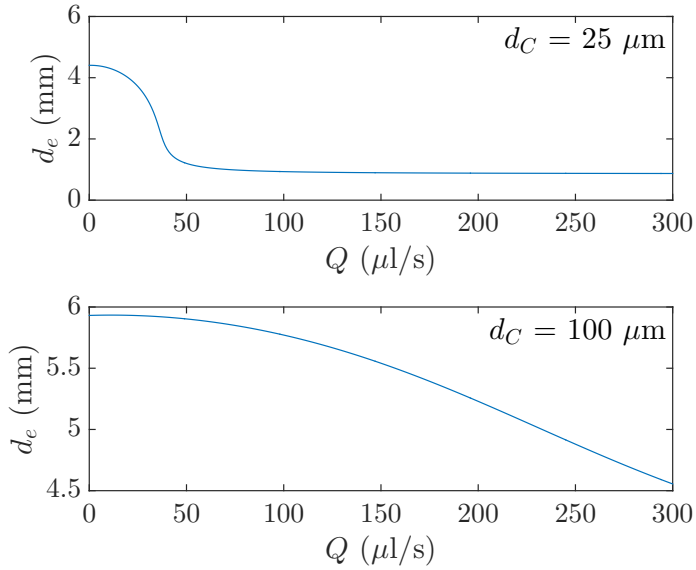

Figure 4.9: Theoretical detachment diameters in microgravity for inner nozzle diameters of 25 and 100 µm, and an acoustic field amplitude of $p_{ac} = 12$ kPa.

Knowing the range of potential detachment diameters, we calculated the approximate velocity they would have in microgravity conditions under an acoustic field, so that we can estimate the time between injections and switching the acoustic field ON and OFF. To do so, we considered that the only forces acting in microgravity once the bubble is detached would be the drag force (equation 4.4) and the Bjerknes force as expressed by Leighton et al. (1990), who used equation 1.7 and we consider $sin(2ky) = 1$ (value at the antinode), i.e. $\vec{F}_{Bj} + \vec{F}_d = \vec{0}$. This results in

$$v_b = \sqrt{-\frac{8kp_{ac}^2}{C_d R \rho_l^2 (\omega_0^2 - \omega^2)}}. \tag{4.6}$$

Figure 4.10 shows the results from equation 4.6 for different acoustic pressures at a frequency of $f = 167$ kHz and using Crum (1975) drag coefficient, $C_d = 27Re^{-0.78}$. It can be observed that the velocity values in microgravity are between 0.3445 and 22.4 mm/s. If we consider pressures between 1 and 12 kPa, we can estimate that the times for bubbles to move to the pressure node are anywhere from 0.19 s up to the slowest case 12.8 s, in the worst case (1 kPa).

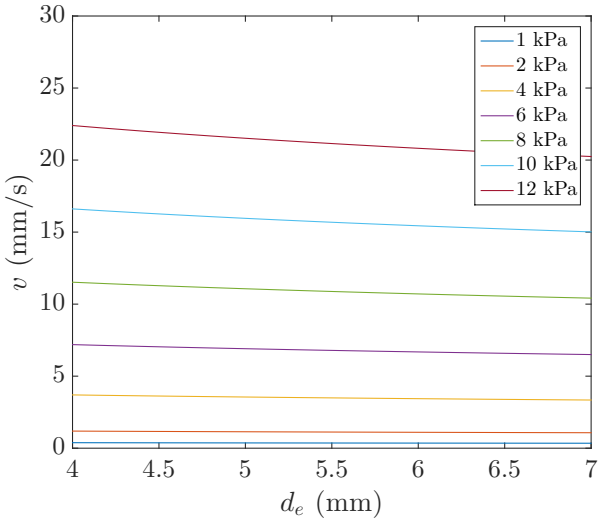

Figure 4.10: Bubble velocities in microgravity for the range of diameters previously found and different pressure values at 167 kHz.

Three different frequencies were chosen to be applied to the system during the microgravity phase. First there was the frequency close to the nominal of the PZT, 167 kHz (3λ inside), which would give the maximum pressure amplitude inside the test cell and would thus be used for detaching the bubbles. The other two frequencies were chosen in order to have 2λ (111.35 kHz) and λ (55.67 kHz) inside the test cell. These would be applied after bubble detachment. Even though the acoustic pressure for these two frequencies would be smaller because there would be no other force (apart from drag) acting on the bubbles in microgravity, the force from the field was assumed to be enough to displace the bubbles to the pressure nodes. These acoustic waves are represented in Figure 4.11.

Taking into account all the considerations above, the time for a bubble to move from one node to another (when changing from one frequency to a different one, distances marked by the green arrows in Figure 4.11), would be between approximately 35 ms and 3.5 s, depending on the distance and the velocity. Based on these frequencies and times, an experimental protocol could be designed for the flight.

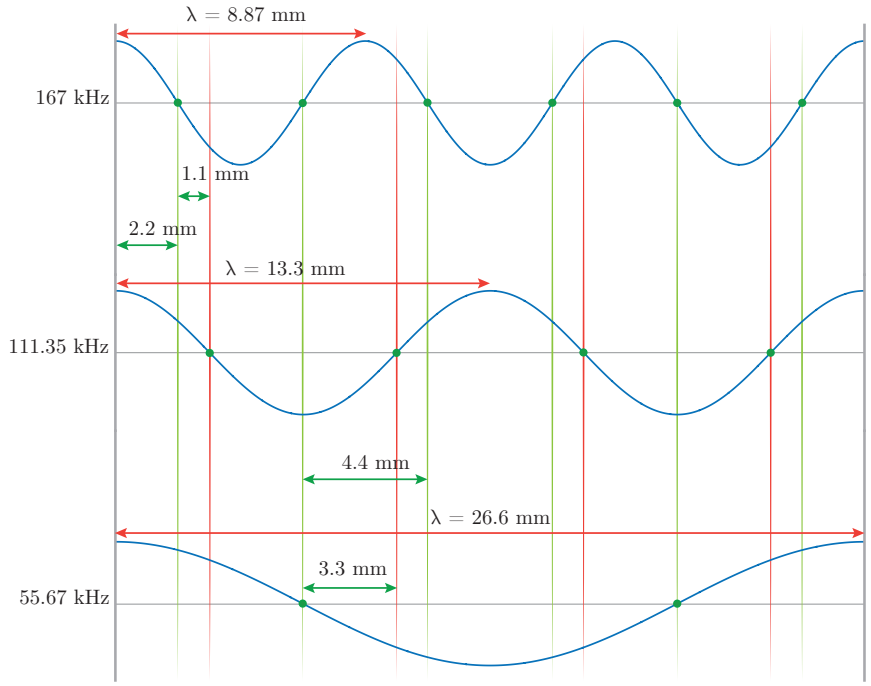

Figure 4.11: Conceptual drawing of the acoustic waves chosen to be applied inside the test cell in order to have 3λ, 2λ and λ.

4.2.2 Protocol

The preliminary study allowed us to carefully choose the parameters in order to optimise the available time of microgravity and to observe effects such as bubble detachment and bubble dynamics after detachment.

The nomenclature used for the injection outputs is shown in the list below. After testing, it was initially observed that a certain amount of air needed to be injected to build up pressure in the circuit (for the valve to let air go through).

- *Output 1.* Lateral, plate orifice. $d_C = 100\mu m$
- *Output 2.* Base, plate orifice. $d_C = 100\mu m$
- *Output 3.* Base, free-standing. $d_C = 25\mu m$

Table 4.2 shows the timeline of events for 190 s of microgravity. The total volume of air injected was calculated to be 2.67% of the total test cell volume.

4.2.3 Flight Campaign

The experimental setup and protocol were designed and built between December 2013 and June 2014, after which they flew on mission SL-9. The launch was originally scheduled for October 20, 2014, but due to adverse weather conditions it took place

Action	Time (s)	Acoustic field
Output 1		
Inject 250 µl/s	1	
Inject 44 µl/s	1	167 kHz
Wait	8	
Wait	4	off
Wait	4	167 kHz
Wait	4	off
Wait	4	111.35 kHz
Wait	4	55.67 kHz
Wait	4	
Inject 44 µl/s	2	167 kHz
Wait	8	
Output 3		
Inject 26 µl/s	5	167 kHz
Wait	5	
Wait	4	off
Wait	4	167 kHz
Wait	4	off
Inject 26 µl/s	5	
Output 2		
Inject 44 µl/s	1	167 kHz
Wait	9	
Wait	4	off
Wait	4	167 kHz
Wait	4	off
Wait	4	111.35 kHz
Wait	4	55.67 kHz
Wait	4	
Inject 44 µl/s	2	167 kHz
Wait	8	
Inject 44 µl/s	1	off
Wait	4	off
Output 3		
Wait	10	off
Inject 26 µl/s	10	167 kHz
Wait	5	off
Wait	5	111.35 kHz
Wait	5	off
Wait	5	55.67 kHz
Wait	5	off
Wait	5	167 kHz
Wait (booster separation)	20	off

Table 4.2: SL-9 experimental protocol showing actions and time.

on October 23, 2014 and reached an altitude of 124 km. The microgravity phase of the flight started at T+55 s. Three discrete signals were used, the first one at T+42.25 s activated the camera for recording, the second one at T+60.25 s was sent to activate the experimental protocol. Finally, a third discrete signal sent at T+502.25 s was used to switch off the camera. Booster separation occurred at T+240 s. Table 4.3 shows the sequence of events that took place during the campaign. Information about the rocket and loads can be found in Appendix A.

Time	Event
T-5 days	Liquid top-off
T-10 min	Power ON
	a. PC switched ON
	b. Arduino, syringe pump and function generator reset to begin a new experiment. LEDs switched ON
T	Launch
T+42.25 s	Discrete signal to start camera recording
T+60.25 s	Discrete signal to start experimental protocol shown in Table 4.2
T+502.25 s	Discrete signal to stop camera recording

Table 4.3: The sequence of events during SL-9's launch campaign.

After the payload was recovered, a preliminary view of the recorded video showed that the experiment did not work as expected. In a later analysis of the payload, it was discovered that there had been a hardware malfunction of the hard drive mounted in the computer. The data recovered showed that the experiment switched ON nominally and worked until T+3.33 s. Thus, the experimental protocol planned for the microgravity phase was never activated. Moreover, it was found that a large amount of gas of unknown origin was inside the test cell.

However, since we had a video during the flight showing liquid and gas in the test cell, we were able to extract information from the effects of rotation on two-phase flows. Data from the rocket spinning around the longitudinal z-axis was provided by UP Aerospace, Inc., and it is shown in Figure 4.12. This plot shows ω_z (the angular velocity of rotation) before and after de-spin, showing how the spin on the z-axis went from -2144 deg/s (357.33 rpm) to about 48 deg/s (8 rpm).

4.3 Results

In this section we present the results from the data recorded during the flight. We will first comment on the observations of the main effects. Afterwards, we will focus on some effects occurring during specific events of the flight in which the parameters are known (i.e. spin, de-spin, microgravity and booster separation). We will discuss

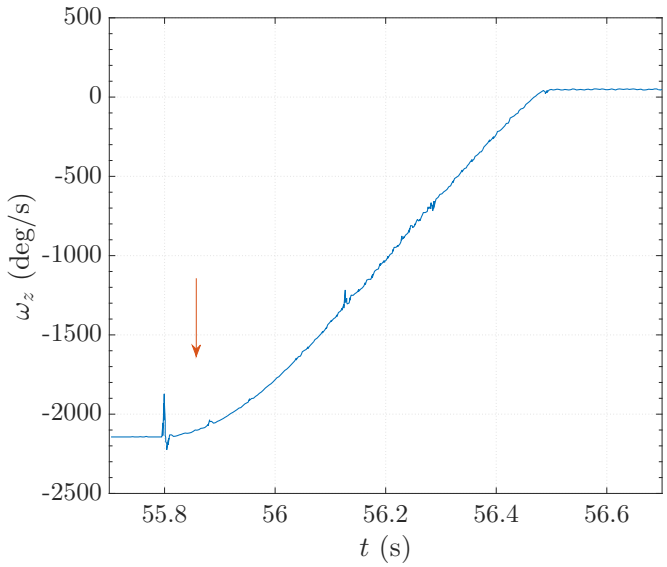

Figure 4.12: SL-9 ω_z during the time of de-spin (data provided by UP Aerospace Inc.). The arrow shows the time when the de-spin mechanism was deployed.

the actual position of the rocket's z-axis compared to the test cell axis, the effects of the rotation on the injected bubbles, and also the effects on the bubbles already present in the system.

4.3.1 Overview

The experimental setup had two main sets of output data. The first one was a 7 min 40 s video of the two-phase flow inside the test cell. The video was saved on a micro SD card in the camera, which could be recovered immediately after the flight. The second output data was a file stored in the computer and that contained the experiment accelerometer data as well as other relevant data for the analysis (flow rates, frequencies, etc.). However, it only saved data up to T+3.33 s, T being the launch time.

The observation of the behaviour of air bubbles together with the rocket accelerometer data were used to correlate the recorded video with the different stages of the flight.

Right at the beginning of the video, one can observe the effects of the force due to centripetal acceleration, which was generated by the rocket spinning at approximately 2144 deg/s. Liquid is pushed towards the outer walls and air towards the centre of the test cell, creating what looks like an air bridge (Figure 4.13 (left)). The bridge consists of a large central bubble connected to the walls through a foam-like cluster of smaller bubbles. The axis of the bridge is slightly displaced from the cen-

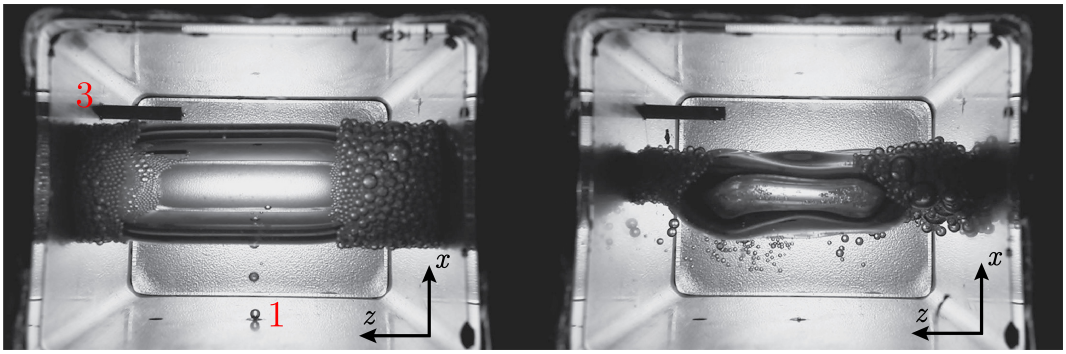

Figure 4.13: Stills of the test cell before (left) and after (right) de-spin. Orifices 1 and 3 are marked on the image, orifice 2 is covered by the column.

tral axis of the test cell. It appears to be displaced towards the camera lens (on the y-axis).

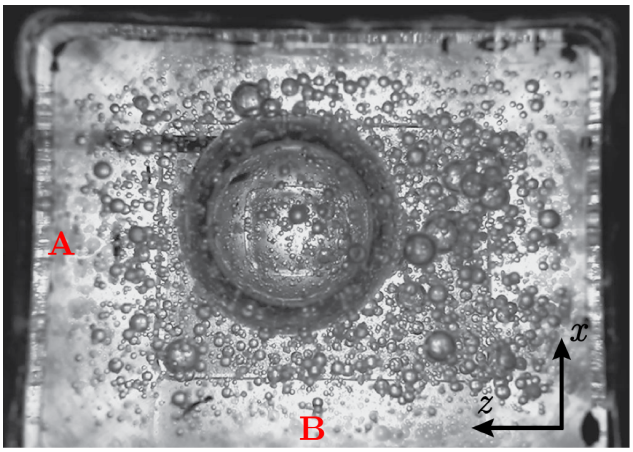

Figure 4.14: Bubble distribution 5 seconds after de-spin.

At the start of the microgravity phase, bubbles injected from the free-standing tube (output 3 in Figure 4.13) and bubbles injected from the plate orifice (output 1) have different sizes, the latter being larger than the former. This behaviour is expected, since the inner diameter of the orifice of the free-standing tube is 25 µm compared to the plate orifice's 100 µm.

Figure 4.13 (right) shows the air bridge right at the beginning of de-spin. The large cylindrical bubble noticeably revolves more abruptly around its axis, destabilises, detaches from the foam, and then recovers its stable spherical shape approximately 3 seconds later. The smaller bubbles clustered at the edges of the large bubble now scatter in the test cell, and most of them also showing a spherical shape (Figure 4.14). We will refer from now on to walls A (left) and B (bottom), as shown

in Figure 4.14.

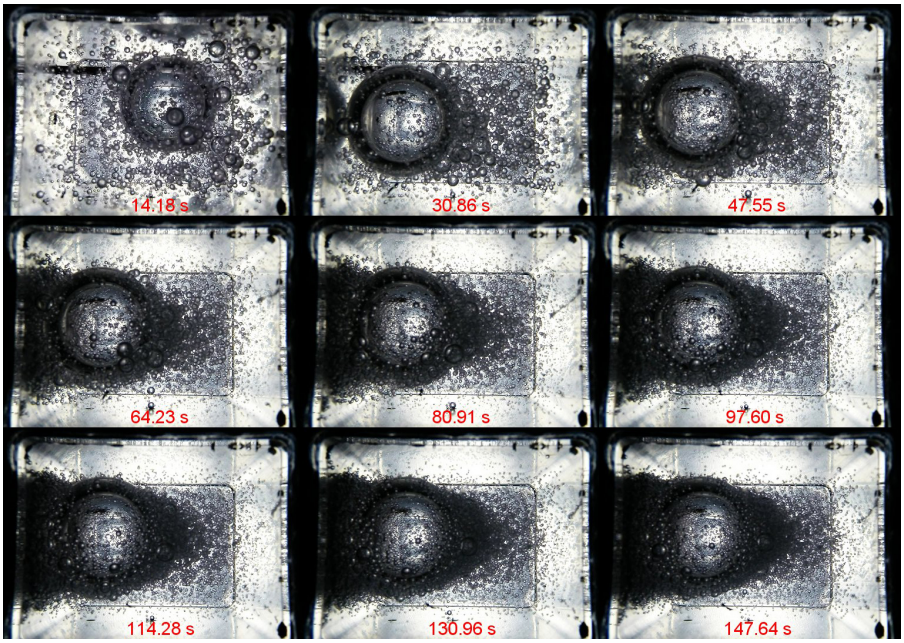

Figure 4.15: Evolution of the two-phase system during 2 minutes and 30 seconds. Time is shown in each frame.

Once the larger bubble shape is stable, the bubble slowly moves towards the free-standing tube, reaching wall A of the test cell. For the remaining time of microgravity, the smaller bubbles tend to cluster around the larger one, especially on the left and right sides in the picture, but less so around the centre of the bubble, i.e. as close to the rotation axis as possible. This can be clearly observed in Figure 4.15, where different snapshots of the test cell are shown over a period of 2 minutes and 30 seconds. Larger bubbles reach the largest bubble faster than the smaller ones, which is expected, since the centrifugal force is higher on larger bubbles.

After de-spin, smaller bubbles appear to swing side to side in a periodic movement caused by the force of centripetal acceleration, since the rocket is still spinning at a rate of 44 deg/s. In addition, the larger bubble slightly turns around the rocket's spin axis, which could also affect the bubble cluster movement. An overlap of the images showing the bubble cluster over one period is shown in Figure 4.16.

Aside from the general two-phase flow dynamics observed, bubble detachment from the orifices inside the test cell during microgravity is also observed. Bubble injection is clearly seen from the nozzle on wall A and from the plate orifice on wall B. Figure 4.17 shows the bubble injection from the plate orifice. Injection was also observed during the spin and de-spin phases.

In order to analyse in depth the observations explained above, we have separated

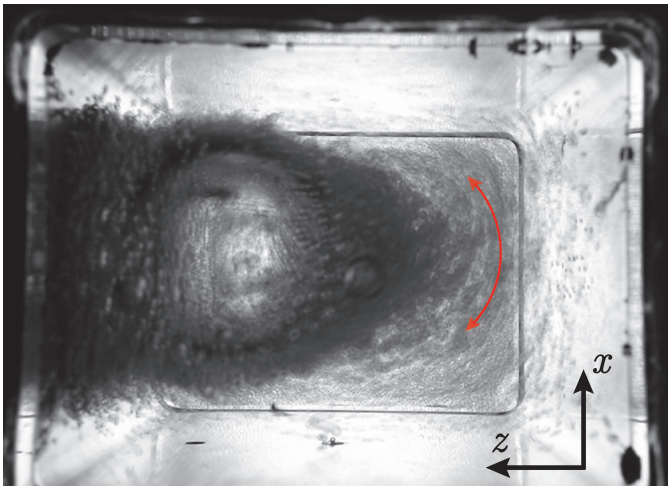

Figure 4.16: Overlap of the frames over a period of the swing motion.

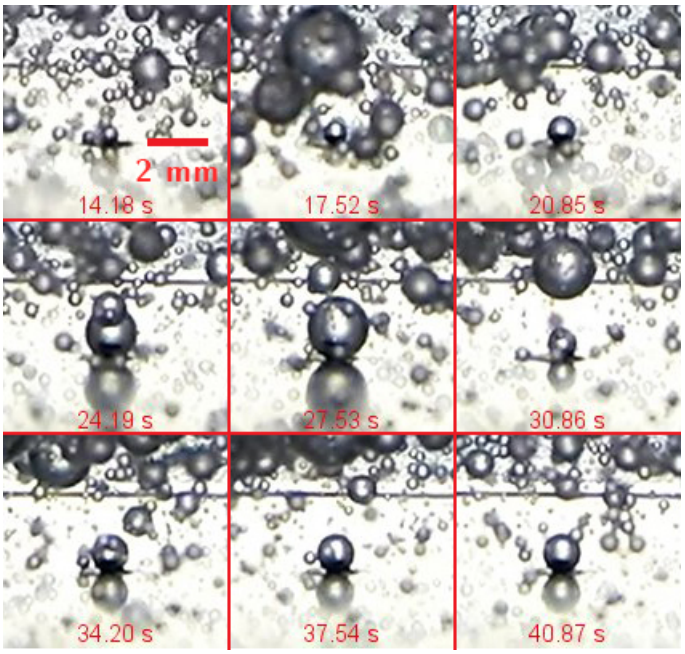

Figure 4.17: Bubble injection from the bottom wall orifice.

the phenomena depending on the flight stage in which they occurred: while the rocket is spinning before microgravity, during de-spin, during microgravity and at booster separation.

First, we will focus on the dynamics during the spin phase, specifically on the shape and position of the bubble bridge and on the bubbles detached from the 100

μm plate orifice. Not only do we study the trajectories and velocities of the bubbles, but we also measure their detachment diameters. Then we will look into the de-spin phase, analysing the trajectory of an injected bubble. During microgravity, we will study the behaviour of the bubbles while the rocket is still spinning. We consider bubbles already in the cell and bubbles injected from the plate orifice. Finally, we will study the booster separation phase, when bubble break-up is observed, and then compare it to the break-up observations from the SL-8 experiment.

4.3.2 Spin: Air Bridge Position

While carrying out the analysis of both detachment and rise, we realised that the air bridge described in section 4.3.1 is slightly displaced towards the camera (y-axis) and above the centre of the test cell on the x-axis. This offset between the rocket axis and the test cell axis could be noticed thanks to different observations. The free-standing tube on wall A and the plate orifice on wall B are both centred on the y-axis (depth) of the cell, which allows us to see that the bases of the free-standing tube and of the air bridge are not aligned. In addition, if the air bridge were at the centre, bubbles coming out from the free-standing tube would first bounce on the visible edge of the air bridge. Instead, they are injected from behind (which can be seen through the big bubble). A similar observation is possible with bubbles injected from the plate orifice reaching the air bridge surface.

The position of the bridge on the y-axis allows us to observe that the bubble rise trajectories are not straight but instead rise towards the camera. Moreover, the pix/mm resolution depends on the plane we are working on. By using perspective techniques, we can break down the test cell into different planes on the y-axis until we find the one crossing the bubble bridge, where its edges (i.e. the maximum diameter) touch the walls. This plane was measured at 10.75±0.67 mm. In Figure 4.18, a difference can be clearly observed between the plane corresponding to the centre (the plane crossing the free-standing tube and plate orifice) and the plane where the air bridge is located. Furthermore, Figure 4.18 shows the distances of interest for the following study, where $r_{top} = 12.39$ mm and $r_{bottom} = 14.76$ mm correspond to the radius from the axis of rotation (z) to the top and bottom walls, respectively. $d_1 = 2.4$ mm and $d_2 = 6.6$ mm are the widths of the foam at the bridge edges, which will be discussed later on. From this analysis, we have obtained the displacement on the x and y axes due to the misalignment of the z-axis of the rocket and the centre of the test cell. Therefore, it can be said that these two axes had an offset of $x = 1.185\pm0.137$ mm and $y = 10.75\pm0.67$ mm.

4.3.3 Spin: Bubble Detachment

In order to obtain a theoretical prediction of the detachment diameter, we take into account that the rocket is spinning at $\omega_z = 37.42$ rad/s around the z-axis. This

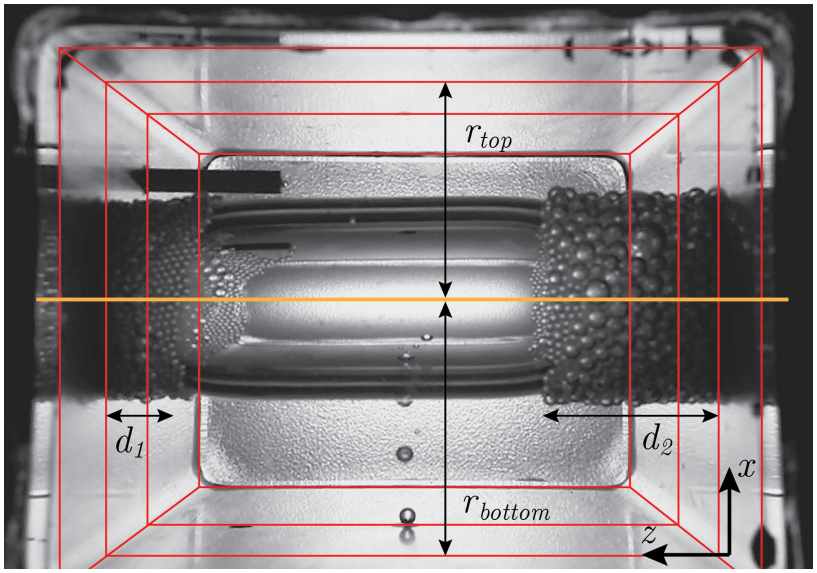

Figure 4.18: Scheme of the planes used to obtain the position of the centre plane of the test cell with respect to the plane of the air bridge. r_{top} and r_{bottom} are the radius from the z-axis to the top and bottom walls, respectively. d_1 and d_2 are the widths of the foam at the bridge edges.

rotation will generate a force on the bubbles, i.e. the centrifugal force $F_c = \rho_l a_c V$ (where $a_c = \omega_z^2 r$ is the centrifugal acceleration), then:

$$F_c = \frac{1}{6}\pi\rho_l\omega_z^2 r d_e^3, \tag{4.7}$$

where r is the radial polar coordinate and d_e is the detachment diameter.

Taking into account that the rocket is no longer accelerating and is close to entering the microgravity phase, we can assume that $g < 10^{-1}$ and, thus, $F_c \gg F_{By}$ (buoyancy force). Hence, neglecting inertia, the only forces acting upon detachment are the surface tension force $F_\sigma = \pi d_C \sigma$ (where d_C is the inner diameter of the orifice) and F_c. When the bubble detaches from the nozzle, $F_c = F_\sigma$. By isolating the diameter, we can obtain the theoretical prediction for the detachment diameter:

$$d_e = \left(\frac{6 d_C \sigma}{\rho_l \omega_z^2 r}\right)^{1/3}. \tag{4.8}$$

For $r = 18.26$ mm (the radius from the axis of rotation to the plate orifice), the theoretical prediction for the detachment diameter is $d_e = 0.815$ mm. The experimental diameters measured (on 14 bubbles) oscillate between $0.357 \pm 0.104 < d_e < 1.069 \pm 0.104$ mm. A hypothesis for such a large range of measured diameters could be that the injected gas is generated by pressure differences in the gas circuit (from

the syringe to the test cell, through the anti-return pressure valve). The pressure valve opens when enough gas pressure has built up. Different gas overpressure leads to different sized bubbles.

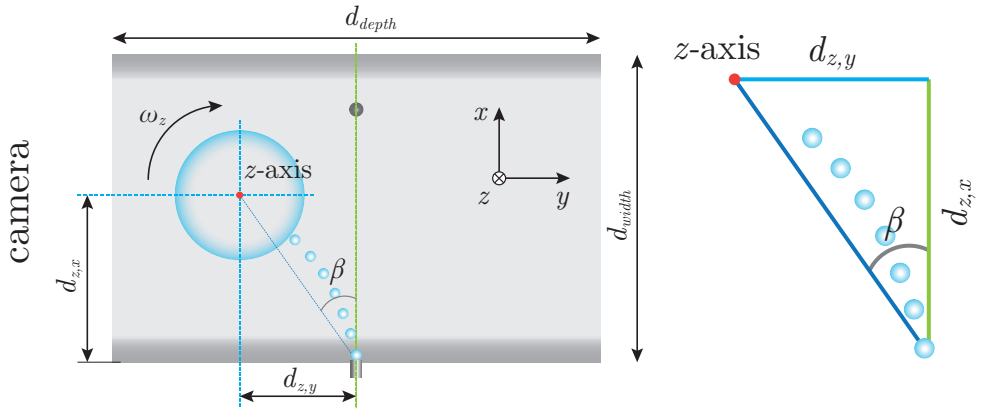

Figure 4.19: Scheme of the xy-plane inside the test cell (from the wall opposite the free-standing tube), showing the different distances to take into account in order to obtain the value of the angle β (angle between the central plane of the test cell and the radius to the z-axis). In this scheme, $d_{z,x} = r_{bottom}$ from Figure 4.18.

4.3.4 Spin: Bubble Motion

In order to measure the bubble displacement, we need to take into account the distances shown in Figure 4.19, where $d_{depth} = 43$ mm and $d_{width} = 27.15$ mm, which are the inner dimensions of the test cell. Angle β is defined as the angle between $d_{z,x}$ and the distance from the center of the air bridge to the injection point. In order to know β, we need to know the distances $d_{z,x}$ and $d_{z,y}$, which are defined as the distances from the injection orifice to the center of the bridge on the x-axis and y-axis, respectively. $d_{z,x}$ and $d_{z,y}$ have already been obtained in Section 4.3.2 and are 14.76 mm and 10.75 mm, respectively. Thus, angle $\beta = \arctan(\frac{d_{z,y}}{d_{z,x}}) = 36.07°$.

Assuming that the injected bubbles move in the radial direction, we have obtained the radial displacement. Figure 4.20 shows the position (a), velocity (b) and acceleration (c) of the 14 injected bubbles in the radial direction. Note that $r = 0$ is the axis of rotation. We can separate the trajectories in three groups corresponding to different bubble radii: the three longest paths correspond to the smaller bubbles with an approximate diameter of $d_e \simeq 0.36$ mm, then there is a single trajectory (in blue) that corresponds to a bubble of $d_e \simeq 0.77$ mm. Finally, the remaining shorter trajectories correspond to bubbles between $d_e \simeq 0.9$ mm and $d_e \simeq 1.07$ mm.

First, we observe that bubbles do not reach a terminal velocity. To know how close these velocities are to their theoretical terminal velocity, v_t, we use the model from Mendelson (1967); Tomiyama et al. (1998), which considers bubbles as interface

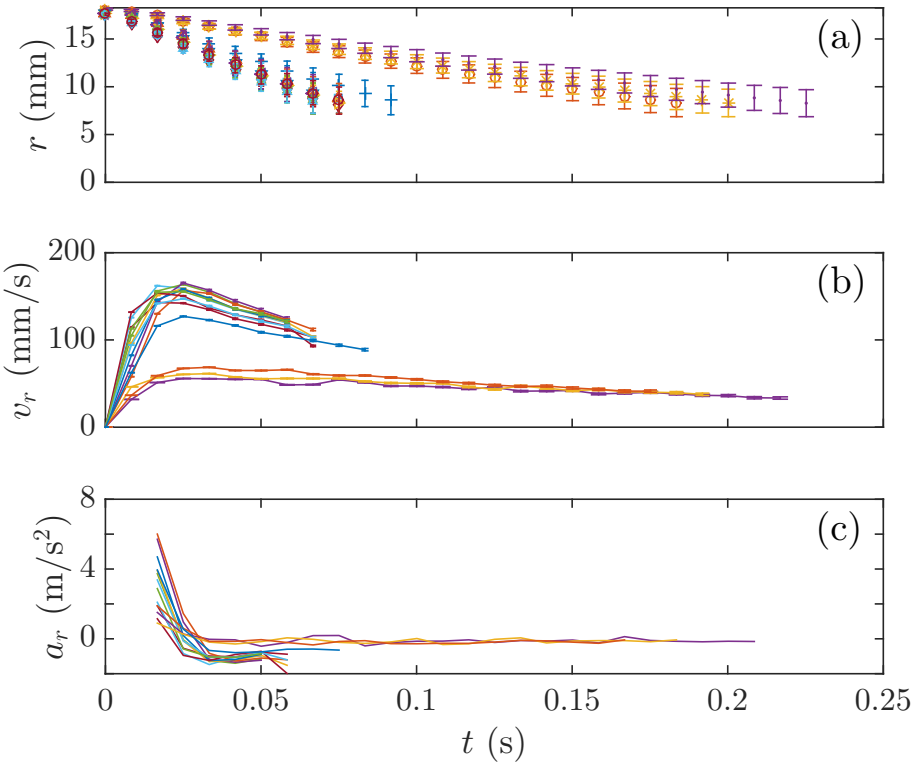

Figure 4.20: (a) Position, (b) velocity and (c) acceleration of the bubbles in the radial direction.

disturbances similar to a wave propagating in an ideal fluid. Substituting g with the centrifugal acceleration a_c, we obtain:

$$v_t = \sqrt{\frac{2\sigma}{\rho_l d_e} + \frac{\omega_z^2 r d_e}{2}}. \tag{4.9}$$

It should be noted that this equation generally agrees with experimental data (Mendelson (1967), Kulkarni & Joshi (2005), Suñol & González-Cinca (2015)), except in the case of bubbles with a diameter of $d_e \leq 0.5$ mm (Kulkarni & Joshi (2005)). Figure 4.21 shows the terminal velocity predicted by equation 4.9 for different experimental d_e as a function of the distance of the bubble to the axis (here $r = 0$ is the z-axis), i.e. at different accelerations depending on their distance from the rotation axis. It should also be noted that for $d_e \simeq 0.36$ mm and $d_e \simeq 0.58$ mm (the latter will be discussed later, since it corresponds to the diameter of a bubble injected during de-spin), equation 4.9 is not valid.

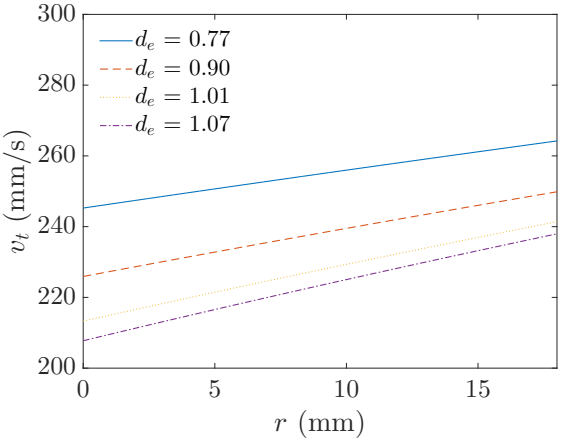

Figure 4.21: Terminal velocity as a function of the radial distance to the center, from equation 4.9 for different experimental values of d_e.

From Figure 4.21, we can draw the conclusion that none of the experimental bubbles reached their expected terminal velocity. Instead, bubbles detach from the nozzle and continue to rise to the axis of rotation following a slowed down trajectory.

In order to analyse the decelerating behaviour observed, the forces acting on a bubble inside a rotating fluid in microgravity need to be considered. Siekmann & Johann (1976) carried out an analytical and experimental study (in simulated weightlessness) for a gas bubble migrating in a rotating fluid. The forces acting on the bubble in a rotating fluid on ground are inertia, drag, centrifugal force, gravity and Coriolis force. They consider that the drag force is proportional to the flow velocity but acts in the opposite direction. If the case of steady motion in weightlessness is considered and assuming small rotation rate in polar coordinates (r,φ), the force balance simplifies to drag force and centrifugal force in the radial coordinate, and to Coriolis force and drag force in the angular coordinate

$$0 = -mr\omega_z^2 + F_{dr}, \tag{4.10}$$

and

$$0 = 2m\dot{r}\omega_z^2 + F_{d\varphi}, \tag{4.11}$$

where $F_{dr} = -K\dot{r}$ and $F_{d\varphi} = -K\dot{\varphi}$ are the drag forces in the radial and transverse direction, respectively. The dot represents the time derivative and K is a constant ($K > 0$) that depends on the drag. Rearranging equations 4.10 and 4.11, and integrating with respect to time

$$r = r_0 \exp\left(-\frac{m_l\omega_z^2}{K}t\right), \tag{4.12}$$

and

$$\varphi = \varphi_0 - 2\frac{m_l^2 \omega_z^3}{K^2} t, \tag{4.13}$$

where subscript 0 denotes initial conditions, $m_l = \frac{4}{3}\pi R^3 \rho_l$ is the mass of the displaced liquid and t is the time. Siekmann & Johann (1976) related K to the Stokes law. However, this law is not applicable in our experiment, since we are in the range of $Re > 2$ (Kulkarni & Joshi (2005)). Taking into consideration the velocities and diameters obtained earlier, we can observe that the Reynolds number ($Re = vd_e/\nu$, where v is the velocity of the bubble and ν is the kinematic viscosity) for our experimental values is between $13.34 < Re < 187.74$. Thus, we have fitted the experimental data to the solution from equation 4.12, considering K as a free parameter that depends on the diameter of the bubble, since drag increases when the diameter increases. Once K is obtained from the fit, we calculate the theoretical trajectories of the bubbles using equations 4.12 and 4.13.

The results from equations 4.12 and 4.13 can be observed in Figure 4.22. Even though these equations are derived for small rotation velocities, we have observed that they are in agreement with our experimental data, both for obtained the values of K and at large rotation velocities.

4.3.5 Spin: Rotating Air Bridge Shape

Another effect to consider while the rocket is spinning is the shape of the air bridge, which thus requires estimating the positions of its edges. The large bubble in the video does not appear to reach the walls, although it cannot be observed due to the clusters of bubbles on both edges. Since the position of the bubble rotation axis is known, we can measure the bubble bridge radius, which is 5.74 mm.

For a bubble at the axis of a rotating liquid, Rosenthal (1962) derived an inequality from which the maximum radius of the bubble (R_b) can be obtained when the capillary force balances both the centripetal force and the effect of the pressure difference on the axis of rotation

$$R_b^3 \omega_z^2 (\rho_l - \rho_a) < 4\sigma. \tag{4.14}$$

According to this expression, a free floating bubble in a rotating liquid with the surface tension and angular velocity of this case should have a maximum radius of 4.04 mm. However, the bubble in our system is constrained at the tips, which could be the cause of a slightly larger radius, but it is still within the same order of magnitude as the calculation.

We present here three methods for estimating the length (l) of the bubble. By comparing the results obtained from each method, we will know whether the values are a good estimation of the actual size of the bubble.

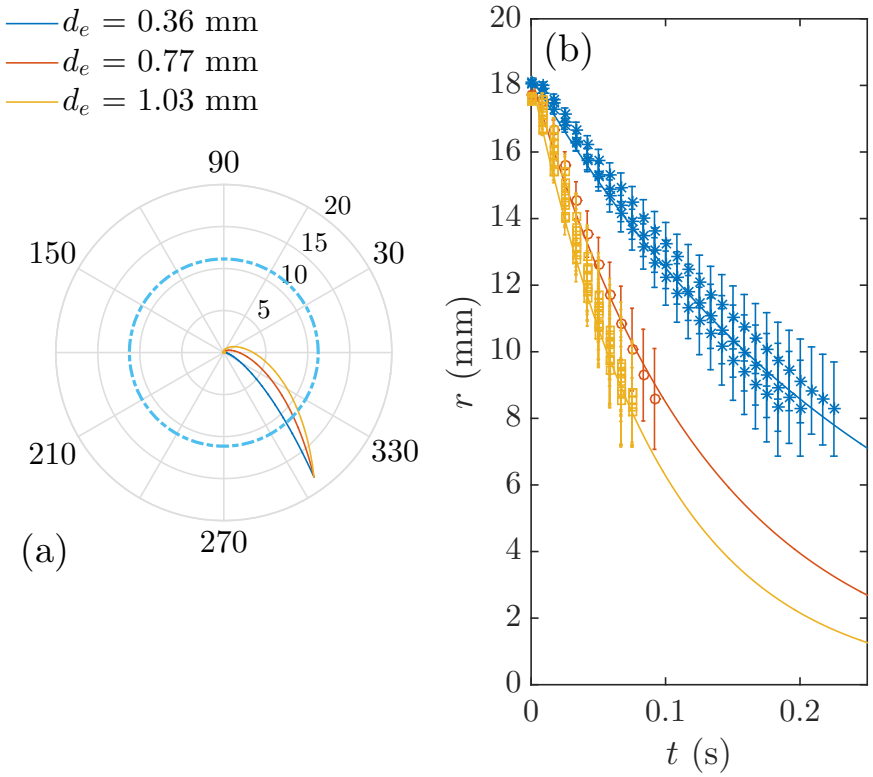

Figure 4.22: Solutions from equations 4.12 and 4.13. (a) Polar graphic of the trajectories from its injection point. The dashed line shows the approximate location of the bubble bridge surface. (b) Time evolution of the r coordinate, experimental data (points) and theoretical prediction (lines).

The first method is by observation, roughly determining the value from the video. The surface of the large bubble bridge in the video starts to curve when the bridge touches the foam (Figure 4.23). By fitting different curves at each end to consider different curvatures of the edges, we were able to estimate the length of the bridge at 26 mm $< l <$ 30 mm.

Second, we measured the length that a cylinder would have with the same volume and radius as the bridge. We have measured the volume (2.77 ml) of the bridge after de-spin, which is the same as during spinning since no coalescence or break-up were observed in either of the processes. In this case, for a cylinder, we have obtained $l = 26.746$ mm.

Finally, we considered the volume equation demonstrated by Rosenthal (1962) in order to obtain the equivalent length,

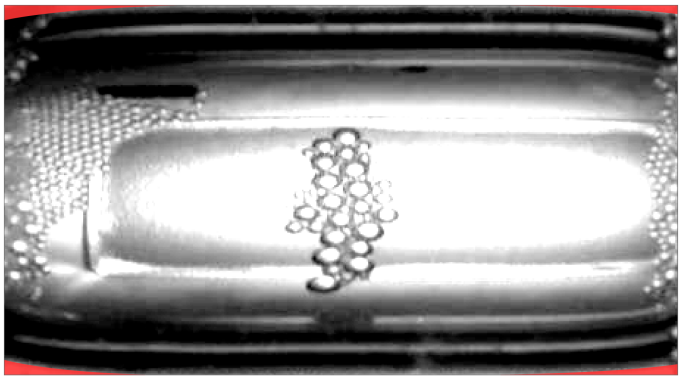

Figure 4.23: Air bridge fitted into a rectangle. The red corners mark the curvature at the edges.

$$V = \frac{2\pi R_b^3}{3e}\left(\frac{(1+e)l}{2R_b} - 1\right), \tag{4.15}$$

where e is a parameter that increases as the angular velocity increases, and it lies between $0 \leq e < 0.5$. According to this research, the bubble is close to cylindrical when the angular velocity is very high, and the l/R_b ratio is higher when e is close to 0.5. Thus, isolating l from equation 4.15, and assuming that we are close to $e = 0.5$, we obtain $l = 26.754$ mm. In order to have an idea of the bubble length, we have overlaid (Figure 4.24) an estimation of the bubble shape, taking into account the radius, length and the slight curvature observed on the edges mentioned before.

Considering the values in Figure 4.18, $d_1 = 2.4$ mm and $d_2 = 6.6$ mm, we confirm that the bubble bridge is not in contact with the walls, as observed in the images.

Figure 4.24: Overlay of the bubble shape on the bubble bridge.

4.3.6 De-Spin: Bridge and Bubble Cluster Destabilisation

De-spin occurs between T+55.795 s and T+56.5 s, the time during which the bridge and the clusters of bubbles destabilise, as explained in section 4.3.1. Also, another bubble is injected from the plate orifice. After de-spin, the rocket keeps spinning in the opposite direction but at a much lower rate, $\omega_z = 48$ deg/s. Right after the system de-spins, the larger bubble takes about 3.15 s to stabilise.

We have not found any particular mode of oscillation for the bridge as the de-spin occurs. However, the shape of the bridge is similar to previously reported shapes by Leslie (1985) for cases in which surface tension is dominant.

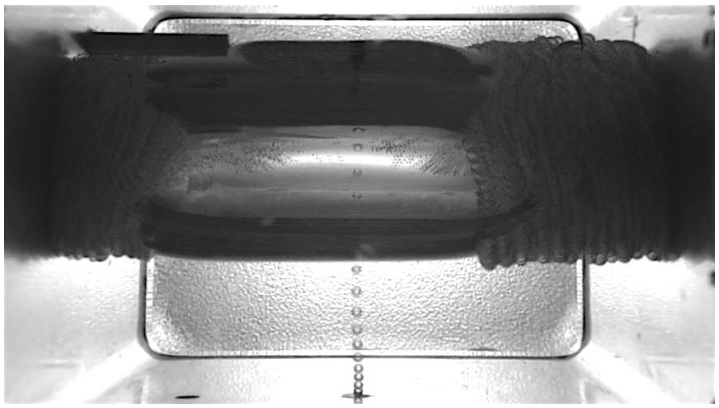

Figure 4.25: Sequence of images of the system during de-spin. The time step between each image is 1/120 s.

During de-spin, we have also observed the detachment and rise of a bubble from the plate orifice. Figure 4.25 shows an overlay of the frames during 0.15 s, where we can see the bubble rising and moving towards the bubble bridge. Later, it appears to continue on its trajectory around the surface of the bridge, since the bridge starts to rotate and deform. Figure 4.26 shows the measured trajectory, velocity and acceleration of the bubble -assuming that, as with the previous bubbles, the bubble moves towards the axis of rotation. It can be seen that the bubble accelerates during de-spin but does not reach its terminal velocity (Figure 4.21) at any distance from the center.

4.3.7 Microgravity: Bubble Motion

During microgravity, the bubble bridge moves to wall A (following the nomenclature in Figure 4.14). Since the rocket was still spinning (although at a much lower angular velocity), the bubble slightly spins around the axis of rotation, which generates a flow inside that sweeps the remaining smaller bubbles along.

Depending on their size, bubbles tend to agglomerate gradually around the z-axis

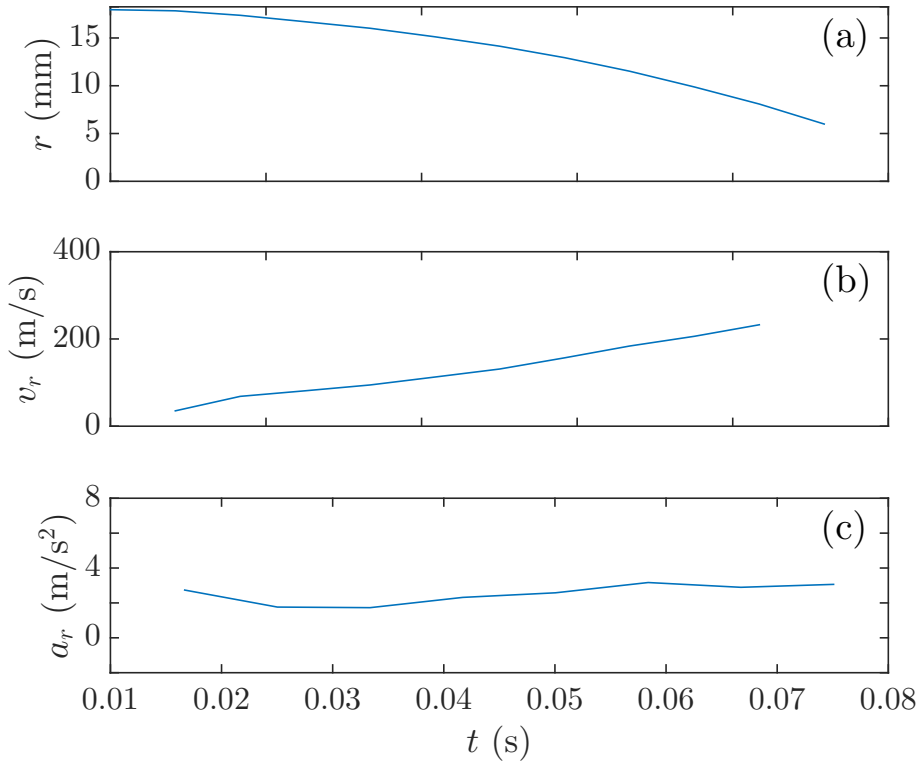

Figure 4.26: (a) Trajectory, (b) velocity and (c) acceleration of the bubble rising towards the bridge during de-spin.

of the larger bubble; i.e. larger bubbles travel faster than smaller bubbles. This can be observed in Figure 4.15.

The largest bubble moves around the z-axis on the xy-plane. Its motion was manually tracked for 40 s by fitting a circle and registering the position of the centre. The trajectories were filtered in MATLAB to remove the noise. Since the bubble is constantly changing planes, the resolution changes accordingly. Nevertheless, even without considering the change in resolution, some information about the frequency can be extracted from these tracks. We have obtained the motion on the x-axis and the projection of the y-axis motion on the z-axis.

The obtained tracks can be seen in Figure 4.28. These tracks show that the bubble does indeed have an oscillating motion in the x and y axes, whose frequency is $\omega_z = 42.98 \pm 0.31$ deg/s. However, the tracks allow us to obtain information that was not obvious from mere visual observations. First, if we look specifically at Figure 4.28b, the amplitude of the motion decreases with time, which can be attributed to the smaller bubbles agglomerating around the larger bubble. Second, it is observed

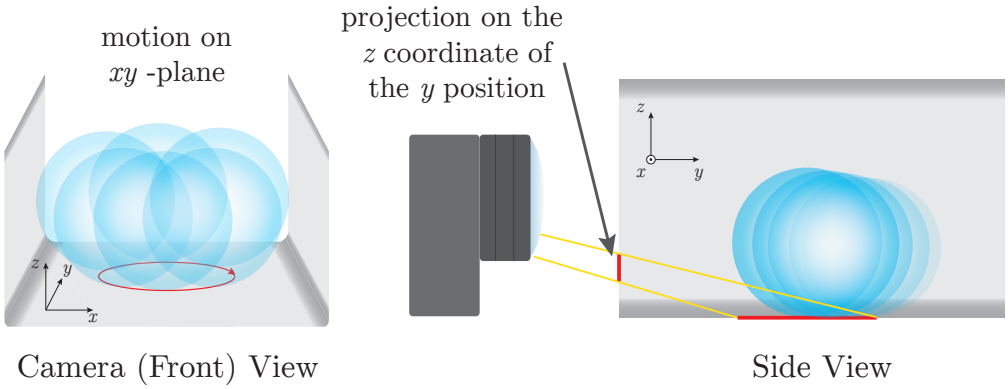

Figure 4.27: Scheme showing the projection of the y position on z.

in Figure 4.28c that the motion is not centred around the z-axis, which might be due to the residual gravity of about $10^{-2}g_0 \sim 10^{-3}g_0$ on the three axes.

Similar behaviour was reported by Siekmann & Johann (1976), who observed circular paths when rotating a fluid in the presence of residual gravity ($10^{-2}g_0$) on one axis.

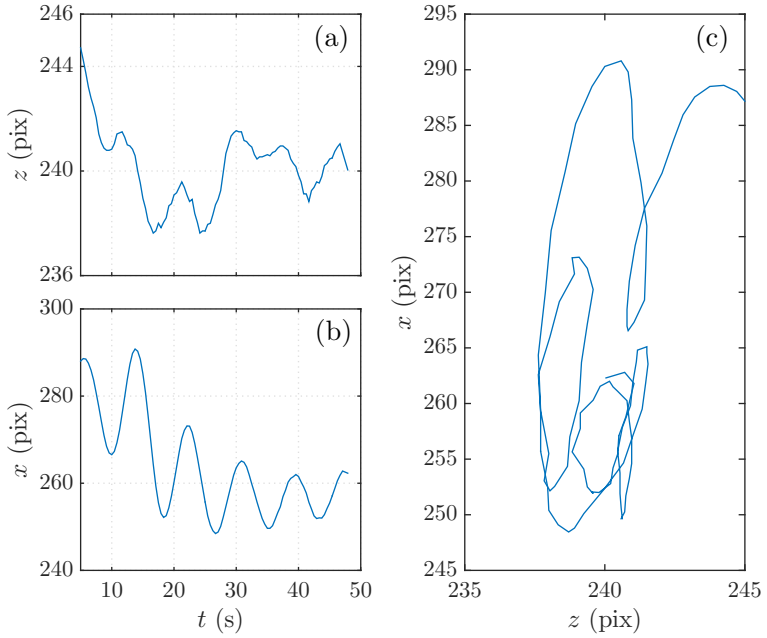

Figure 4.28: Time evolution of the larger bubble position. (a) Projection of the y position on the z coordinate (a). (b) x coordinate of the position. (c) Trajectory of the bubble.

The trajectory of bubbles moving towards the axis of rotation were also measured. The trajectories of a bubble injected from the plate orifice and moving towards the larger bubble is shown in Figure 4.29. The z component of the trajectory (Figure 4.29a) oscillates. We measured the frequency of these oscillations and obtained $\omega_z = 43.11 \pm 0.1$ deg/s (0.75 rad/s), which is very close to the value provided by UP Aerospace on the spin of the rocket: $\omega_z = 44$ deg/s. Moreover, the frequency is the same as the one measured for the larger bubble, confirming that the motion of the smaller bubbles is due to the disturbance generated by the larger bubble in the fluid.

Furthermore, it is observed in both Figure 4.29a and 4.29b that the amplitude of the oscillation increases as the bubble approaches the cell's axis of rotation. In addition, the motion of the bubble is not that of a zig-zag motion but of a spiralling motion.

These observations are important to take into account for future experiments, since the rocket spin may cause undesirable effects on the experiments.

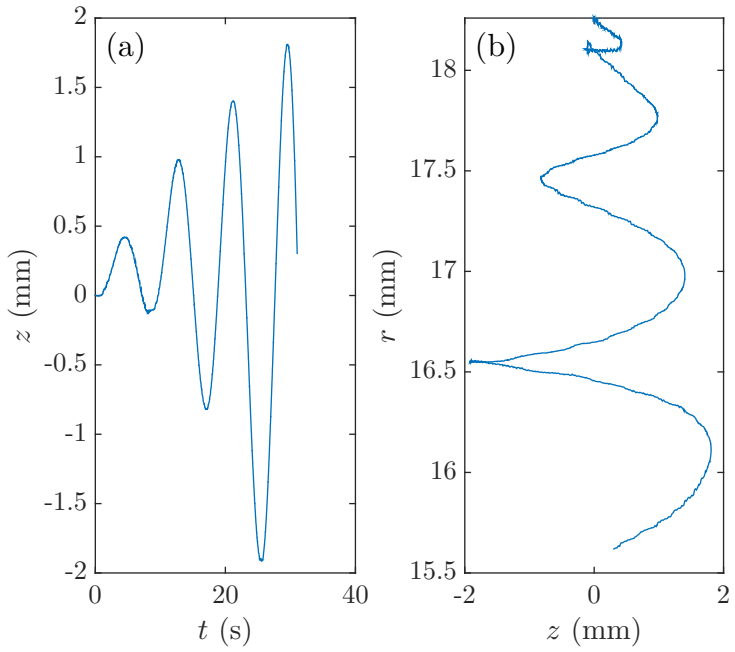

Figure 4.29: (a) Time evolution of the z coordinate, and (b) trajectory of a bubble injected from the bottom plate orifice during microgravity.

4.3.8 Booster Separation: Bubble Break-up

Following the analysis carried out on the SL-8 experiment (Section 3.4.4), we also observed the dynamics of the bubble and the cloud of smaller bubbles when the

booster separated. Moreover, the smaller bubbles serve as a guide for observing the liquid flow direction during the process. Since the bubble was spinning around the axis of rotation at all times, it was centred enough for it to deform through the middle and break up (much like the conceptual sketch shown in Figure 3.13).

Figure 4.30 shows the image sequence of the bubble breaking up. Considering that the test cell had a different shape than those in the Chapter 3 cells, the bubble first flattens on the surface and then most of the air is displaced to the sides, making the central part of the "U" thinner every time, until the two parts separate. The bubble breaks into two smaller bubbles, one slightly larger than the other. They recover their spherical shape faster than in the previous experiment. It should be noted that the volume ratio between the bubble and cell is $V_b/V_{cell} = 0.37$ in SL-8 and $V_b/V_{cell} = 0.066$ in the present experiment, which significantly reduces wall effects in the last case.

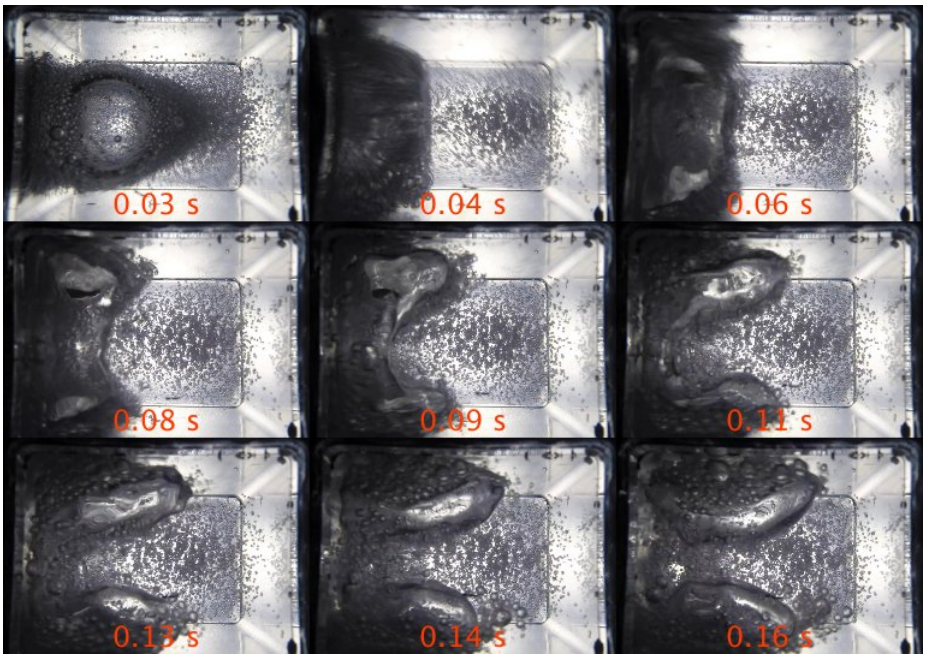

Figure 4.30: Image sequence at the moment of booster separation, showing the larger bubble breaking up.

4.4 Conclusions

In this section we have presented an experimental setup that was designed and built to generate bubbles and acoustic fields in microgravity conditions. The setup was adapted to the required microgravity platform, which greatly reduced its original

volume, and it will be used for future experiments to study the effects of acoustic fields in microgravity.

Ground testing and calculations were carried out to optimise the available time in microgravity while also planning the experimental protocol to be applied during the available microgravity time.

Even though a technical fault led to the experiment not working as expected, the fact that the camera was independent from the PC allowed us to obtain a video from the phenomena inside the test cell during the time between take-off and reentry.

We reviewed the main phenomena that took place in the test cell and have concluded that the injection was most likely due to unaccounted pressure differences in the experimental setup. By coupling our video data with the data from the launch provider's Inertial Measurement Unit, we were able to link the different parts of the video to the events in the flight.

While the rocket was still spinning at a very high angular velocity, bubbles were injected from two visible orifices in the cell, which caused the gas inside the cell to agglomerate around the axis of rotation in a form that visually appears similar to an air bridge. The larger volume of air was surrounded by two clusters of bubbles on its edges that separated it from the walls.

When the rocket's de-spin system was deployed, the angular velocity decreased drastically. Bubbles that were located at the rotation axis destabilised, and another small bubble was simultaneously injected from the plate orifice before following an accelerated trajectory towards the center. Afterwards, all the bubbles in the system recovered their spherical shape.

After de-spin, the rocket continued to rotate at a much lower angular velocity. In this phase, bubbles in the cell moved in an oscillating motion. The larger bubble located itself at wall A of the cell, while the remaining bubbles agglomerated around it (especially at the tips of the bridge). Smaller bubbles took a longer time to reach this position than larger bubbles.

We analysed some of the phenomena in each stage of the flight. During this analysis we observed that the axis of rotation was displaced from the axis of the test cell on the y and x axes. By means of drawing techniques, we were able to locate the position of the rotation axis of the bridge.

The trajectories of the injected bubbles and the estimated bubble detachment size were obtained. The different detachment diameters obtained are attributed to pressure differences in the injection system. However, most of the diameters were of the same order of magnitude as the theoretical prediction. Rising bubble trajectories were measured, and we observed that no bubble reached a terminal velocity. In addition, we found good agreement with the analytical predictions of the trajectory, even though our experiment had a high rotation rate.

During microgravity, the rocket still rotated at a lower frequency, which subjected the bubbles inside the test cell to centrifugal force. It was observed that the larger bubble spun around the axis and, as the remaining bubbles agglomerated around it,

the amplitude of its movement decreased. Moreover, this motion was also influenced by the residual gravity on the three axes, as was observed in the past. These effects during microgravity are important to take into consideration in future experiments using the same platform, since they can condition the bubble dynamics.

The last effect observed was bubble break-up, which showed dynamics similar to the observations in the SL-8 experiment. In this case, the bubble broke up into two almost equal parts that quickly returned to sphericity. Wall effects were reduced in this experiment, since the ratio between the bubble volume and the test cell volume was smaller in comparison to SL-8.

Chapter 5

Effects of Hypergravity and Acoustic Fields on Two Phase Flows

This chapter presents an experimental and numerical analysis of rising bubbles at gravity levels higher than $g_0 = 9.8$ m/s^2 while applying acoustic fields. In the experiment, bubbles were injected from a nozzle, and acoustic fields were applied in two directions and with different acoustic pressures. Different effects were observed, including bubble levitation. The acoustic field caused bubbles to detach at smaller sizes than without the field. Moreover, the rising paths were highly dependent on bubble size and the field that was applied, even at high gravity levels. Furthermore, due to the high flow rates used for bubble injection, bubble trains were observed, thus affecting the rise velocity due to the wakes of the bubbles being so close to each other. We have carried out a numerical analysis that qualitatively agrees with the experimental results.

5.1 Introduction

Physical phenomena in hypergravity is not very well known, even though two-phase systems in space applications are usually subjected to gravity levels that are different than those of microgravity. Bubbles rising in fluids can easily be found in a large variety of situations, from simple daily objects (e.g. bubbles in a glass of sparkling water) to technologically sophisticated devices (e.g. bubble column reactors). Each of these systems operates in very different conditions; for instance, the liquid fuel in a rocket taking off experiences hypergravity conditions. The behaviour of bubbly flows in such conditions needs to be understood well in order to be able to improve the efficiency of the devices containing them. Additionally, it is desirable in certain systems to manage the dynamics of bubbles. The interaction between acoustic waves

and bubbles has been proved to be an efficient method for controlling bubble dynamics (Leighton (1994); Abe et al. (2002); Fan & Cui (2005)). However, the effects of acoustic fields on bubble generation and dynamics have some issues that require further experimentation.

Three main processes have to be considered when a bubble is injected into a liquid in the direction opposite to gravity: detachment, rise and coalescence with a free surface. When a bubble is injected into the liquid through a needle, the shape and size of the bubble is determined by the balance of forces acting on it during the process (Fan & Cui (2005)). In particular, gravity plays a crucial role in this process. This effect was observed by Suñol et al. (2011), where the diameter of the injected bubble was found to be strongly dependent on the gravity level. Once the bubble has been injected, it will reach a constant rise terminal velocity at the moment when the drag force compensates the buoyancy effect. The last main process consists of the bubble bouncing before it finally coalesces with the free surface.

The effects of an acoustic standing wave on bubbly flows have been studied in normal gravity by focusing on the shape and size of the bubbles (Fan & Cui (2005); Xi et al. (2011)) and on the motion of the bubbles when applying a phase shift (Abe et al. (2002)). The latter work also presents results in microgravity conditions, showing that the position of the bubble in the standing wave varies due to the absence of the buoyancy effect.

When acoustic forces are applied to injected bubbles, the processes of bubble detachment and rise behave differently than without acoustics. It is known that applying an acoustic standing wave to the gravity axis generates bubbles of smaller initial size that maintain a more spherical shape during the process (Fan & Cui (2005)).

To our knowledge, studies that apply standing waves in a perpendicular direction to the bubble motion have mainly focused on the effects of Bjerknes forces (Crum (1975); Rabaud et al. (2011)) or on different characteristics of sonoluminescence (Posakony et al. (2006); Urteaga & Bonetto (2008); Yanagita et al. (2002)). Thus, by studying the perpendicular application of an acoustic field to the path of a rising bubble, new knowledge could be provided on the dynamics of rising bubbles. It is interesting to observe how the effects of a transversal field differ from those of an axial field (with respect to the axis of gravity) in the process of bubble detachment, since the dynamics of the bubbles should be different for each case. Therefore, affecting different parameters.

We present the results from an experiment for studying the size and shape of bubbles injected into a tank of liquid, as well as the dynamics of the bubbles rising in the tank under a standing acoustic wave at different gravity levels higher than $1g_0$. This experiment was carried out in the framework of the "Spin Your Thesis! 2012" programme at the Large Diameter Centrifuge (LDC) in ESTEC (Noordwijk, The Netherlands).

Two acoustic waves were considered. One of them was applied in the direction

of gravity (axial or vertical field) and the other one perpendicular to it (transverse or horizontal field). Different tests were carried out by applying one or the other of the acoustic fields. We observed the size and shape evolution of the injected bubbles in distilled water.

Moreover, the results from the experimental campaign were complemented with theoretical analysis and numerical simulations.

5.2 Experimental Setup

The experimental setup (Figure 5.1) consisted of the following systems: test cell, bubble injection, acoustic wave generation, and data acquisition. The dimensions of the test cell were 100 mm × 100 mm × 100 mm, and it was filled with distilled water. Two piezoceramic transducers (PZT) were attached to the cell walls, one on the lateral wall and one underneath. Two sides of the test cell were free of devices so that the whole process could be recorded from one side and illuminated from the other.

We released air bubbles with an equivalent diameter (d_e, bubble diameter after detachment) of between approximately 0.7 to 2 mm. The nozzle was placed at the bottom wall of the test cell, allowing the bubble to rise as a result of the action of gravity. Gas was injected into the cell at the desired flow rates by means of a syringe pump. The test cell had a gas outlet at the top to avoid any overpressure in the system.

The acoustic sound field was generated by the PZTs by means of a function generator that was fixed at given frequencies and amplitudes. The output of the function generator went through a voltage amplifier.

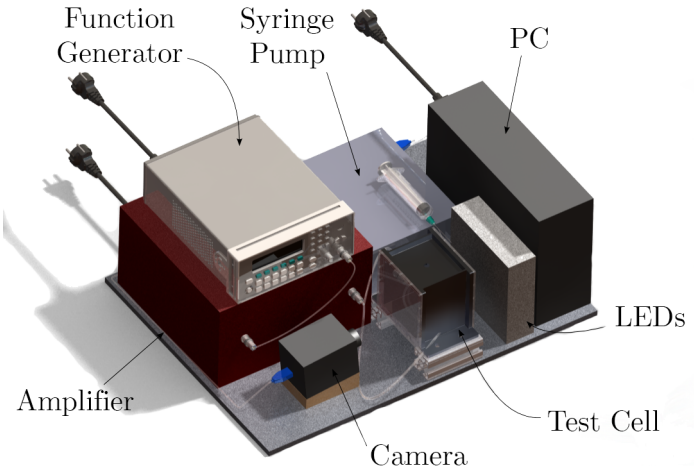

Figure 5.1: Diagram of the experimental setup including all the required equipment.

The initial setup distribution is shown in Figure 5.1, which shows the location of all the devices on the base plate, including the wires. In order to ensure the test cell could sense with precision the actual gravity level applied, the equipment was ultimately placed somewhat differently from what was expected, so that the cell would be at the middle of the gondola. A more detailed description of each subsystem can be seen in the following subsections.

5.2.1 Bubble Injection

By means of the bubble injection system, we were able to inject bubbles into the test cell using small quantities of gas. This system consisted of:

- *Syringe Pump.* A KDS Legato 180 allowed the control of the gas flow rate, and it was controlled by means of LabView from a computer at the operation bench.
- *Syringe.* A syringe with the desired amount of gas was placed in the syringe pump. We chose a 20 ml syringe to be used during the tests. A needle was placed at the tip of the syringe. A 1 mm outer diameter tube was connected to the needle through a retractable joint.
- *Needle/Injector.* The same retractable joint was used to connect the gas line to the injector. The gas line was connected to a stainless steel needle that finally injected the gas into the test cell. The needle had an internal diameter of 0.15 mm and an external diameter of 0.72 mm.
- *Gas Outlet.* During the design phase of the test cell, we took into account a gas outlet. This outlet was placed on the upper wall in order to avoid any overpressure inside the test cell.

5.2.2 Acoustic Wave Generation

By generating a specific electrical signal, we were able to have a standing acoustic wave inside the test cell. The following devices constituted this system:

- *Function Generator.* Through this device (Agilent 33210A 10 MHz Function / Arbitrary Waveform Generator), we were able to precisely control the frequency and voltage amplitude of the sine wave. Live control of this device was performed with LabView.
- *Amplifier.* The function generator produced a very low output voltage amplitude, which led to very low acoustic energy inside the test cell. In order to obtain higher amplitude, a 50× voltage amplifier (Falco WMA-300) was used. This amplifier can provide up to 300 V_{p-p}.

- *Piezoelectric Ceramic Transducers (PZTs).* The output from the amplifier was directly connected to two piezoelectric transducers that converted the electrical signal into mechanical vibrations. Coaxial cables were used to connect this system. Each transducer works better at specific frequencies provided by the manufacturer; i.e. 53 kHz for the transverse field and 60 kHz for the axial field.

5.2.3 Data Acquisition

High-speed videos were recorded, in order to obtain data from the phenomena taking place inside the test cell. To this end, the following devices were used:

- *LEDs Matrix.* A matrix of 12 × 12 ultra-bright LEDs (10000 mcd each) illuminated the test cell from one side. A diffuser sheet was used in order to provide homogeneous background illumination. LEDs reduce the possibility of abrupt temperature changes in the system due to lighting.
- *High-Speed Camera.* On the opposite side of the LEDs, a high-speed camera (RedLake Motion Xtra HG-SE) with a frame rate of 1000 fps, and an image resolution of 1280×256 pixels per frame.
- *PC.* Once videos had been recorded, they were saved in the camera's buffer. Thus, a PC was used to transfer the video and record the next one. A fanless PC with solid state drives was used, since it did not have any moving parts. Moving parts can damage the device at high gravity levels.

5.2.4 Test Cell

SolidWorks was used to design a test cell specifically for the Spin Your Thesis! campaign. The test cell was a 93 mm × 93 mm × 93 mm (inner size) aluminium cube, with two 119 mm × 119 mm methacrylate windows. It was filled with distilled water up to a level of 62 mm. The final experimental setup mounted inside the gondola can be seen in Figure 5.2.

5.3 Experimental Procedure

Different parameters were controlled in the experiment and were kept either constant or varied during the tests. A single output was obtained: the high-speed videos of the rising bubbles. The controlled parameters of the experiment were separated into two groups: constants (frequency and properties of the fluid, i.e. distilled water) and variables (voltage amplitude, direction of the sound field and gravity level).

Even though we initially planned on keeping the voltage amplitude constant, at the end we decided to vary it and keep the properties of the fluid constant (distilled water). Ground tests were carried out before the campaign in order to determine

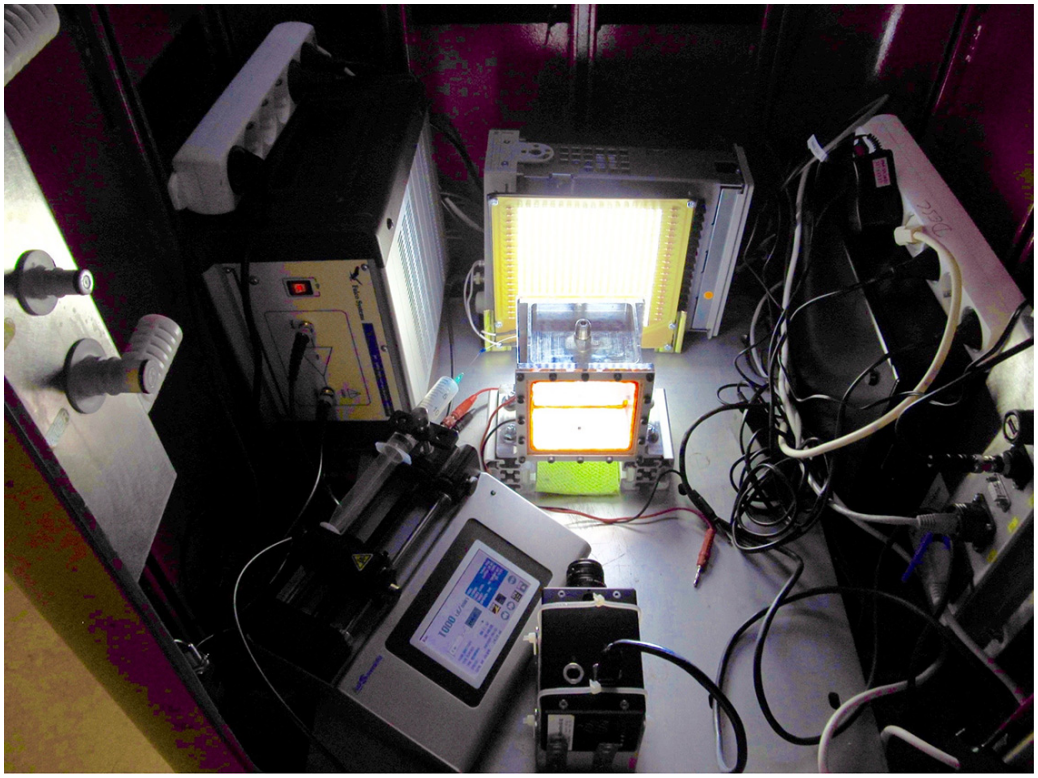

Figure 5.2: Experimental setup assembled inside the gondola of the Large Diameter Centrifuge.

the optimal frequencies and voltages to be used. These tests were carried out using different test cells, since the final test cell for the campaign was delivered later.

As results were desired for the performance of different frequencies in distilled water at each gravity level, we fixed the frequency for each field direction (thus, 2 frequencies per gravity level) and kept them constant during the campaign. We also tested different voltage amplitudes (which caused different effects on the bubbles) for each field direction and at each gravity level. If we had had spare runs, we would have liked to have changed frequencies and/or liquids during the tests, so that we could actively control the bubble motion and compare the effects of acoustic fields on different media.

Table 5.1 shows the main tests that were carried out and the variables that were considered in each test. Each gravity level was explored for approximately 1 min. No special requirements for transitions between different gravity values were needed other than allowing the free surface to stabilise after each change, which took less than a minute.

Table 5.2 shows the campaign schedule that was followed, taking into account

Test	Field Direction	Fluid	Gravity Level (g_0)	Voltage (V)
1	Transverse (53 kHz)	Distilled Water	1, 2, 5, 10, 15, 20	3, 4, 5, 6
2	Axial (60 kHz)			

Table 5.1: Summary of the main tests carried out and parameters that were controlled during each test (frequency was kept constant).

the planned tests and the 2.5 days available for LDC experimentation. It took place early in the week from 10 to 13 September 2012, at ESA-ESTEC in Noordwijk, The Netherlands.

Day	Morning (9h to 13h)	Afternoon (14h to 18h)
Monday	-	Assembly of the experiment
Tuesday	Test 1	Test 1
Wednesday	Test 2	Test 2
Thursday	Backup tests: Tests 1 and 2 recording closer to the nozzle	Unloading the experiment and packing

Table 5.2: Campaign schedule for the week at the LDC.

Backup (i.e. additional) tests were carried out using a different lens on the camera in order to try to capture the motion of the bubble right at the tip of the nozzle with a higher resolution.

The original date of the campaign was moved to 10-13 September 2012 due to repairs being carried out at the LDC. During these repairs, we assembled the experiment on Monday, 10 September 2012. We began testing on Tuesday morning. Experiments were performed from Tuesday morning until Thursday morning, when backup tests were carried out. The experimental setup was dismantled on Thursday afternoon and left ready for shipping back to our laboratory.

The procedure for recording and saving the high-speed videos was the following (taking into account that the LEDs, function generator and amplifier had already been activated and the gravity level had already been stabilised):

1. Start gas injection with the syringe pump and let it run until a steady flow of bubbles is achieved (30 s $\sim$ 1 min).
2. Start high-speed video. A signal triggers the camera and records the injection and rising of the bubbles ($\sim$ 4 s).
3. Transfer high-speed video to the computer. This step was by far the longest, and it took place while the LDC was still running (15 $\sim$ 20 min).

The above procedure was monitored from the operation bench and took approximately 15 to 20 min. Transferring the video from the camera buffer to the computer

was the step that took the longest time to complete.

5.4 Experiment Results

The data generated during the campaign amounted to 77 high-speed videos, which correspond to a total amount of approximately 210000 frames. The initial processing of the videos took a long time because the videos were quite large. We first carried out a qualitative analysis (Section 5.4.1) of all the phenomena observed in the videos so that we could later focus on certain key aspects for a more detailed analysis.

Videos were converted (by means of AviSynth) to an uncompressed AVI file, which is the format that is compatible with the Fiji (ImageJ) software that was used for the analysis. Upon conversion, videos became very heavy in terms of computer memory (2 - 4 GB each, compared to the initial 3 MB). Hence, each video was cropped, keeping only the area of interest (a field of view that allowed observation of all the rising bubble paths), and also converted to grayscale. These steps were necessary in order to avoid long computing times during certain stages of the analysis.

5.4.1 Qualitative Analysis

First, a table summarising all the cases studied (Figure 5.3) is presented, organised by gravity level, field direction and applied voltage. A single image from each of the videos has been generated by overlapping the pixels of minimum intensity for all the frames.

From Figure 5.3 and observation of the videos, some common features in different cases can be distinguished. The observed effects are listed below and will be individually explained later on, including pictures from the videos for better understanding.

1. Direction
   (a) Injection (initial)
   (b) Rise (final)
2. Injection and bubble size
   (a) Uneven
   (b) Uniform
3. Oscillatory rising trajectories
4. Bubble levitation
5. Bubble-bubble interaction (Secondary Bjerknes Force)
6. Deviation
7. Cavitation

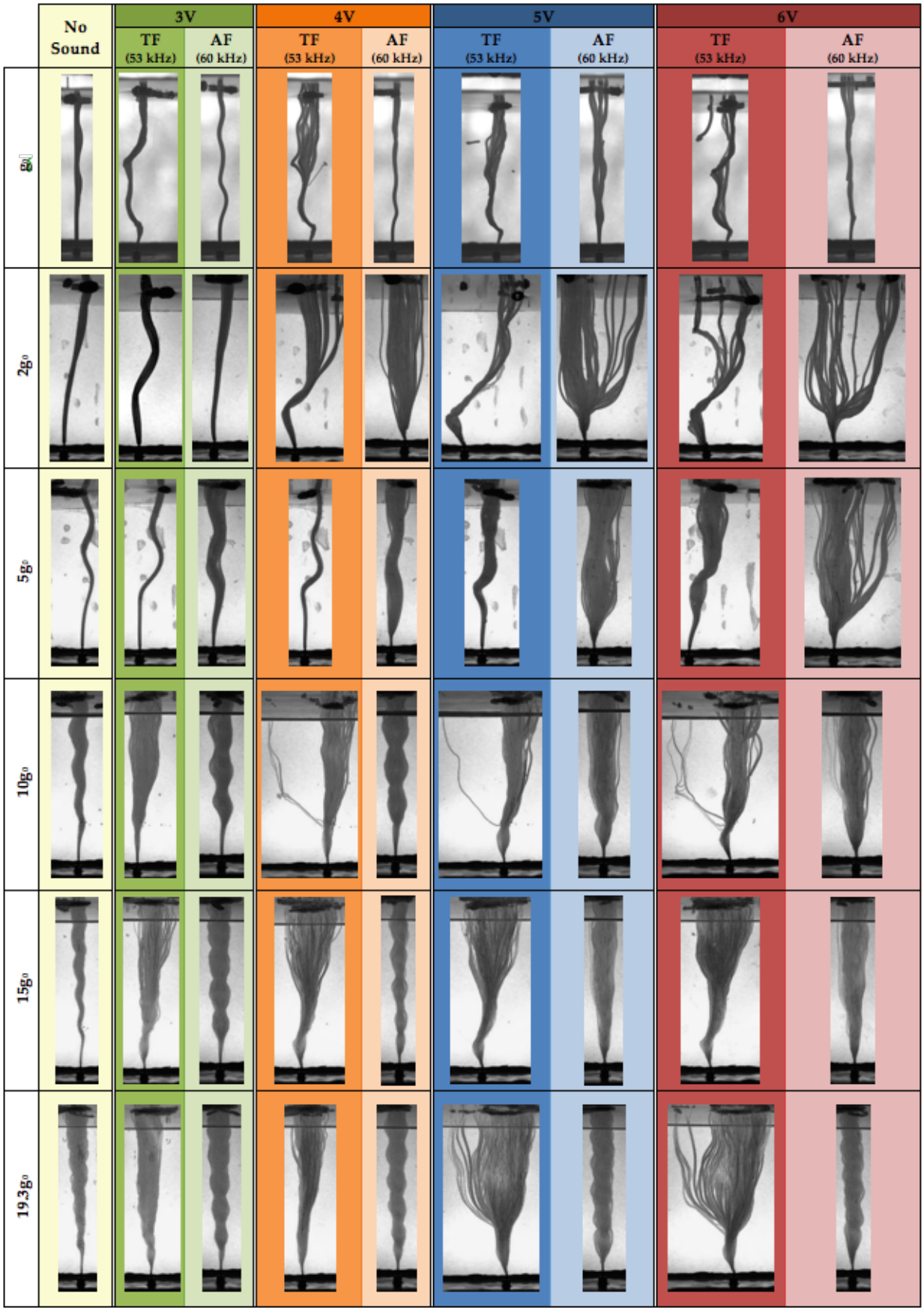

Figure 5.3: Summary of the explored g-levels. Images obtained by overlapping most frames of each video.

Direction

It was observed that bubbles start deviating to the left or to the right just after detachment (initial direction). After some milliseconds (just before colliding with the free surface), bubbles move to the left or to the right with respect to the injection axis (final direction). To distinguish both measurements, we have defined the criteria shown in Figure 5.4. The nozzle injection axis has been taken as a reference in the z direction. The initial direction is considered by observing the behaviour of the bubbles during the first 7 mm of rise. The final direction is considered to be the position of the bubbles when crossing the yellow arrow (close to the free surface).

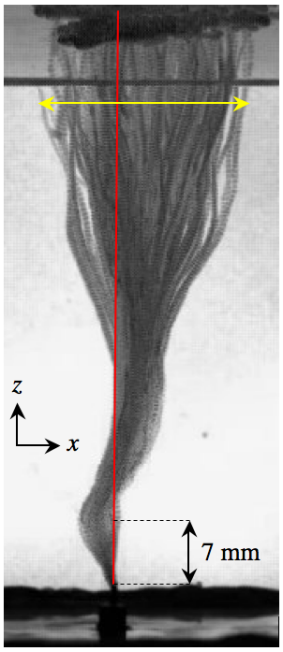

Figure 5.4: Sum of the pixels of minimum intensity during 1 s to show the criteria for these measurements.

Regarding the initial direction, we observed four different behaviours: left, straight, right and downwards. The most common of the four cases was the straight initial direction, especially when applying the axial acoustic field.

Downwards injection (Figure 5.5) was only observed when applying the transverse field at $2g_0$ and high voltages (5 and 6 V). Figure 5.5 shows the image sequence of downward injection at 6 V. Since we were recording the whole rising process from the nozzle to the free surface, the image resolution was not high enough to allow good visualisation of the detachment of such small bubbles. Downwards injection is easily observed in the videos, but not so obvious when shown on still images. In any case, it can be observed in Figure 5.5 that very small bubbles (red circles) detach

from the nozzle tip and, instead of rising up, they go down to the base of the needle and coalesce there (yellow arrow), until the bubble reaches a critical size (most likely due to overcoming the surface tension force), and it detaches from the base of the needle. The bubble diameter upon detachment from the base is approximately 1.5 mm.

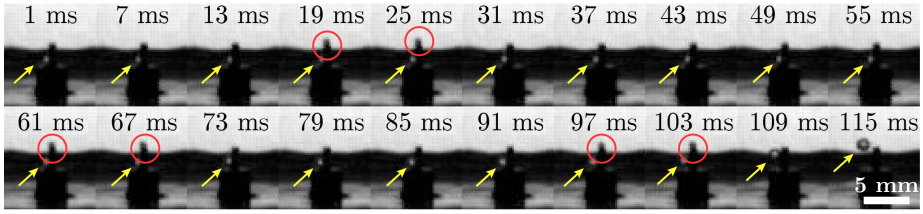

Figure 5.5: Image sequence of downwards injection ($2g_0$ transverse 6 V). Red circles show the frames where bubbles are seen growing on the nozzle tip and going downwards.

Regarding the final direction, it can be seen in Figure 5.3 that each case is quite different from the other. They can be classified into three categories: straight, right and widespread. The most common of the three is widespread, although not all of them have the same tendency. Some are widespread centred, while others are widespread to the right (compared to the axis of the nozzle). Most of the cases appear to rise towards the right, which could be due to the Coriolis effect.

Two of the analysed cases are shown in Figure 5.6, superposing the expected acoustic wave in each case. Figure 5.6a shows one of the cases where levitation occurred. It is observed that bubbles initially moved towards the expected pressure antinode and, immediately afterwards, they deviate to the right. Approximately halfway to the free surface, we observe three cases. In the first case, bubbles that are apparently smaller than the resonance size go back to the leftmost antinode and levitate. The second case occurred with only one of the bubbles, which remained approximately at the pressure antinode and rose to the free surface without deviating. Finally, the third and most common case presents bubbles moving to the pressure node and reaching the free surface at the same node position. From this behaviour, it can be deduced that bubbles are larger than the resonance size, and thus they go to the pressure node.

When applying the axial acoustic field (Figure 5.6b), most of the bubbles rise in an oscillating motion around the axis of the nozzle.

Injection and Bubble Size

Uneven detachment or injection of bubbles was also observed in the recorded videos. When bubbles are injected without applying an acoustic field, single bubbles detach regularly from the nozzle (similar to Figure 5.7b). However, when an acoustic field is present, the behaviour of the bubbles upon injection becomes less predictable.

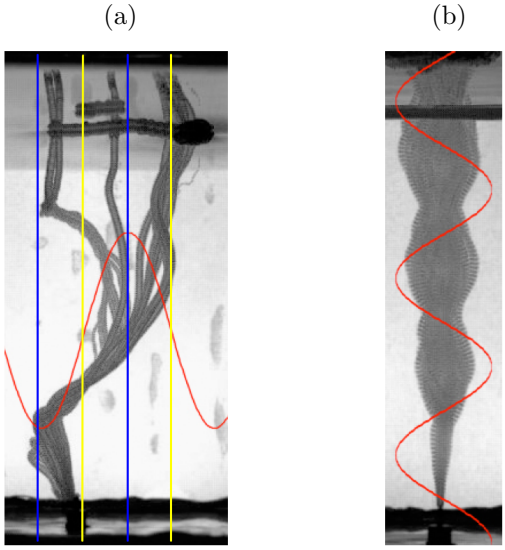

Figure 5.6: (a) $2g_0$ transverse 6 V and overlaid in red 53 kHz wave, blue lines show antinodes and yellow lines show nodes. (b) $10g_0$ axial 4 V and overlaid in red 60 kHz wave.

For instance, in Figure 5.5 we can already observe uneven injection. Tiny bubbles appear from the nozzle (although they cannot be observed in that sequence) while, during that test, two slightly larger bubbles are also injected simultaneously.

This effect is clearly noticeable in Figure 5.7a, where bubble injection is observed for 37 ms. From $t = 17$ ms, it can be observed that the bubble that was injected was actually two bubbles. This also occurred with groups of three bubbles injected. In all of the cases, the number of bubbles is known because they attract and repel each other as they rise.

As in the case when no acoustic field is applied, a uniform size of injected bubbles is observed only at low voltages (3 V or 4 V) and when applying the transverse field at $5g_0$. The $5g_0$ case is easily observed in Figure 5.3, where all the bubbles follow the same path during the experiments, thus allowing for those well-defined trajectories obtained in the overlapped images.

Oscillatory Rising Trajectories

In the tests without an acoustic field applied, it was observed that the frequency of the oscillatory rising paths of the bubbles increased as the gravity level increased, and its wavelength decreased as the gravity level increased. This behaviour is shown in Figure 5.8, where the average wavelength of 3 bubble trajectories at each gravity level are plotted against g/g_0. The wavelength was measured from the first minimum to the next. At $2g_0$, it is not possible to observe a full wavelength, hence the wavelength has not been determined.

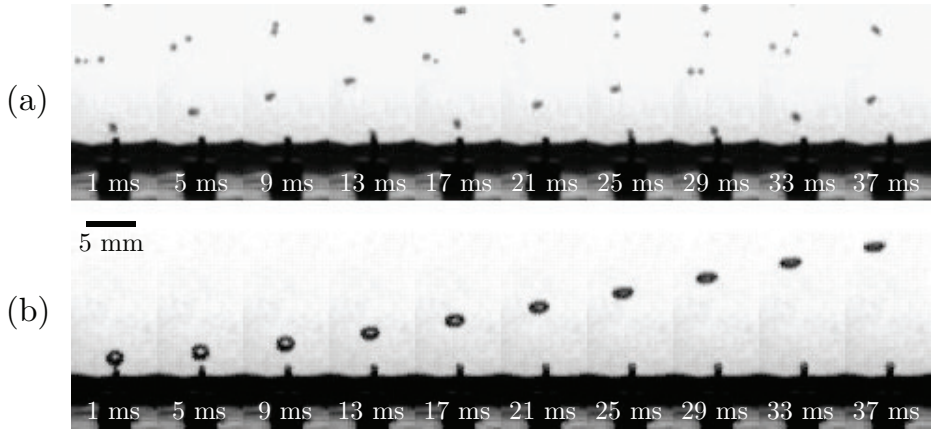

Figure 5.7: (a) Image sequence of uneven injection ($10g_0$ transverse 6 V). (b) Image sequence of uniform injection ($2g_0$ transverse 3 V).

In the cases with an acoustic field, one can observe that at high voltages (5 and 6 V) the rising trajectory is oscillatory only for certain bubbles, hence the overlay of all the trajectories is not a uniformly oscillatory path. Oscillatory rise is observed especially when applying the axial acoustic field at 3 and 4 V, and also at $2g_0$ and 3 V.

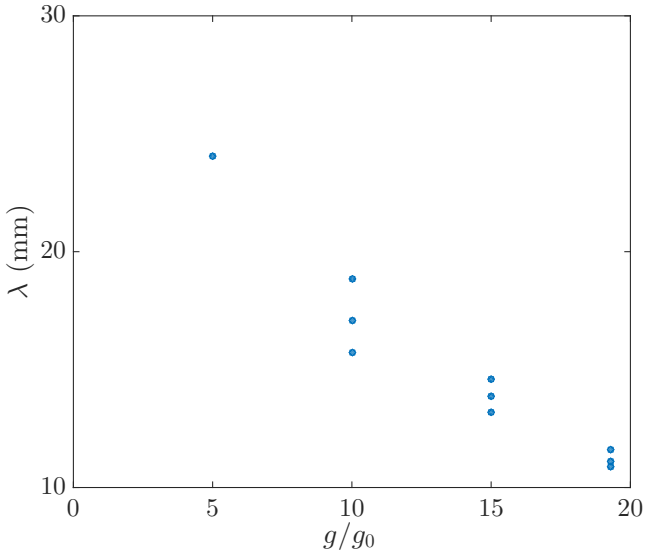

Figure 5.8: Average wavelength of 3 bubble trajectories at each gravity level, without an acoustic field. At $5g_0$, all bubbles have the same wavelength while rising.

Cases where the shape of the overlaid paths of the bubbles are similar to that

of a sinusoidal wave, are shown in Figure 5.9. Both the cases, with and without an acoustic field, are presented. All of the cases with an acoustic field occur when applying 3 or 4 V. The bubble trajectories in each case have approximately the same wavelength. The acoustic field causes the bubble paths to have different amplitudes and phases.

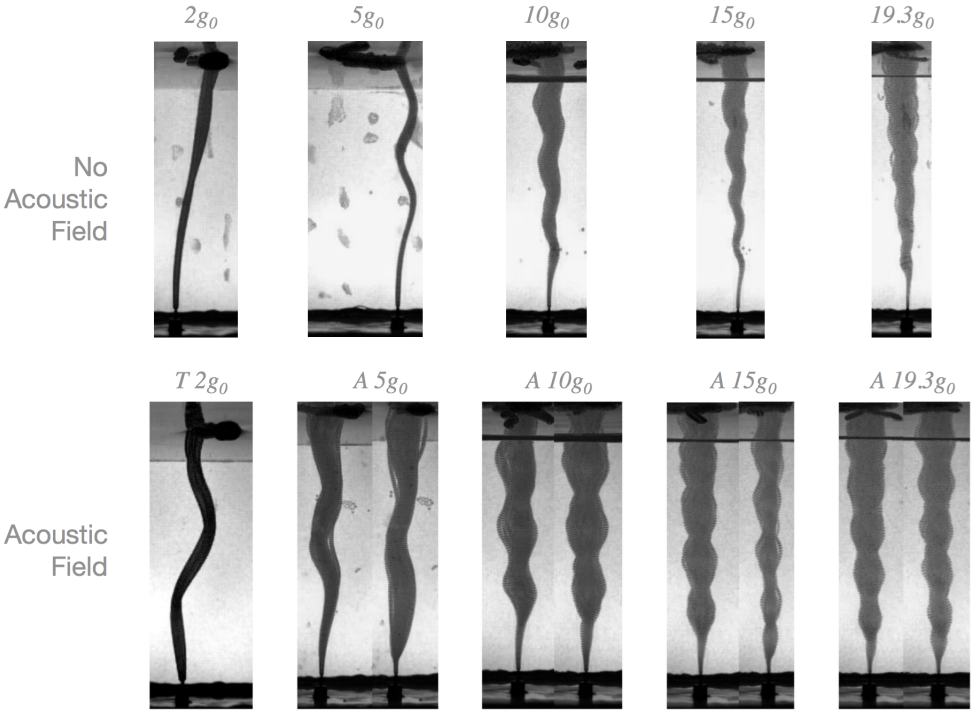

Figure 5.9: Overlaid trajectories in the cases where oscillatory rise is observed. Upper row without acoustic field, lower row with acoustic field (from left to right: transverse field at $2g_0$ and 3 V and axial field at $5g_0$, $10g_0$, $15g_0$, $19.3g_0$, respectively).

Bubble Levitation

Levitating bubbles remain at the same position for several milliseconds, delaying the time to reach the free surface as compared to the other bubbles that appear during the same time frame in the video. Figure 5.10 shows the case where levitation is observed more clearly. This is only observed it at $2g_0$, and very lightly at $10g_0$, meaning that the trapped bubbles are small compared to the rising bubbles, and that the time they are trapped is shorter.

Figure 5.10 shows one of the observed cases of levitation. Circled in red, we observe the levitating bubble, which coalesces with two other bubbles during the 800 ms that it is levitating. The two observed rising paths on the right take about

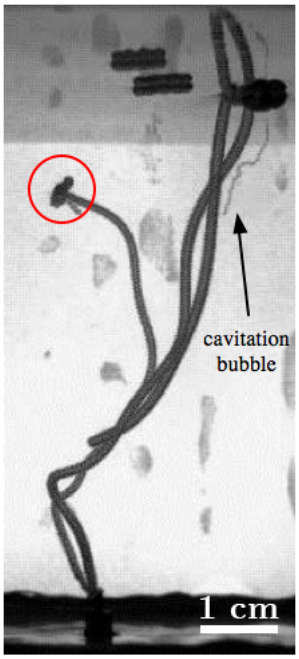

Figure 5.10: Sum of the pixels of minimum intensity in 800 frames. Horizontal field, $2g_0$ and applying 6 V. Total time of the process is 800 ms. The red circle shows the levitating bubble.

340 ms from the moment they detach from the needle until they reach the free surface.

Without applying the transverse acoustic field, a bubble at $2g_0$ takes approximately 254 ms to reach the free surface. Hence, the levitating bubble stays in the levitation position four times longer than an untrapped bubble rising in the same acoustic field, and five times longer than a bubble rising at $2g_0$ without applying an acoustic field.

When applying the axial acoustic field, we also observed bubbles levitating even though the time was shorter. In that case, however, bubbles were usually trapped closer to the injection point.

Bubble-Bubble Interaction (SBF)

Strong interactions among two or more bubbles were observed in 24 (12 in each field direction) of the 40 cases presented in Figure 5.3 (considering only those where acoustic fields were applied). Most of these interactions were observed when applying 5 or 6 V. Typically, they were identified because bubbles attracted and repelled each other along the rising trajectory; sometimes it involved just two bubbles, but multiple

bubble interaction was also observed.

Figure 5.11 and Figure 5.12 show montages of two cases: the first one occurs while applying the transverse field and the second one for the axial field. The interaction occurs slightly differently in both cases; thus, different methods have been used to better illustrate the phenomenon.

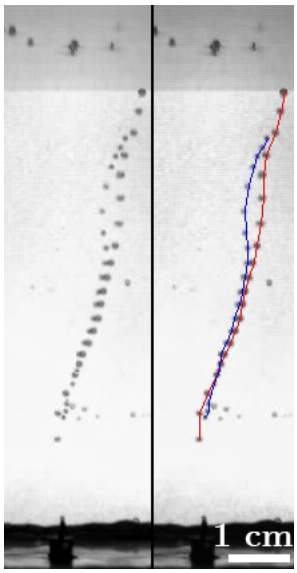

Figure 5.11: Left: Overlay of frames at every 21 ms. $10g_0$ transverse field 53 kHz 4 V. Right: same with bubble paths.

Figure 5.11 shows the first of the montages. Two particles are observed in this case. Initially, the smaller particle (blue trajectory) is levitating at a certain height for 20 ms (not shown in this montage). As the slightly bigger (red) particle approaches, the blue one moves slightly to the right. The red particle overtakes the blue one, which then starts following the red one. Right after this occurs, these two particles join (not coalesce) and rise higher for a while. Finally, the red particle separates and starts a faster rising trajectory until it reaches the free surface. Even though shape oscillations cannot be observed due to the resolution, they might be occurring and leading to the secondary forces.

In Figure 5.12 we can observe an interaction between three bubbles. Initially, two bubbles stuck together rise up from the needle. At a given point, one of the bubbles in the pair detaches from the other, which stays in that position for some time (18 ms approximately), until the next injected bubble gets closer. As the third bubble approaches, it first collides with the second one, joins it, and for approximately 16 ms they start rising together. Finally, these bubbles separate from each other and rise to the free surface. During the rise, these two bubbles are seen attracting and repelling each other.

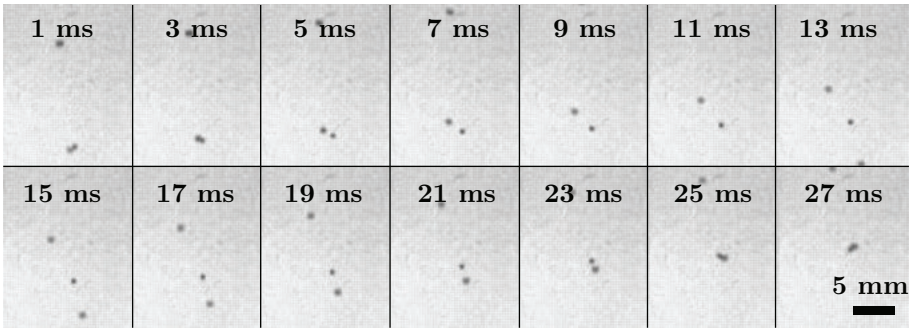

Figure 5.12: Time sequence of one of the interactions during this case ($15g_0$ axial field, 60 kHz 5 V).

Deviation and Cavitation

It was observed in some of the videos that certain bubbles deviate largely from the mean trajectory of the rest of the bubbles. This is determined by two factors: the initial stretch of the rising path; and the size of the bubbles (typically due to uneven injection). Moreover, in the 6 V transverse test at $10g_0$, the cause of this effect was both uneven injection and generation of tiny bubbles due to acoustic cavitation.

Figure 5.13 shows one of the cases in which highly deviated bubbles were observed. Cavitating bubbles (smaller than 500 μm) appear in this video. Due to the backlight, the small sizes and the high velocities at which they move, it is only possible to observe them in certain zones of the video (red circles).

5.4.2 Pressure Measurements

Before getting into more detail on the quantitative analysis, we should mention a series of measurements with a hydrophone that were carried out in order to know how the axial pressure wave propagates. For this scenario, we have focused on the axial field, since it presents the most reproducible results.

In order to get a better understanding of the dynamics behind the bubble detachment and rise when applying an acoustic field, the acoustic pressure inside should be coupled with the rise trajectories.

An automatised setup was prepared for taking these measurements. First, extra orifices at the top of the cell had to be added in order to properly fit the hydrophone. The reason for this is that the hydrophone provides better measurements of the field when it is perpendicular or at a certain angle to the direction of the field propagation. Due to physical constraints, the largest possible angle that could be obtained between the field and the hydrophone was 50.75°. Moreover, the hydrophone was attached to a rod that was moved by an adapted syringe pump, which was used as a stepper motor. The data was acquired by means of LabView. The final pressure value was

Figure 5.13: Transverse field 6 V under $10g_0$. Overlapped trajectories during 409 ms. Arrow shows the deviated trajectories. Red circles show cavitation bubbles.

obtained after setting the appropriate sensitivity for each frequency, as provided by the manufacturer's calibration sheet.

With the setup explained above, and measuring from the bottom of the cell up to the free surface, the pressure profiles shown in Figure 5.14 were obtained. These measurements were taken in the lab a few months after the hypergravity experiments.

5.4.3 Bubble Detachment

Here we present results obtained from the study of the bubbles' detachment, both when there is no acoustic field (which is in line with previous work by Suñol & González-Cinca (2015)) and when an acoustic field is applied.

Using the recorded images, the major diameter d_h and minor diameter d_v were measured just as the bubble detaches from the nozzle. The equivalent diameter (d_e) is obtained from the measured diameters as

$$d_e = (d_h^2 d_v)^{\frac{1}{3}}, \tag{5.1}$$

which corresponds to the diameter of a spherical bubble with the same volume as

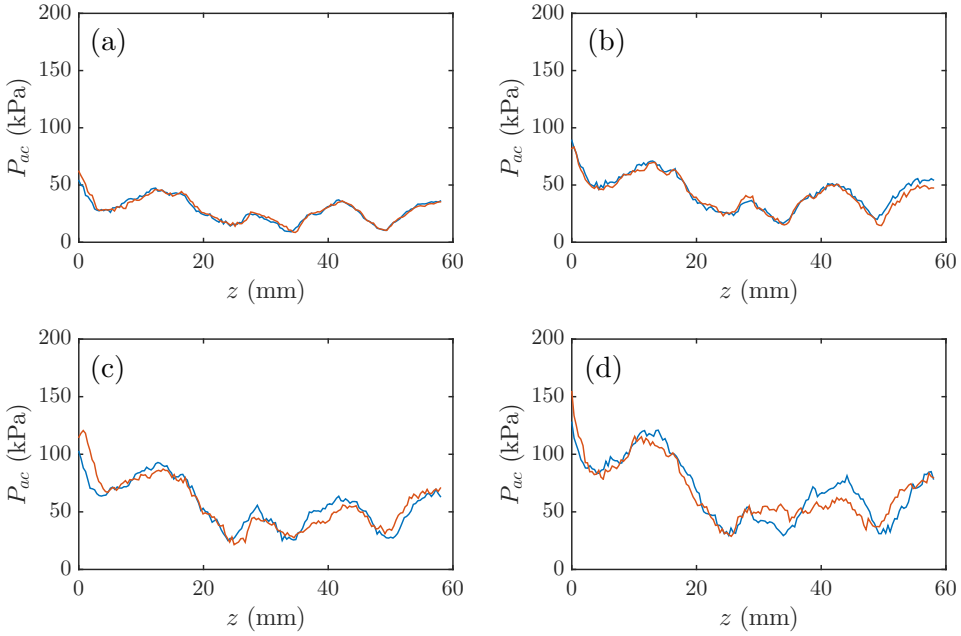

Figure 5.14: Measured pressure at each of the voltages applied during the campaign. (a) 3 V, (b) 4 V, (c) 5 V and (d) 6 V.

the actual oblate spheroid observed experimentally. This approximation was used to obtain the equivalent diameter in all the cases, with and without an acoustic field.

The bubble's diameter upon detachment, when there is no acoustic field, can be determined by a competition between buoyancy force, $F_{By} = \rho_l g V$, and the surface tension force, $F_\sigma = \pi d_C \sigma$, which are the only forces acting at the nozzle tip (provided that inertial forces are neglected). Thus, when $F_{By} = F_\sigma$, the bubble will reach its critical diameter and will detach, obtaining the gravity dependent detachment diameter

$$d_e = \left(\frac{6\sigma d_C}{\rho_l g} \right)^{(1/3)}, \tag{5.2}$$

where $d_C = 0.15$ mm is the inner diameter of the nozzle. In Figure 5.15, the theoretical prediction in equation 5.2 and the obtained experimental values are plotted. Good agreement between theory and experiments is obtained.

For the case when an acoustic field is applied, the theoretical relationship is not valid anymore and needs further consideration. As will be shown later on, the diameters when the field is present are lower in the experimental measurements. This was expected, since the acoustic force acts in favour of the buoyancy force. For

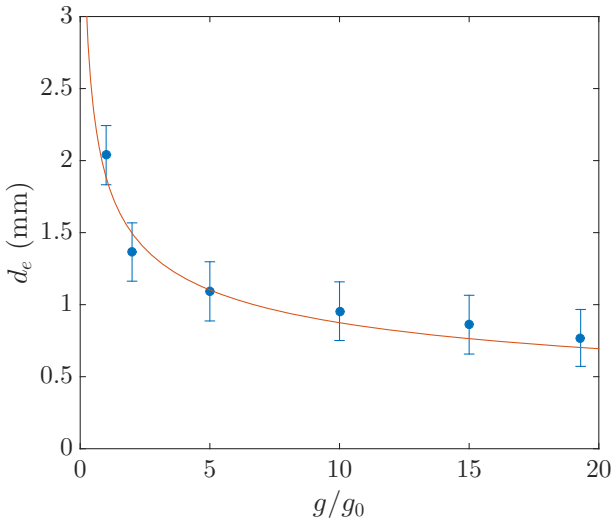

Figure 5.15: Detachment diameter as a function of the gravity level. Points: experimental case without acoustic field. Line: analytical expression of d_e (equation 5.2).

higher voltage amplitudes (5 - 6 V), however, it is not possible to directly measure the diameters, since the video's resolution is not good enough to measure such small bubbles.

With the measurements presented in Section 5.4.2, the pressure values close to the nozzle tip can already be considered. For 3 V, they correspond to 30 kPa. As mentioned above, the acoustic force acts against the surface tension (or capillary force) on the nozzle, which favours the buoyancy force, i.e. $F_{By} + F_{Bj} = F_\sigma$, neglecting any inertial effect (Figure 5.16a).

First, we need to know whether we are dealing with bubbles larger or smaller than their resonance size. As explained in Chapter 1, bubbles larger than resonant size will locate themselves at the antinodes of the wave. To establish their relative size, we use Minnaert's resonance frequency equation, as shown in Chapter 1

$$\omega_0 = \frac{1}{R_0}\sqrt{\frac{3\gamma p_0}{\rho_l}}, \tag{5.3}$$

where ω_0 and R_0 are the resonance frequency and radius, respectively; γ is the polytropic index for adiabatic conditions (for air $\gamma = 1.4$) and p_0 is the hydrostatic liquid pressure outside the bubble. From equation 5.3, the obtained corresponding resonant size for $f_0 = 60$ kHz is $d_0 = 0.11$ mm. Thus, it can be confirmed that the range of bubble sizes considered in this study are larger than resonance ($R > R_0$).

We consider the Bjerknes force equation derived by Leighton (1994) (equation 1.7), which is written below for convenience.

$$F_{Bj} = -\frac{4P_{ac}^2 k\pi R_0 \sin(2ky)}{\rho_l} \frac{1}{\omega_0^2 - \omega^2}. \tag{5.4}$$

This equation is only applicable in the range of bubbles that are larger than resonance. When adding the Bjerknes force to the force balance in order to obtain the detachment diameter when applying the axial field, one gets

$$\rho_l g \frac{4}{3}\pi R^2 - \frac{4P_{ac}^2 k\pi R}{\rho_l} \frac{1}{\frac{1}{R^2}\frac{3\gamma p_0}{\rho_l} - \omega^2} = \pi d_C \sigma. \tag{5.5}$$

This equation must be solved numerically. We removed $\sin(2ky)$ (equation 5.4), since the pressure that will be considered is already the value for a certain point of the wave, not the amplitude of the wave. By reworking equation 5.5, the resulting fifth order equation is reached, which can be used to obtain the detachment diameter of bubbles at different gravity levels and for a certain pressure field. It has the structure $AR^5 + BR^3 + CR^2 + D = 0$, where the coefficients A, B, C and D are

$$A = \frac{4}{3}\pi g \rho_l^2 \omega^2, \tag{5.6}$$

$$B = \frac{4\pi\omega P_{ac}^2}{c} - 4\pi\rho_l g \gamma p_0, \tag{5.7}$$

$$C = -\pi d_C \sigma \rho \omega^2, \tag{5.8}$$

$$D = 3\pi d_C \sigma \gamma p_0. \tag{5.9}$$

Equations 5.6 to 5.9 are solved in order to obtain the detachment diameter of the bubbles at different gravity levels. For the acoustic pressure values measured from the 3 V case, the numerical solution is plotted in Figure 5.16b.

Comparing the numerical results to the experimental results for the case of the acoustic field, it can be observed that at 3 V (measured acoustic pressure 30 kPa) the numerical results are in good agreement with the experimental measurements of the diameters. However, it should be noted that for higher gravity levels ($>10g_0$), the effects of the acoustic field on the bubble size seem almost negligible.

Note that the results for 4, 5 and 6 V are not shown in Figure 5.16b. From 4 V (about 50 kPa) on up, bubbles injected from the nozzle are very small and the video resolution is not good enough to measure their size. The observed behaviour shows that bubbles are injected at very small sizes, and they remain attached to the nozzle. They sometimes coalesce or simply agglomerate, until they reach a critical size (close or slightly smaller than the one measured at 3 V) before detaching from the nozzle.

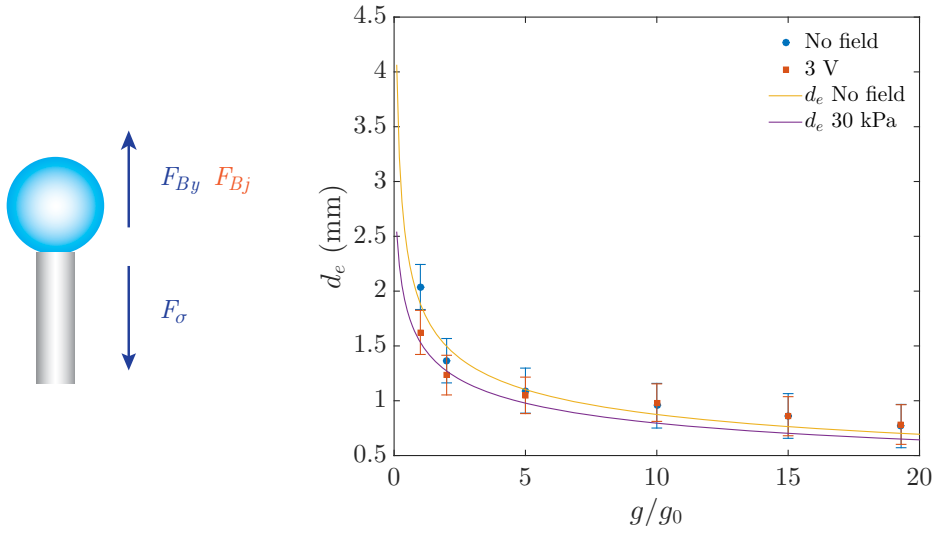

Figure 5.16: (a) Diagram of forces acting on bubble detachment. Dark blue indicates forces acting when there is no acoustic field and no inertial forces. (b) Detachment diameters for the experimental 3 V cases, analytical results for no acoustic field and numerical results for acoustic field. Error due to video resolution and standard deviation of the measurements.

5.4.4 Oscillatory Rising Trajectories

In all the tests, the distance between the tip of the needle and the free surface was kept between 62 and 70 mm, depending on the case. This allowed us to obtain a longer rise trajectory than Suñol & González-Cinca (2015). A sinusoidal curve was fit to the paths, and the wavelength of the path was obtained from there, which has already been shown in Figure 5.8. Figure 5.17 shows the fitted curve on the experimental bubble trajectory for a $5g_0$ case. In our test cases, we observed periodic oscillatory trajectories only when: no acoustic field was applied, the vertical field was applied at low pressure (i.e. 3 V) and in the $2g_0$ while applying 3 V case with the horizontal field.

In the case without the acoustic field, we can observe in the overlapped frames shown in Figure 5.9 that bubbles rise to the free surface following an oscillating (or zig-zag) path. Furthermore, it appears that, as the gravity level increases, the frequency of the zig-zag path increases. In all of the cases, it can be seen that the injected bubbles first turn to the right. This first displacement to the right of the nozzle axis might be due to the Coriolis force ($F_C = 2\rho_l V v \omega_{LDC} \sin\alpha$, where V is the bubble's volume, v its velocity, $\omega_{LDC} = \left(\frac{\sqrt{g^2-g_0^2}}{R_{LDC}}\right)$ is the angular velocity of

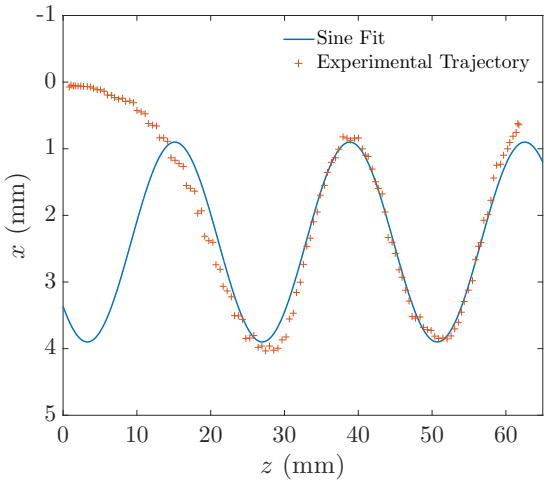

Figure 5.17: Experimental bubble path at $5g_0$ fitted with a sine function.

the LDC, and α is the angle between v and ω_{LDC}), which is perpendicular to the velocity of the bubble.

Suñol & González-Cinca (2015) explain that the oscillatory rising trajectory is due to the interaction between F_{By}, F_C, lift force F_L and drag force F_d. Typically, F_L is related to the wake vortices, and $F_d = \frac{1}{2}\rho C_d S U^2$, where C_d is the drag coefficient and S is the projected area of the bubble. It should be noted that the Reynolds number ($Re = v d_e/\nu$) for these experiments ranges between 448 and 627.

As shown in previous works (de Vries et al. (2002); Tagawa et al. (2014)), bubbles following a zig-zag trajectory have a double-threaded wake, and it is the periodic vortex shedding of these bubbles that cause this motion. The frequency of the vortex shedding, f_s, from the rear part of a rigid sphere is (Tagawa et al. (2014); Suñol & González-Cinca (2015))

$$f_s = \frac{p\nu\,\mathrm{Re}}{\pi d_e^2}, \tag{5.10}$$

where p is a parameter that depends on the shape of the bubble. Tagawa et al. (2014) obtained $p = 0.3$ for a zigzagging bubble in a surfactant solution that has a spherical shape and drag coefficient close to a rigid sphere. Suñol & González-Cinca (2015) found $p = 0.265$ for their experiments, which is an indication that bubbles were not spherical but oblate spheroids in their approach.

The frequency of the oscillatory trajectories was measured for different cases. Since there are slight variations between each trajectory, we measured 10 bubble trajectories for each case. As can be observed in Figure 5.3, the oscillation is not apparent in the $2g_0$ case. However, it was not possible to obtain the frequency by filtering the trajectory with MATLAB and subtracting it from the original one.

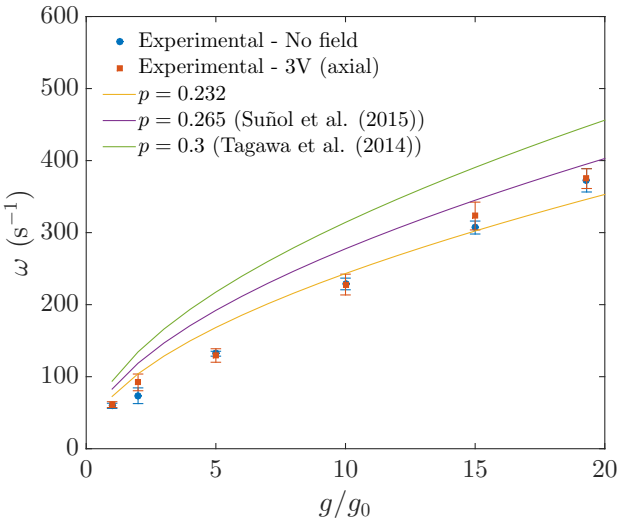

Figure 5.18: Frequency of the oscillatory motion as a function of the gravity level (no field and 3 V axial field). Solid lines correspond to theoretical predictions from equation 5.10 when no acoustic field is applied. Error bars show the standard deviation of the frequency.

Figure 5.18 shows the measured frequencies from our experimental data. Here we can observe the frequencies when no acoustic field is applied as well as the theoretical prediction. Compared to Tagawa et al. (2014) and Suñol et al. (2011), we obtained a lower value of p, which might indicate that the shape of the bubbles in the present experiments are not spherical and slightly more deformed than those from Suñol & González-Cinca (2015), even though the bubble sizes in their experiment were similar to ours. Moreover, the frequencies measured in the axial acoustic field case while applying 3 V are also shown. It can be observed that the frequency of the zig-zag motion is very close to that without the acoustic field. Thus, it seems that the frequency of the zig-zag motion is not affected by a low pressure acoustic field.

The amplitude of the oscillatory trajectories was also studied. Data corresponding to $1g_0$ and $2g_0$ have been excluded due to large statistical deviation. We have plotted the obtained amplitudes in Figure 5.19. Below $10g_0$, the amplitude of the trajectories under the effects of the acoustic field are lower. However, for larger gravity levels, the amplitude is closer to that without the acoustic field, although the error is larger.

The x coordinate is shown in Figure 5.20 as a function of time, both with (left) and without (right) the field at $5g_0$ and $15g_0$. It is observed that when there is no field, bubbles tend to follow a similar oscillatory trajectory in approximately the same region on the x-axis; when we apply the field, there is more dispersion. Even when observing a plane of the axial field, the pressure is not perfectly uniform over that plane (for instance, due to reflections), and it causes the bubble to take slightly

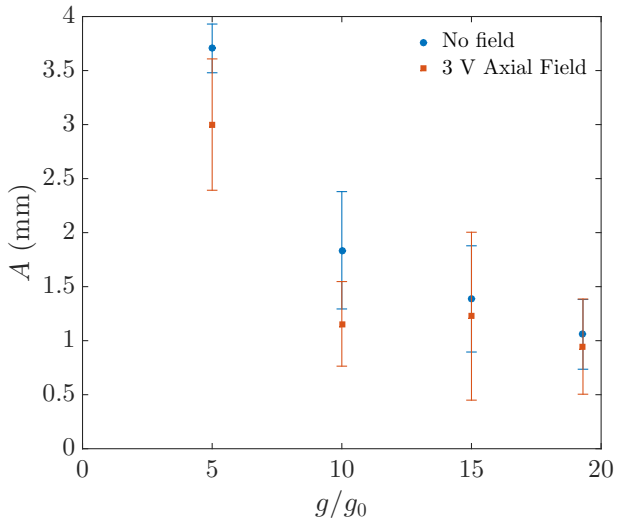

Figure 5.19: Amplitude of the oscillatory paths as a function of the gravity level. Error bars show the standard deviation of the amplitude.

different directions path after path.

5.4.5 Terminal Velocities

The last part of the experimental data study focuses on the terminal velocity of the rising bubbles without an acoustic field. With an acoustic field, bubbles do not reach a terminal velocity but instead their velocity slightly oscillates as they rise.

Compared to the hypergravity experiments carried out by Suñol & González-Cinca (2015), higher velocities were obtained in this experiment (Figure 5.21), which might be due to the fact the injection was not of isolated bubbles but of trains (or chains) of bubbles. Hence, the wake of the leading bubble could cause the trailing bubble to reach slightly larger velocities. We discarded the possibility that inertial effects at the detachment were causing the bubbles to rise faster, since when we studied the bubble generation (Section 5.4.2) we found that the diameters obtained experimentally were in good agreement with the analytical expression (which only takes into account the buoyancy and surface tension forces upon detachment).

In Figure 5.21, the experimental results of the terminal velocities are plotted from our tests injecting air at a flow rate of 1 ml/min, and those from Suñol & González-Cinca (2015) at 1 nl/min. The theoretical prediction corresponds to the model for a non-spherical bubble from Mendelson (1967); Tomiyama et al. (1998),

$$v_t = \sqrt{\frac{2\sigma}{\rho_l d_e} + \frac{g d_e}{2}}, \tag{5.11}$$

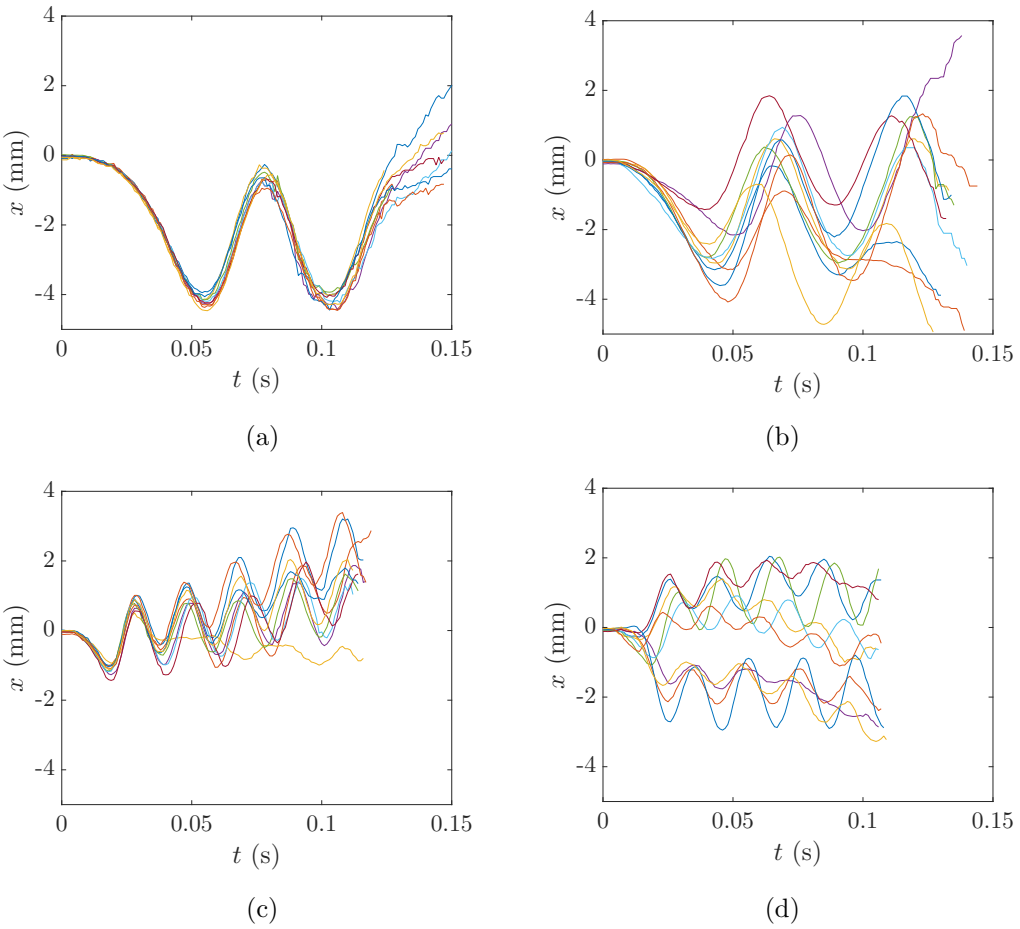

Figure 5.20: x coordinate with respect to time for (a) $5g_0$ no field, (b) $5g_0$ axial field at 3 V, (c) $15g_0$ no field and (d) $15g_0$ axial field at 3 V.

where v_t is the terminal velocity and d_e can be substituted by equation 5.2. It can be seen that there is good agreement between the model and the experimental data at low flow rates in Suñol & González-Cinca (2015) (same fluid properties and bubble diameters, but lower flow rate than the present experiment).

Nonetheless, since the case of the present experiment considers bubble trains, it is important to take into account effects from the wake when studying the terminal velocity. In Figure 5.22, a graphical sketch of the flow between two bubbles is presented. According to Zhang & Fan (2003), the trailing bubble experiences significant acceleration due to the wake of the leading bubble. Thus, the wake effect needs to be taken into account when calculating the terminal velocity of the trailing bubble.

In order to study these higher terminal velocities, a model obtained by Zhang & Fan (2003) is considered, which assumes that the motion of the trailing bubble is

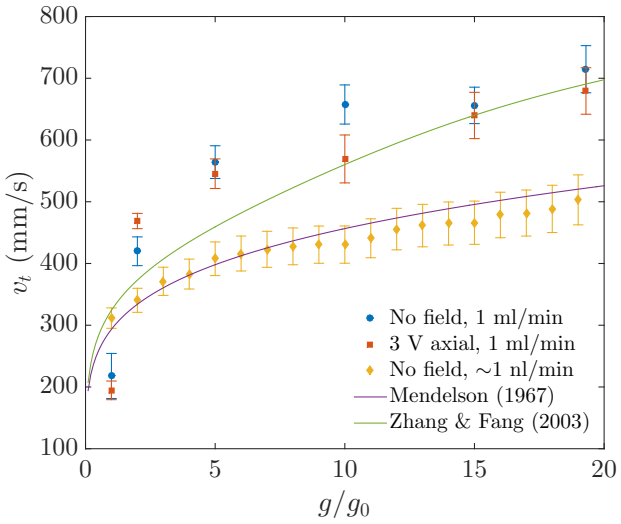

Figure 5.21: Measured terminal velocities as a function of the gravity level, when there is no field and at 3 V axial field, flow rate 1 ml/min. Terminal velocities for bubbles injected at 1 nl/min from Suñol & González-Cinca (2015). The solid purple line corresponds to equation 5.11 and the solid green line corresponds to equation 5.12.

in a quasi-steady state, which means that the added mass and Basset forces can be neglected. In this model, only the wake effect is considered to be an influence on the motion of the bubble. Taking into account that only the buoyancy and drag forces have an effect, they obtained

$$v_t^* = 1 + \frac{C_{d0}}{2}\left[1 - \exp\left(-\frac{Re_0}{16x^*}\right)\right] \tag{5.12}$$

where $C_{d0} = 4gd_e/3v_{t0}^2$ and Re_0 are the drag coefficient and the Reynolds number of a single isolated bubble, respectively. The asterisk denotes non-dimensional quantities which are: $v_t^* = v_t/v_{t0}$, where v_t and v_{t0} are the terminal velocities of the trailing bubble and the isolated bubble, respectively; and $x^* = d_b/d_e$, where d_b is the separation distance between the bottom edge of the leading bubble and the top edge of the trailing bubble. Thus, in order to calculate the final velocity from this model, the separation between the bubbles at each gravity level is required. For each gravity level, d_b has been measured at the applied flow rate (i.e. 1 ml/min). Figure 5.23 shows the values obtained, where the solid line corresponds to an exponential fit ($d_b = a\exp(bg/g_0)$ in mm, where a = 63.67 and b = -0.1537).

To obtain the terminal velocities by means of equation 5.12, we used equation 5.2 for d_e, equation 5.11 for v_{t0} and the exponential fit for the distance of separation between bubbles d_b. The result can be seen in Figure 5.21 (solid green line). It can be observed that for high gravity level values, the resulting value is quite close to that

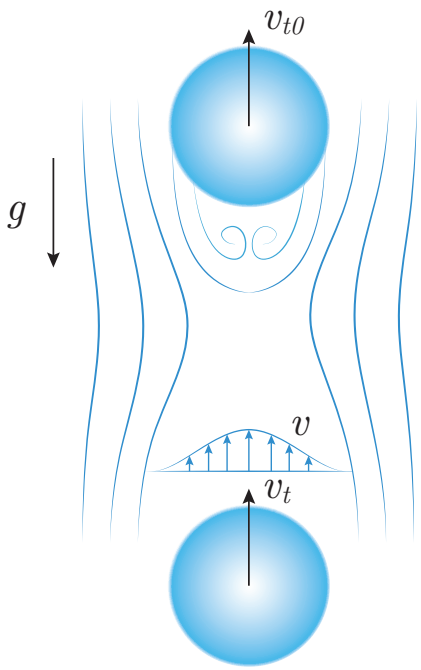

Figure 5.22: Diagram of the flow between two bubbles due to wake attraction.

obtained experimentally. However, at low gravity levels the experiment deviates from the theoretical prediction. This might be due to the distance between the leading and trailing bubble. Since it is larger at lower gravity levels, it is possible that the effects of the wake are lower and thus equation 5.12 might no longer be valid.

5.5 Experimental Conclusions

We observed many different phenomena resulting from the action of acoustic fields, the consequences of increasing the gravity level in these cases, and then compared them with cases without an acoustic field.

Due to the large amount of data and the observed effects, a qualitative analysis was carried out in order to provide an overview of all of the effects caused by the acoustic waves.

During detachment, different effects caused by the acoustic waves were observed: downwards, uneven and uniform detachment. Compared to the experiments without acoustic fields, all the effects studied for V $>$ 3 V indicate that the detachment depends strongly on the driving voltage. We also observed a change in the bubble diameter upon detachment when applying the acoustic field.

The rise of the bubbles was very diverse in that they deviate to the left or to the right of the nozzle injection axis. From the tests we were able to observe that, with

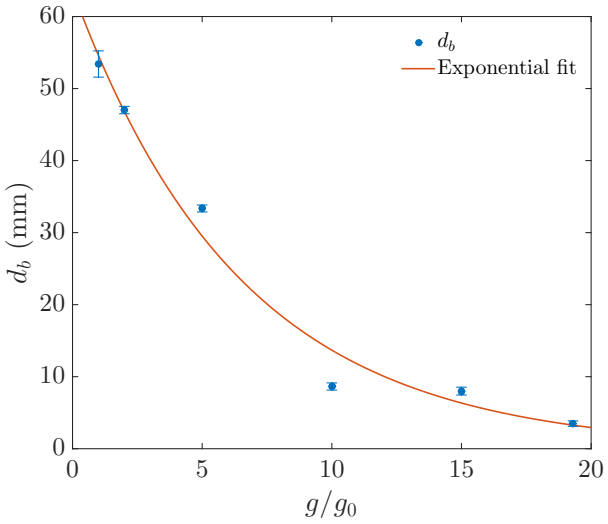

Figure 5.23: Separation between leading and trailing bubble, for a flow rate of 1 ml/min at all the gravity levels explored.

the transverse field, bubbles indeed tend to deviate to the nodes or antinodes of the wave, depending on the bubble size. This effect becomes weaker at higher g-levels (buoyancy force dominating over acoustic forces), especially when applying the axial acoustic field. However, bubbles take longer to reach the free surface when acoustic fields are applied (this can actually be seen in the overlapped images, where darker paths imply slower motion). Moreover, bubbles rise following different paths when compared to the tests without an acoustic field.

In order to complete the quantitative results, acoustic pressure measurements inside the test cell were carried out in order to know the pressure of the wave inside the cell, as well as the value of the pressure at certain points.

We also carried out a quantitative study of the detachment size, the oscillatory rising trajectories and terminal velocities when the axial acoustic field is applied. This case presented the most reproducible results, while the effects observed from the transverse field were more random. Regarding bubble detachment, we obtained good agreement with the analytical expression of the diameter. Moreover, an expression for estimating the detachment diameter when an acoustic field is applied was proposed, which shows good agreement with the experimental data.

With regards to the zig-zagging paths of the bubbles, we saw that the acoustic field does not have a great effect on the frequency. However, it does affect the trajectory and amplitude slightly. The Coriolis force only affects the initial deviation of the bubble, but not the oscillatory trajectory. Finally, when considering the terminal velocity of bubbles, it was observed that there were chains of bubbles in

these experiments instead of isolated ones; thus, the effect of the wake of the leading bubble on the trailing bubble needs to be considered. The theoretical model used is in good agreement at high gravity levels, while at low gravity levels the separation between bubbles is larger; hence, the effects of the leading/trailing bubble are lower.

5.6 Numerical Analysis

This section presents two different studies to explore the dynamics of a rising bubble (not in a train). First, an analytical study of the force balance equation. Secondly, numerical simulations carried out by means of the fluid dynamics numerical code JADIM.

The dynamics of a rising bubble when an acoustic field is applied at different gravity levels was studied analytically. Test simulations and integration of the acoustic field in the code were performed during the numerical simulations

5.6.1 Force Balance Analysis

To get a prediction of the bubble trajectory in one dimension when applying the acoustic field, Newton's second law was solved on a spherical rising bubble. The calculations are based on the numerical analysis presented in Abe et al. (2002), which qualitatively agrees with their experimental results. In order to obtain the motion of the bubble, two equations need to be solved simultaneously. Assuming a spherical bubble that expands and contracts adiabatically in a standing wave field, the bubble radius can be obtained by means of the Rayleigh-Plesset equation

$$R\frac{\mathrm{d}^2R}{\mathrm{d}t^2}+\frac{3}{2}\left(\frac{\mathrm{d}R}{\mathrm{d}t}\right)^2+\frac{4\eta_l}{\rho_l R}\frac{\mathrm{d}R}{\mathrm{d}t}=\frac{1}{\rho_l}\left(P_g-P_l+P_v-\frac{2\sigma}{R}\right), \tag{5.13}$$

where R is the time-dependent bubble radius, η_l is the dynamic viscosity, ρ_l is the liquid density, σ is the surface tension, P_g is the gas pressure, P_l is the resultant liquid pressure when the acoustic field is applied, and P_v is the vapour pressure within the bubble. To obtain the translational motion of the bubble, the force balance equation needs to be solved

$$m_b\frac{\mathrm{d}u_b}{\mathrm{d}t}=-V\frac{\mathrm{d}P_l}{\mathrm{d}z}-\frac{1}{2}\rho_l\frac{\mathrm{d}}{\mathrm{d}t}(Vu_r)-\frac{1}{2}\rho_l u_r^2 AC_d+V(\rho_l-\rho_g-\rho_v)g, \tag{5.14}$$

where m_b is the mass of the bubble expressed as $m_b=\frac{4}{3}\pi R_0^3\rho_g$, ρ_g is the gas density, ρ_v is the vapour density, $V=\frac{4}{3}\pi R^3$ is the bubble volume, u_r is the relative velocity between the bubble and the liquid, A is the area of the cross-section of the bubble (which is $A=\pi R^2$), C_d is the drag coefficient, and g is the acceleration of gravity. Finally, u_b is the bubble translational velocity defined as

$$\frac{\mathrm{d}z}{\mathrm{d}t} = u_b. \tag{5.15}$$

If we examine the terms on the right-hand side of equation 5.14, the first term corresponds to the primary Bjerknes force, the second term is the added mass force, the third term is the viscous drag force, and finally the last term corresponds to buoyancy force.

To obtain the bubble's trajectory the ordinary differential equations 5.13, 5.14 and 5.15 need to be numerically solved. However, a change of variable is required to convert equation 5.13 into two first-order ordinary differential equations (we will use the same nomenclature as in Watanabe & Kukita (1993))

$$R\frac{\mathrm{d}Q}{\mathrm{d}t} + \frac{3}{2}Q^2 + \frac{4\eta_l}{\rho_l R}Q = \frac{1}{\rho_l}\left(P_g - P_l + P_v - \frac{2\sigma}{R}\right), \tag{5.16}$$

$$\frac{\mathrm{d}R}{\mathrm{d}t} = Q. \tag{5.17}$$

Additional equations are required to solve equations 5.16 and 5.17. Assuming that the process is adiabatic with polytropic index γ, the gas pressure in the bubble can be expressed as

$$P_g = P_{g0}\left(\frac{R_0}{R}\right)^{3\gamma}, \tag{5.18}$$

where P_{g0} is the equilibrium gas pressure in the bubble (subscript 0 denotes equilibrium conditions)

$$P_{g0} = \frac{2\sigma}{R_0} + P_{l0} - P_v. \tag{5.19}$$

The resultant pressure in the liquid while the acoustic field is applied is

$$P_l = P_{l0} + P_{ac}\cos(\omega t)\sin(kz), \tag{5.20}$$

where P_{ac} is the pressure amplitude of the acoustic field, ω is the angular frequency $\omega = 2\pi f$, where f is the frequency of the field, and k is the wave number. The wave number is defined as $2\pi/\lambda$ and the wavelength $\lambda = c/f$, where c is the speed of sound in the liquid.

The relative velocity mentioned in equation 5.14 can be expressed as

$$u_r = u_b - u_l, \tag{5.21}$$

where u_l is the velocity in the liquid, and it is defined as (Abe et al. (2002))

$$u_l = -\frac{kP_{ac}}{\omega\rho_l}\sin(\omega t)\cos(kz). \tag{5.22}$$

Finally, in the calculations we will consider two drag coefficients to input in equation 5.14. First, we will use the drag coefficient obtained experimentally by Crum (1975)

$$C_d = 27Re^{-0.78}, \tag{5.23}$$

where Re is the Reynolds number defined as

$$Re = \frac{2\rho_l |u_r| R}{\eta_l}. \tag{5.24}$$

Secondly, we will also test the drag coefficient proposed by Mei et al. (Mei et al., 1994; Magnaudet & Eames, 2000), which is valid for high and low Reynolds numbers

$$C_d = \frac{16}{Re}\left\{1 + \left[\frac{8}{Re} + \frac{1}{2}(1 + 3.315Re^{-1/2})\right]^{-1}\right\}. \tag{5.25}$$

Two different drag coefficients were tested in order to debug the code, and to then compare how they fit to the actual experimental result. To solve the system of ordinary differential equations 5.14 to 5.17, the Runge-Kutta-Gill fourth order method was used. This method and the mathematical development for implementing the equations into the code are explained in Appendix C.

Code Implementation and Test Cases

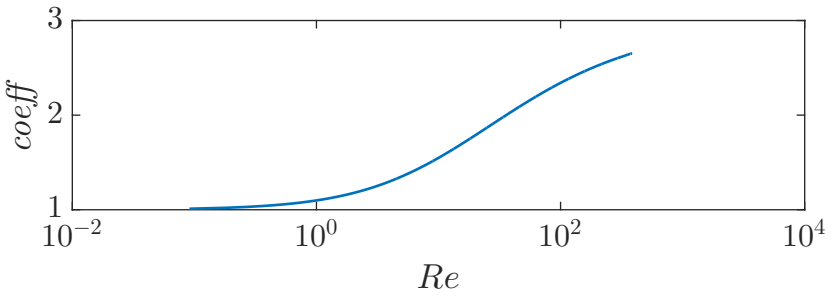

Figure 5.24: *coeff* variation for the Re range of the experiments.

Initially the numerical code was implemented in MATLAB, but the complexity of the equations led to MATLAB requiring very much computational time to solve it. Thus, a code in FORTRAN was written (see Appendix D) to solve the force balance and Rayleigh-Plesset equations by means of the Runge-Kutta-Gill method.

First, Mei's model of the drag coefficient was tested to see its behaviour with respect to Re (from close to zero up to the terminal velocity of the bubble), and as a test to see if the numerical method was properly implemented. Results are

presented in Figure 5.24, where *coeff* represents the term between the curly brackets in equation 5.25, which is expected to be close to 1 for low Re and 3 for high Re. The curve does not reach higher values of Re because it corresponds to the maximum velocity that the test bubble achieved.

The following step was performed to obtain a figure similar to Figure 7 in Abe et al. (2002), which shows the trajectories of bubbles with different radii. Since the values used for their calculations were not mentioned in the paper, we used the values from Watanabe & Kukita (1993) that are shown in Table 5.3, first by using Crum's drag coefficient (equation 5.23) followed by Mei's (equation 5.25).

Physical properties					
σ	$7.2{\cdot}10^{-2}$ N/m	η_l	$8.9{\cdot}10^{-4}$ Pa·s	P_{l0}	100000 Pa
ρ_l	997.4 kg/m^3	g	9.81 m/s^2	P_v	3170 Pa
ρ_g	1.2 kg/m^3	γ	1.4	P_{ac}	20000 Pa
ρ_v	0.77 kg/m^3	c	1500 m/s	f	14580 Hz

Table 5.3: Physical properties used in Watanabe & Kukita (1993).

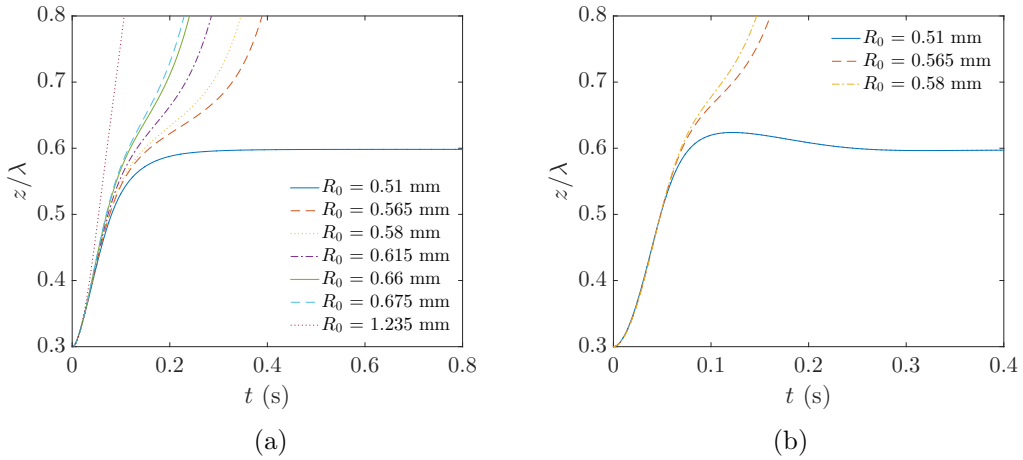

Figure 5.25: Bubble trajectories along the z axis using two different C_d. Acoustic field set at $f = 14.58$ kHz, $P_{ac} = 20$ kPa. (a) Crum's C_d, (b) Mei's C_d.

Figures 5.25a and 5.25b show the trajectories obtained when using the values in Table 5.3 and applying the drag coefficient from equations 5.23 and 5.25, respectively, which were used to solve the force balance coupled with the Rayleigh-Plesset equation. Figure 5.25a was obtained by calculating all of the trajectories for the same radius values as Abe et al. (2002). With the values used, it was not possible to obtain the identical bubble behaviour as in the article, although it was very close.

This is probably because the frequency used and other physical parameters were not exactly the same, since they are not mentioned in the article. However, as the bubble size increases for this acoustic field, the tendency of the trajectories is the same as in their paper. The bubbles, which rise along the direction of propagation of the field, stabilise at different points depending on their size and the pressure field. In this case, a bubble stabilises above $z/\lambda = 0.5$, which corresponds to the node of the acoustic pressure field. That is the point where the acoustic force balances the buoyancy force. Thus, the larger the bubble, the larger the buoyancy force, which will cause the bubble to be trapped slightly above the pressure node or to not be trapped at all.

Another test case is to remove gravity, which means that the bubble should be trapped exactly at the node of the acoustic field. Figure 5.26 shows the trajectories of a bubble with the same characteristics when it is under microgravity conditions and $1g_0$ (where $g_0 = 9.81$ m/s^2), similar to Figure 8 in Abe et al. (2002). As expected, a bubble in microgravity will be trapped exactly at the node of the acoustic wave, because there is no buoyancy to compensate. In the cases in Figure 5.25, the initial position of the bubble is closer to the node at $z/\lambda = 0.5$, otherwise it will either go to $z/\lambda = 0$ or $z/\lambda = 1$, depending on its starting position. Comparing both cases, the bubble will have similar behaviour at both gravity levels. Because the amplitude of the pressure field is higher in this case than in the case with gravity, the bubble will have a greater velocity, which will generate an overshoot trajectory that will later stabilise. This will occur much faster than what is observed in Figure 5.25.

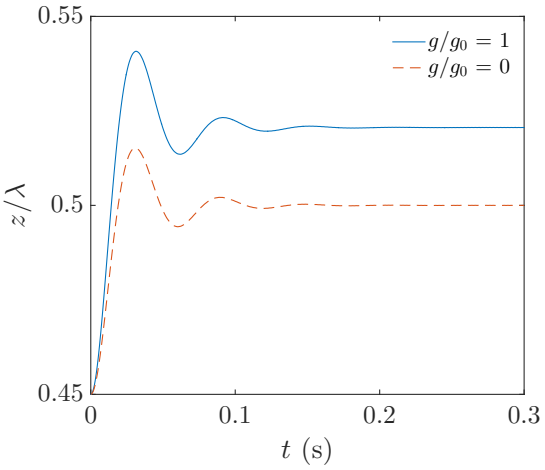

Figure 5.26: Bubble trajectories of a bubble with the same parameters under $0g_0$ and $1g_0$. Acoustic field set at $f = 19.6$ kHz, $P_{ac} = 60$ kPa.

Parametric Study

With the previous results in mind, a parametric study of the trajectories was carried out by basically looking at the effects of different pressures and different radii on the bubble trajectory. For this study, the values of air and water were taken at 25°C and the standard atmosphere as shown in Table 5.4. For the study of different acoustic pressures, the radius was fixed at $R_0 = 0.5$ mm. This was chosen because levitation was observed experimentally at $2g_0$ for this bubble size and when an acoustic field of 60 kHz is applied along the axis of gravity. To obtain the vapour density we used $\rho_v = 0.0022 P_v/T$.

Physical properties					
σ	$7.2{\cdot}10^{-2}$ N/m	η_l	$8.902{\cdot}10^{-4}$ Pa·s	P_{l0}	101325 Pa
ρ_l	997.07 kg/m^3	g	9.81 m/s^2	P_v	3169.8 Pa
ρ_g	1.1735 kg/m^3	γ	1.4	P_{ac}	50000 Pa*
ρ_v	0.77 kg/m^3	c	11496.69 m/s	f	60000 Hz

Table 5.4: Physical properties for the case of liquid and air at 25°C. *Value used when calculating the trajectories for different bubble radii.

As mentioned above, calculations were made for different acoustic pressures and assuming a frequency of 60 kHz, because this is the frequency used along the axis of gravity in the experiments at different gravity levels. Moreover, two tests were performed by placing the bubble at two different initial positions, i.e. at $z/\lambda = 0$ and $z/\lambda = 0.2$.

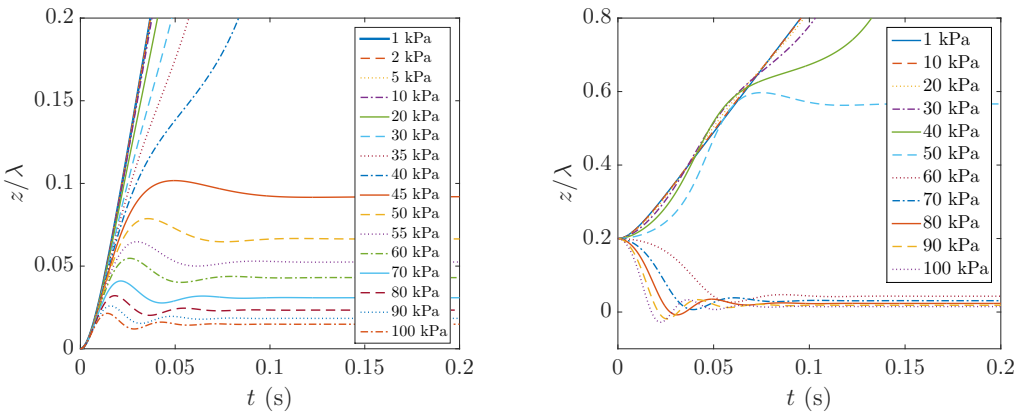

(a) (b)

Figure 5.27: Bubble trajectories of a bubble with $R_0 = 0.5$ mm at different acoustic pressures and a $f = 60$ kHz. (a) From $z/\lambda = 0$, (b) From $z/\lambda = 0.2$.

First, the calculations for different pressures starting from $z/\lambda = 0$ are presented in Figure 5.27a. It can be observed that, for lower pressures, the bubble just rises. As the pressure increases, the rise-time increases too. From 45 kPa the bubble is trapped at the position of equilibrium. Since the closer node from the initial position is $z/\lambda = 0$, the position of levitation gets closer to this node as the acoustic force gets stronger. If the initial position is moved to $z/\lambda = 0.2$, we obtain the trajectories shown in Figure 5.27b. As previously observed, the bubble rises up at low pressures. As the pressure is increased, the rising time is longer. If we observed more wavelengths at $P_{ac} = 40$ kPa, the bubble rises following an oscillatory path, slows down after passing a node, and then accelerates afterwards. At 50 kPa, we observe that this is the first pressure that can trap a bubble at the equilibrium position slightly above the node at $z/\lambda = 0.5$. If the pressure is increased above 50 kPa, the values are high enough to make the bubble go down and become trapped at the equilibrium position close to the node at $z/\lambda = 0$.

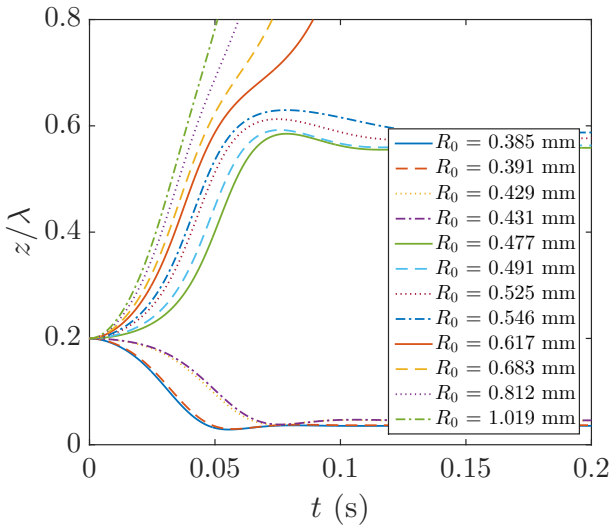

Figure 5.28: Bubble trajectories of different radii at $P_a c = 50$ kPa and a $f = 60$ kHz, starting from $z/\lambda = 0.2$.

From the tests at different pressures, it can be determined that the pressure to be studied when changing the bubble radius will be 50kPa, since this is the first value to levitate a bubble in the previous tests. Figure 5.28 shows the trajectories for different radii of the bubble. The radius values chosen where those observed experimentally. As experimentally observed, bigger bubbles rise up to the free surface with the acoustic field barely affecting them. As the bubble size decreases, their path gets more affected as they follow an oscillatory rising path or get trapped close to the node.

When the size is sufficiently small, bubbles go down closer to the node at $z/\lambda = 0$. This actually fits with experimental observations: at high acoustic pressures, it was observed that the size of the injected bubbles is very small, and they move down the nozzle and start to coalesce there. After they reach a certain size, they detach and rise up to the free-surface.

All of the results observed present similarities with the experiments at different acoustic pressures and bubble sizes, which are presented in Section 5.4. We have observed bubbles escaping the effects of the acoustic field, others rising following oscillatory paths and even slowing down at some points, bubbles levitating after being detached from the nozzle, and finally bubbles going down the nozzle. Figure 5.29 shows the actual z trajectories from the experimental results. It can be seen that the trajectories qualitatively agree with the theoretical results shown previously. The effect on the bubbles from increasing the pressure amplitude can be seen. In the case of Figure 5.29d, which corresponds to a pressure field of 6 V, the tracks correspond to bubbles of slightly different sizes. It can be seen that one of the bubbles remains close to $z/\lambda = 0.6$ for a longer time, which is because the bubble is smaller and finally overcomes the pressure as a result of a second bubble coalescing; thus, buoyancy becomes stronger.

5.6.2 JADIM

JADIM is a numerical code developed at the IMFT (Institute de Mécanique des Fluides de Toulouse). It provides an accurate description of different physical phenomena in multiphase flows by solving the three-dimensional Navier-Stokes equations, both incompressible and non-stationary.

Code Modification

As mentioned above, JADIM solves the Navier-Stokes equations, which need to be taken into account in order to add the external pressure field from the incident acoustic wave. Assuming the fluids to be Newtonian, incompressible and with uniform surface tension, the Navier-Stokes equation can be formulated as

$$\frac{\partial U}{\partial t} + U \cdot \nabla U = -\frac{1}{\rho_l}\nabla P + g + \frac{1}{\rho_l}\nabla \cdot \Sigma - \frac{\sigma}{\rho_l}(\nabla \cdot n)n\delta_I, \tag{5.26}$$

where U and P are the velocity and pressure in the flow, respectively, Σ is the viscous stress tensor, n is the unit normal to the interface going out from phase 1, and δ_I is the Dirac distribution associated with the interface. It is in the first term of the right-hand side where the acoustic pressure needs to be taken into account. This term can be decomposed in

$$-\nabla P = -(\nabla p + \nabla p_{ac}), \tag{5.27}$$

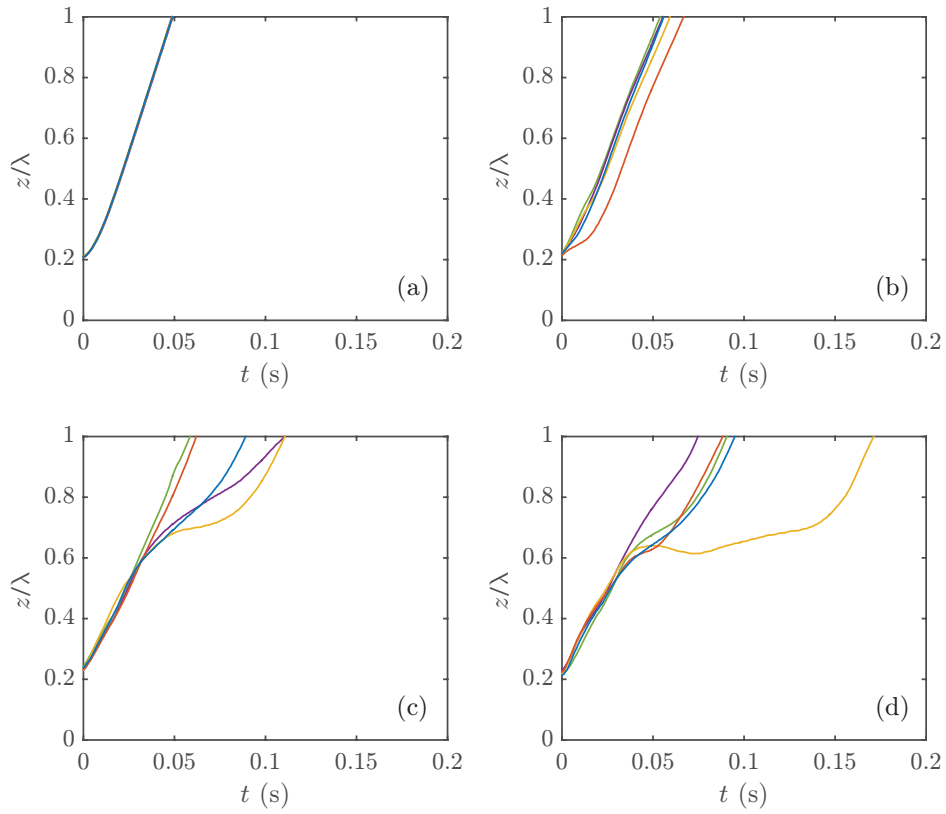

Figure 5.29: z trajectories of experimental bubbles at $2g_0$ applying the axial acoustic field at (1) 3 V, (b) 4V, (c) 5 V and (d) 6 V.

where ∇p is calculated by the numerical code and ∇p_{ac} is where the acoustic pressure will be added.

The pressure and velocity fields caused by the incident acoustic wave on the fluid need to be known before implementing ∇p_{ac} into the code. From Andersen et al. (2009), we can obtain the expression for the velocity potential ϕ_{in} in 2D (i.e. when waves are applied in two directions (x and y))

$$\phi_{in} = \frac{u_0}{k} \cos(k_x x) \cos(k_y y) \cos(\omega t), \tag{5.28}$$

where u_0 is the velocity amplitude and can be expressed as

$$u_0 = \frac{P_{ac}}{\rho_l c} = \frac{P_{ac} k}{\rho_l \omega}. \tag{5.29}$$

From equation 5.28, the velocity can already be obtained (equation 5.30) as well as the pressure (equation 5.31) of the fields.

$$\mathbf{v}_{in} = \nabla\phi_{in} = -\frac{u_0 k_x}{k}\sin(k_x x)\cos(k_y y)\cos(\omega t)\hat{\imath} - \frac{u_0 k_y}{k}\cos(k_x x)\sin(k_y y)\cos(\omega t)\hat{\jmath} \quad (5.30)$$

$$p_{ac} = -\rho_l \partial_t \phi_{in} = \frac{\rho_l \omega u_0}{k}\cos(k_x x)\cos(k_y y)\sin(\omega t) \quad (5.31)$$

If $k_y = 0$ and $k = k_x$, then equations 5.30 and 5.31 become one-dimensional.

Thus, ∇p_{ac} can now be decomposed as follows. After substituting equation 5.29 into equation 5.31, we obtain

$$\nabla p_{ac} = \begin{cases} -P_{ac} k_x \sin(k_x x)\cos(k_y y)\sin(\omega t) \\ -P_{ac} k_y \cos(k_x x)\sin(k_y y)\sin(\omega t). \\ 0 \end{cases} \quad (5.32)$$

These equations will be added to the pressure term in JADIM. In order to activate the acoustic pressure option in the code, the function i_pac was created. The input parameters for simulation are P_{ac}, c, f_x and f_y. These last two are, respectively, the frequency of the waves in directions x (which corresponds to our experimental z-axis) and y (which corresponds to our experimental x-axis), thus maintaining the nomenclature of JADIM's axes.

Verification Study Case

To verify the implementation of the new code in JADIM, one of the 2D bubble test cases from JADIM was used. Initial simulations were carried out in which we observed the imposed field in different situations: with and without bubbles (i.e. single- and two-phase flows) as well as with and without time variations. The 2D domain of this case can be observed in Figure 5.30.

This case has $\rho_l = 1000$ kg/m^3, $\rho_b = 10$ kg/m^3, $\eta_l = 0.68415{\cdot}10^{-1}$ Pa·s, $\eta_b = 0.68415{\cdot}10^{-3}$ Pa·s and $\sigma = 0.3442$ N/m at normal gravity. Its corresponding Bond ($Bo = \rho_l g d^2/\sigma$) and Archimedes ($Ar = \rho_l (gd)^{1/2} d/\eta_l$) numbers are 2.85 and 45.78, respectively.

First, forcing was added in JADIM considering no time variation. This initial code modification was tested on a single-phase case and by considering different wavelengths. The pressure fields obtained from these simulations can be observed in Figure 5.31, where the imposed acoustic field can be observed. Periodic boundary conditions are chosen on the four walls so that an object crossing one boundary would

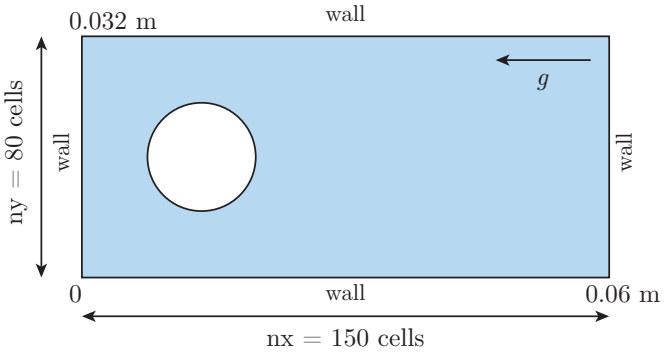

Figure 5.30: Scheme with parameters of the JADIM test case.

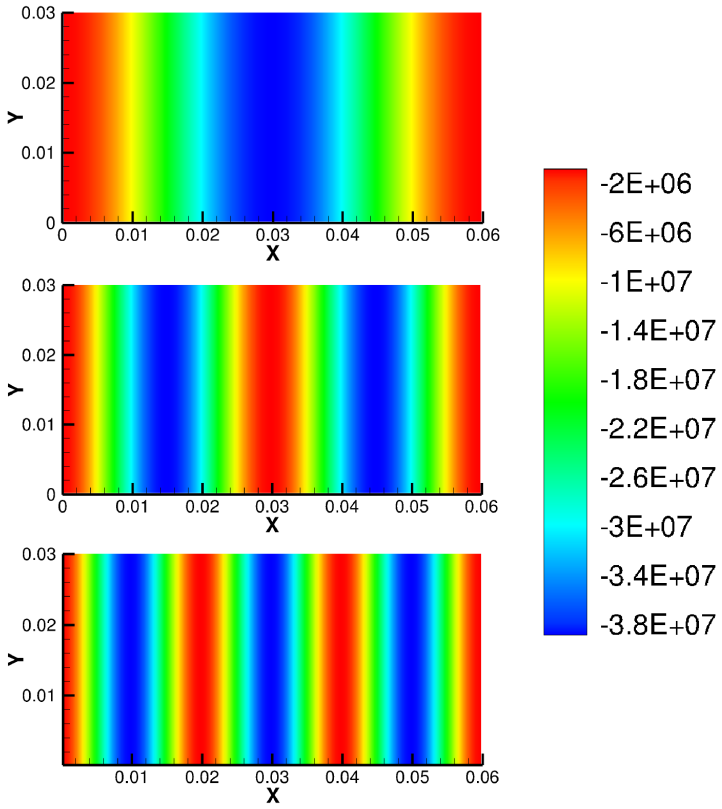

Figure 5.31: Simulated pressure field due to a standing wave when the wavelength corresponds to λ, 2λ and 3λ. One wavelength is from peak to peak (i.e. maximum pressure to maximum pressure).

re-appear at the opposite boundary. It can be seen that the pressure distribution

follows a sinusoid along the x axis for different wavelengths tested.

In JADIM, the pressure is calculated by taking a reference point on the grid. This point can be moved and, hence, affect the solved pressure with the code. We have tested this reference point at its default position, at the theoretical position of a node and, finally, at an antinode. These changes affect the maximum and minimum pressures, but the amplitude remains the same for all of them. For instance, if we take a node as a reference point, the minimums and maximums of the pressure wave vary from -P to P. However, if we choose an antinode, they vary from 0 to 2P. That is because the reference at the node pressure will be 0, while at the antinode it will be P.

When considering a two-phase system in which we add the bubble shown in Figure 5.30, the bubble motion is similar to when there is no field. Moreover, in the first step (when the simulation goes from initial conditions to adding the acoustic field), the bubble breaks up. This can be avoided by reducing the acoustic pressure. Figure 5.32 shows the bubble breaking up, where blue corresponds to the liquid phase and red to the gas phase, while the rest corresponds to the interphase.

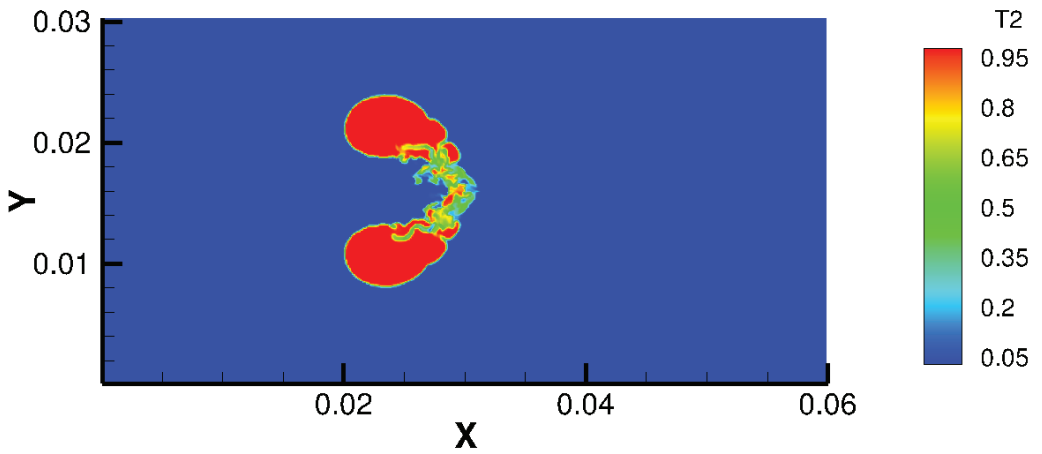

Figure 5.32: Verification case with a pressure field. Colour scale represents the phase (blue for liquid, red for air).

Despite the bubble breaking up, we carried out different simulations with the bubble located at different initial positions. A grid with larger cells was used so that the simulations would take less computational time. A frequency of 25 kHz was chosen in order to have 3 antinodes (at $x = 0$, $x = 0.03$ m and $x = 0.06$ m). Note that, as shown in Figure 5.30, gravity is on the x axis. The simulations were carried out for bubbles of $R_0 = 2.5$ mm and an acoustic pressure of 2000 Pa and $g = 9.81$ m/s^2. In the simulation shown in Figure 5.33, the bubble was initially

located at the pressure node, after which it rises up, briefly surpasses $x = 0.03$ m, and then immediately goes back to the antinode $x = 0.03$ m (similar behaviour to the overshooting observed in Figure 5.26). Figure 5.33 shows an overlay of the position of the bubble during 0.12 s. It should also be noted that the bubble initially breaks up (as in Figure 5.32), then rapidly coalesces and rises.

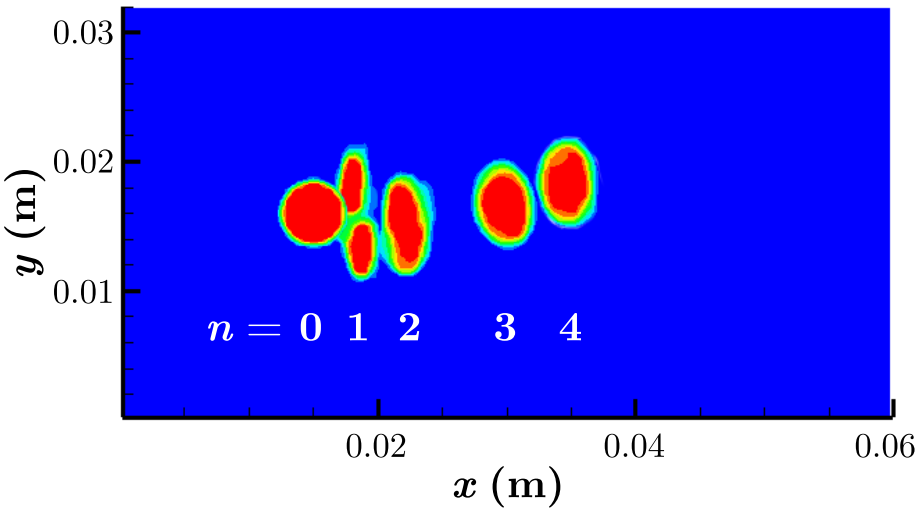

Figure 5.33: Rise of a bubble from the node of the wave to the antinode, where it stabilised. $t = n\Delta t$, where $\Delta t = 0.03$ s.

The same simulation was carried out for a bubble with its initial position at the antinode of the wave. As can be observed in Figure 5.34, the bubble in this case remained at the same position, trapped by the acoustic field at the antinode.

Even though the motion of the bubble qualitatively agrees with the theory, the actual position where the bubble is trapped does not. This is because the bubbles are larger than the size corresponding to a resonance frequency of 25 kHz, i.e. ~ 5 µm ($R_0 \gg R$). Therefore, according to theory, they should move towards the pressure nodes instead.

Due to time constraints of the stay at IMFT, further analysis of the obtained results has not been pursued. It has not yet been possible to identify the reason behind the bubble breaking up and the position of bubble levitation.

5.7 Numerical Analysis Conclusions

In this section, we have carried out a numerical analysis of rising bubbles under the effects of vertical acoustic fields. We were able to create a code that can estimate the stabilisation position of rising bubbles.

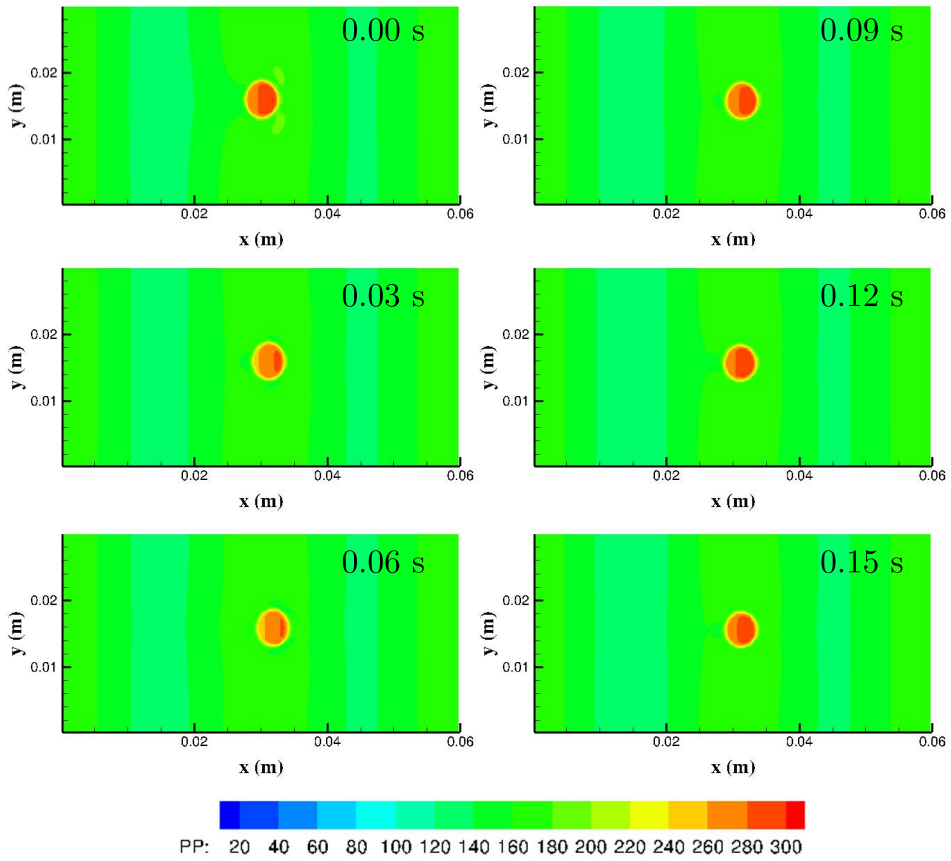

Figure 5.34: Pressure field of a bubble at the antinode of the wave during 0.15 s.

The numerical results qualitatively agree with the experimental observations, and with previously reported results by other researchers.

This numerical code will be useful for future experimental planning so that preliminary studies can be done to design test cells and plan experimental protocols.

As for the numerical simulations with IMFT's code JADIM, we have successfully implemented an acoustic field in the code, generating pressure variations equivalent to those expected from an acoustic field. Simulations on a time-varying pressure field were carried out, successfully trapping bubbles. However, the position of levitation is not that which is expected from theory, which might be due to physical considerations of the numerical code, such as compressibility. Unfortunately, due to the limited duration of the stay, it was not possible to further investigate the application of a field in the test case.

Chapter 6

Conclusions and Outlook

This chapter will review the main conclusions gained from the different experiments and simulations carried out during this thesis. Moreover, it includes some difficulties encountered and recommendations for future experimental setups. Finally, work currently being carried out will be discussed and other suggestions for further investigations are outlined.

Inter-Particle Acoustic Forces

Effects of a standing acoustic wave on microparticles in a microchannel were studied by selecting cases of isolated particles. Due to the size of the particles only a few cases were examined. However, they clearly showed two particles interacting due to inter-particle attractive forces on the acoustic levitation plane.

A method to determine the transverse forces on particles has been described, which can also estimate the magnitude of the Secondary Bjerknes force between two elastic solid particles.

The method presented also allowed to indirectly obtain the acoustic pressure applied. Depending on the experimental setup the acoustic pressure is not always possible to measure. Qualitative agreement has been observed with previous experiments.

The magnitude of the interacting attractive forces has been obtained by the method presented and shows agreement with theoretical predictions.

Low Frequency Vibrations on Two Phase Flows

When low frequency vibrations were applied, different effects were observed on bubbles, depending on their physical properties. A qualitative description of all the observations has been provided.

For the physical parameters of the bubbles in the experiments, high viscosity has shown to be the least susceptible to breakup.

Shape oscillations, usually described for higher frequency vibrations and smaller bubbles were observed, however they seemed highly affected by the walls. Thus, wall effects should not be neglected, since walls constrain the movement of the bubble, especially when the ratio between the bubble volume and the cell volume is high.

When vibrations were applied, bubbles were observed to translate along the walls, depending on how abrupt their shape oscillations were during vibration. Moreover, bubbles separated and approached the walls due to the vertical vibrations.

For the case of silicon oil (high viscosity), after the vibration stopped, the relaxation dynamics of the bubble exponentially decay, while for the other cases bubbles undergo volume oscillations.

Effects of Spin on Two-Phase Flows

A lightweight and small experimental setup to be used in future acoustics experiments was designed and built.

High rotation velocities caused the two-phase system with low surface tension inside the test cell to reorganise along the rotation axis forming a bubble column. Moreover, this allowed us to know the position of the axis of rotation, taking into account the video perspective for the rest of the analysis.

Bubble injection was observed during rotation. Trajectories were measured and compared to analytical predictions, showing good agreement at a high rotation rate, even though the prediction considered a lower rotation rate.

At low rotation velocity effects were more clearly observed on larger bubbles, which quickly positioned themselves close to the axis of rotation. The two-phase system rotated around the axis, but as more bubbles got closer, the amplitude of this rotation decreased.

Finally, at booster separation the larger bubble broke up into two parts, similar to the observations from the previous experiment. Wall effects were greatly reduced in this experiment, because the ratio between the bubble's volume and the test cell's volume was smaller, compared to SL-8.

Effects of Hypergravity and Acoustic Fields on Two Phase Flows

Different effects were observed when an acoustic field was applied on rising bubbles, including: bubble levitation, bubble interactions, diverse rise directions, detachment diameter, oscillatory rising trajectories, deviation from the main trajectories and cavitation.

Regarding detachment a good agreement with previous experiments has been observed when no acoustic field was applied. Bubbles injected were smaller as the gravity level increased. When applying an acoustic field parallel to the rise trajectory, detached bubbles (for the same gravity level) were smaller as the amplitude of the wave increased.

Bubble trains have a significant effect on the terminal velocity. The wake of the leading bubble accelerates the trailing bubble. Good agreement at high gravity levels

was observed for the model used, while at low gravity levels the separation between bubbles is larger, hence the effects of the leading/trailing bubble were lower.

Numerical Analysis

A numerical code was written in order to estimate the position of stabilisation of a rising bubble when a parallel field is applied, showing qualitative agreement with the experimental observations.

The IMFT numerical code JADIM was used to carry out numerical simulations of the phenomena. A large number of tests were carried out to become familiar with the code and also to try different physical properties and grid sizes. A stationary acoustic field was successfully implemented to the code but due to the short stay further simulations were not carried out.

6.1 Difficulties and Recommendations

Each experiment was unique and each posed its own difficulties, below is a list of the most relevant, in no particular order:

- Locating isolated particles in the micro-channel proved to be complicated for several reasons (reduced field of view compared to the channel size, microscope very sensitive to vibrations and aggregates fast formation). A smaller channel with a focalised aggregation point and better fixed microscope could help locate more cases of isolated particles.

- A high speed camera should be used to study secondary forces on bubbles in micro-channels.

- Regarding fish-eye/barrel lenses, even when the image was corrected, it still presented a slight distortion on the edges. Unless necessary, they should be avoided to have an optimal image of the phenomena.

- Effects of rocket spin are more significant than previously anticipated and should not be neglected on fluid dynamics experiments.

- Perspective should be taken into account when analysing data, or two cameras should be used to have two viewing angles (three dimensional analysis).

- Millimetre marks inside the test cell would be helpful to have information about the resolution on each plane depth.

- PZTs work better fixed onto metallic walls with conductive epoxy, the same goes for cables. Soldering wires on the piezo was not very reliable.

- The GoPro camera used proved to be hard to control when wired from a PC. An alternative would be to wirelessly activate it from the PC using a WiFi emitter, or to try different commercially available lightweight small cameras with LabView capabilities.
- The non pressurisation of the module of the experiment inside the rocket may have caused unplanned air injection inside the test cell.
- The numerical code in Appendix D cab be useful for future planning of experimental protocols.

6.2 Future Work

The more one learns, the more questions arise. During the completion of this thesis we have had the opportunity to observe and study several interesting effects. However, some of these effects should be further explored by obtaining additional data in order to complement the analysis.

Currently, we are working on the next generation of the experiment presented in Chapter 4. Instead of bubble injection this experiment goes one step closer to a real scenario, whereby bubbles are generated through boiling. In this experiment we aim to study the heat transfer enhancement by measuring the heat flux in reduced gravity conditions. This will also involve the mass transfer by measuring the bubble growth, detachment and coalescence in a microgravity environment. The experiment was successfully launched on March 15th 2016 on the REXUS 19/20 campaign, from Esrange Space Center, Sweden.

Below is a list of suggestions that would further complement the observations and results obtained in this thesis.

- For the case of particles in micro-channels, it would be interesting to obtain supplementary cases of two individual particles in order to statistically validate the results shown in Chapter 2. This method could also be applied to study of attractive forces between bubbles. This kind of experiment would require a means to inject very small bubbles and a higher speed camera since the process on bubbles takes place much quicker (as was observed on experiments carried out with the same experimental setup).
- Regarding low frequency vibrations; further studies could be carried out to determine which is the most important physical property to determine break-up. Different test cell geometries and volume fractions could be studied in order to obtain more data about shape oscillations and wall effect.
- It would be interesting to further explore the videos recorded in hypergravity, to obtain additional data on the effects of the transverse acoustic field. It would

also be interesting to consider the bouncing process with the free surface while the acoustic field is applied. A series of new tests with a close-up of the nozzle would be useful to further investigate the impact of the acoustic field on the detachment diameter.

- Finally, regarding numerical simulations, further tests could be carried out to understand the bubble breakup occurring when the field is applied and also to correlate the simulations with the experimental data.

Bibliography

Abe, Y., Kawaji, M. & Watanabe, T., 2002. Study on the bubble motion control by ultrasonic wave. *Experimental Thermal and Fluid Science*, **26**, 817–826. ISSN 08941777.

Abramson, S. & Silverman, S., 1966. The dynamic behaviour of liquids in moving containers. 464.

Andersen, L. M., Nysteen, A. & Settnes, M., 2009. *Forces Acting on Microparticles in Acoustofluidic Systems*. Bachelor thesis, Technical University of Denmark.

Annamalai, P., 1982. Bubble migration in a rotating, liquid-filled sphere. *Physics of Fluids*, **25**(7), 1121–1126. ISSN 00319171.

Apfel, R. E., 1988. Acoustically induced square law forces and some speculations about gravitation. *American Journal of Physics*, **56**(8), 726. ISSN 00029505.

Behruzi, P., de Rose, F., Netzlaf, P. & Strauch, H., 2011. Ballistic Phase Management for Cryogenic Upper Stages. In *DLRK (DGLR Conference)*, 9. Bremen, Germany.

Benes, E., Groschl, M., Nowotny, H., Trampler, F., Keijzer, T., Bohm, H., Radel, S., Gherardini, L., Hawkes, J. J., Konig, R. & Delouvroy, C., 2001. Ultrasonic separation of suspended particles. *2001 IEEE Ultrasonics Symposium. Proceedings. An International Symposium (Cat. No.01CH37263)*, 649–659.

Beysens, D., 2004. L'effet des vibrations sur la matière inhomogène: Quelques études en apesanteur. *Comptes Rendus - Mecanique*, **332**, 457–465. ISSN 16310721.

Bjerknes, V. F. K., 1904. Fields of Force. *The Columbia University Press*.

Calliada, F., Campani, R., Bottinelli, O., Bozzini, A. & Sommaruga, M. G., 1998. Ultrasound contrast agents: basic principles. *European Journal of Radiology*, **27 Suppl 2**, S157–60. ISSN 0720-048X.

Carrasquillo, R. L., 2005. ISS ECLSS Technology Evolution for Exploration. In *43rd AIAA Aerospace Sciences Meeting and Exhibit*, no. January 2005, 1–8. Reno, Nevada (USA).

Carrera, J., Parthasarathy, R. & Gollahalli, S., 2006. Bubble formation from a free-standing tube in microgravity. *Chemical Engineering Science*, **61**(21), 7007–7018. ISSN 00092509.

Carter, L., 2010. Status of the Regenerative ECLS Water Recovery System. In *40th International Conference on Environmental Systems*, 1–11. American Institute of Aeronautics and Astronautics, Reston, Virigina. ISBN 978-1-60086-957-0.

Chato, D. J., 2007. Cryogenic Technology Development for Exploration Missions. *NASA STI - Technical Memorandum*, **214824**(September), 1–16.

Collas, P., Barmatz, M. & Shipley, C., 1989. Acoustic levitation in the presence of gravity. *The Journal of the Acoustical Society of America*, **86**(2), 777–787.

Crum, L. A., 1975. Bjerknes forces on bubbles in a stationary sound field. *The Journal of the Acoustical Society of America*, **57**(6), 1363. ISSN 00014966.

de Vries, A. W. G., Biesheuvel, A. & Wijngaarden, L. V., 2002. Notes on the path and wake of a gas bubble rising in pure water. *International Journal of Multiphase Flow*, **28**, 1823–1835.

Doinikov, A. A., 1999. Bjerknes forces between two bubbles in a viscous fluid. *The Journal of the Acoustical Society of America*, **106**(6), 3305. ISSN 00014966.

Eller, A., 1968. Force on a Bubble in a Standing Acoustic Wave. *The Journal of the Acoustical Society of America*, **43**(1), 170–171. ISSN 0020-1669.

Falcon, E., Wunenburger, R., Évesque, P., Fauve, S., Chabot, C., Garrabos, Y. & Beysens, D., 1999. Cluster Formation in a Granular Medium Fluidized by Vibrations in Low Gravity. *Physical Review Letters*, **83**(2), 440–443. ISSN 0031-9007.

Fan, J. M. & Cui, Z., 2005. Effect of Acoustic Standing Wave in a Bubble Column. *Industrial & Engineering Chemistry Research*, **44**, 7010–7018.

Faraday, M., 1831. On a Peculiar Class of Acoustical Figures; and on Certain Forms Assumed by Groups of Particles upon Vibrating Elastic Surfaces. *Philosophical Transactions of the Royal Society of London*, **121**, 299–340.

Farris, S. C., Bugg, J. D. & Gabriel, K. S., 2004. The motion of bubbles in a sinusoidally oscillating liquid in microgravity. *Microgravity - Science and Technology*, **15**, 28–35. ISSN 0938-0108.

Gaddis, E. & Vogelpohl, A., 1986. Bubble formation in quiescent liquids under constant flow conditions. *Chemical Engineering Science*, **41**(1), 97–105. ISSN 00092509.

Gao, J., 1999. Containerless processing of materials by acoustic levitation. *Advances in Space Research*, **24**(10), 1293–1297. ISSN 02731177.

Garcia-Sabaté, A., Castro, A., Hoyos, M. & González-Cinca, R., 2014. Experimental study on inter-particle acoustic forces. *The Journal of the Acoustical Society of America*, **135**(3), 1056. ISSN 1520-8524.

Gor'kov, L., 1962. On the Forces Acting on a Small Particle in an Acoustical Field in an Ideal Fluid. *Soviet Physics -Doklady*, **6**(9), 773–775.

Hung, R. J. & Long, Y. T., 1995. Rotating Liquid Helium Subjected To a Lateral Impulse in Microgravity. *Cryogenics*, **35**(9), 589–597.

Kim, D., Park, J. K., Kang, I. S. & Kang, K. H., 2013. Mechanism of bubble detachment from vibrating walls. *Physics of Fluids*, **25**(2013). ISSN 10706631.

King, L. V., 1934. On the Acoustic Radiation Pressure on Spheres. *Proceedings of the Royal Society A: Mathematical, Physical and Engineering Sciences*, **147**(861), 212–240. ISSN 1364-5021.

Kulkarni, A. a. & Joshi, J. B., 2005. Bubble Formation and Bubble Rise Velocity in Gas - Liquid Systems : A Review. *Industrial & Engineering Chemistry Research*, **44**, 5873–5931. ISSN 08885885.

Kundt, A. & Lehmann, O., 1874. Longitudinal Vibrations and Acoustic Figures in Cylindrical Columns of Liquids. *Annual Review of Physical Chemistry*, **153**, 1.

Leighton, T. G., 1994. *The Acoustic Bubble*. Elsevier. ISBN 9780124419209.

Leighton, T. G., Walton, A. J. & Pickworth, M. J., 1990. Primary Bjerknes forces. *European Journal of Physics*, **11**, 47–50.

Leslie, F., 1985. Measurements of rotating bubble shapes in a low-gravity environment. *Journal of Fluid Mechanics*, **161**, 269–279.

Lum, A. F. H., Borden, M. A., Dayton, P. A., Kruse, D. E., Simon, S. I. & Ferrara, K. W., 2006. Ultrasound radiation force enables targeted deposition of model drug carriers loaded on microbubbles. *Journal of controlled release : official journal of the Controlled Release Society*, **111**(1-2), 128–34. ISSN 0168-3659.

Magnaudet, J. & Eames, I., 2000. The Motion of High-Reynolds-Number Bubbles in Inhomogeneous Flows. *Annual Review of Fluid Mechanics*, **32**, 659–708.

Marston, P. L., 1980. Shape Oscillation and Static Deformation of Drops and Bubbles Driven by Modulated Radiation Stresses – Theory. *Journal of Acoustical Society of America*, **67**, 16–26.

Mei, R., Klausner, J. F. & Lawrence, C. J., 1994. A note on the history force on a spherical bubble at finite Reynolds number. *Physics of Fluids*, **6**(1), 418–420. ISSN 1070-6631.

Mendelson, H. D., 1967. The Prediction of Bubble Terminal Velocities from Wave Theory. *AIChE Journal*, (March), 250–253.

Monti, R., Savino, R. & Alterio, G., 1997. Modelling and Simulation of G-Jitter Effects on Fluid Science Experimentation. Impact on The Utilization of The ISS. *Acta Astronautica*, **40**(2-8), 369–381.

Nyborg, W. L. & Gershoy, A., 1973. Microsonation of cells under near-threshold conditions. *Proceedings of the Second World Congress of Ultrasonics in Medicine*, 360–366.

Pal, P., 2009. Sloshing of Liquid in Partially Filled Container – An Experimental Study. *International Journal of Recent Trends in Engineering*, **1**(6), 1–5.

Pamperin, O. & Rath, H.-J., 1995. Influence of Buoyancy on Bubble Formation at Submerged Orifices. *Chemical Engineering Science*, **50**(19), 3009–3024.

Pédrono, A., 2015. JADIM User Manual.

Pelekasis, N. A., Gaki, A., Doinikov, A. A. & Tsamopoulos, J. A., 2004. Secondary Bjerknes forces between two bubbles and the phenomenon of acoustic streamers. *Journal of Fluid Mechanics*, **500**, 313–347. ISSN 0022-1120.

Plateau, J., 1857. I. Experimental and theoretical researches on the figures of equilibrium of a liquid mass withdrawn from the action of gravity - Third series. *Philosophical Magazine Series 4*, **14**(90), 1–22. ISSN 1941-5982.

Posakony, G. J., Greenwood, L. R. & Ahmed, S., 2006. Stable multibubble sonoluminescence bubble patterns. *Ultrasonics*, **44 Suppl 1**, e445–9. ISSN 1874-9968.

Rabaud, D., Thibault, P., Raven, J.-P., Hugon, O., Lacot, E. & Marmottant, P., 2011. Manipulation of confined bubbles in a thin microchannel: Drag and acoustic Bjerknes forces. *Physics of Fluids*, **23**(4), 042003. ISSN 10706631.

Rastello, M., Marié, J.-L. & Lance, M., 2011. Drag and lift forces on clean spherical and ellipsoidal bubbles in a solid-body rotating flow. *Journal of Fluid Mechanics*, **682**, 434–459. ISSN 0022-1120.

Rayleigh, L., 1884. On the Circulation of Air Observed in Kundt's Tubes, and on Some Allied Acoustical Problems. *Philosophical Transactions Series I*, **175**, 1–21.

Rayleigh, L., 1914. XXII. The equilibrium of revolving liquid under capillary force. *Philosophical Magazine Series 6*, **28**(164), 161–170. ISSN 1941-5982.

Risso, F. & Fabre, J., 1998. Oscillations and breakup of a bubble immersed in a turbulent field. *Journal of Fluid Mechanics*, **372**, 323–355. ISSN 00221120.

Rosenthal, D. K., 1962. The shape and stability of a bubble at the axis of a rotating liquid. *Journal of Fluid Mechanics*, **12**(3), 358–366. ISSN 0022-1120.

Ruggles, J. S., Cook, R. G., Annamalai, P. & Cole, R., 1988. Bubble and Drop Trajectories in Rotating-Flows. *Experimental Thermal and Fluid Science*, **1**(3), 293–301.

Sabbatini, M., 2014. *ESA User Guide to Low Gravity Platforms*. Directorate of Human Spaceflight and Operations, 3rd ed.

Schindelin, J., Arganda-Carreras, I., Frise, E., Kaynig, V., Longair, M., Pietzsch, T., Preibisch, S., Rueden, C., Saalfeld, S., Schmid, B., Tinevez, J.-Y., White, D. J., Hartenstein, V., Eliceiri, K., Tomancak, P. & Cardona, A., 2012. Fiji: an open-source platform for biological-image analysis. *Nature methods*, **9**(7), 676–82. ISSN 1548-7105.

Shklyaev, S. & Straube, A. V., 2009. The impact of bubble diffusivity on confined oscillated bubbly liquid. *Physics of Fluids*, **21**(6), 063303. ISSN 10706631.

Siekmann, J. & Johann, W., 1976. On Bubble Motion in a Rotating Liquid Under Simulated Low and Zero Gravity. *Ingenieur-Archiv*, **45**(5), 307–315.

Sommers, B. S. & Foster, J. E., 2012. Nonlinear oscillations of gas bubbles submerged in water: implications for plasma breakdown. *Journal of Physics D: Applied Physics*, **45**(41), 415203. ISSN 0022-3727.

Straube, A. V., Lyubimov, D. V. & Shklyaev, S. V., 2006. Averaged dynamics of two-phase media in a vibration field. *Physics of Fluids*, **18**(5), 053303. ISSN 10706631.

Suñol, F. & González-Cinca, R., 2015. Effects of gravity level on bubble path instability. *Physical Review E*, **93**(053009), 1–4.

Suñol, F., Maldonado, O., Arco, E. & Garcia-Sabaté, A., 2011. Effects of gravity level on bubble rising, bouncing and coalescence with a free surface. *ESA Spin Your Thesis! Final Report*.

Tagawa, Y., Takagi, S. & Matsumoto, Y., 2014. Surfactant effect on path instability of a rising bubble. *Journal of Fluid Mechanics*, **738**, 124–142. ISSN 0022-1120.

Tomiyama, A., Kataoka, I., Zun, I. & Sakaguchi, T., 1998. Drag Coefficients of Single Bubbles under Normal and Micro Gravity Conditions. *JSME International Journal*, **41**(2), 472 – 479.

Tomsik, T. M., 2000. Recent Advances and Applications in Cryogenic Propellant Densification Technology. *NASA STI - Technical Memorandum*, (March), 15.

Trinh, E. H., Thiessen, D. B. & Holt, R. G., 1998. Driven and freely decaying nonlinear shape oscillations of drops and bubbles immersed in a liquid: experimental results. *Journal of Fluid Mechanics*, **364**, 253–272. ISSN 00221120.

Tsuge, H., Terasaka, K., Koshida, W. & Matsue, H., 1997. Bubble formation at submerged nozzles for small gas flow rate under low gravity. *Chemical Engineering Science*, **52**(20), 3415–3420. ISSN 00092509.

Tsutsui, J. M., Xie, F. & Porter, R. T., 2004. The use of microbubbles to target drug delivery. *Cardiovascular ultrasound*, **2**, 23. ISSN 1476-7120.

UP Aerospace, I., 2012. SpaceLoft XL. Payload Users Guide Lite (PUG Lite).

Urteaga, R. & Bonetto, F. J., 2008. Trapping an Intensely Bright, Stable Sonoluminescing Bubble. *Physical Review Letters*, **100**(7), 074302(1–4). ISSN 0031-9007.

Utsumi, M., 2000. Low-Gravity Sloshing in an Axisymmetrical Container. *Journal of Applied Mechanics*, **67**(June), 344–354.

Veldman, A., Gerrits, J., Luppes, R., Helder, J. & Vreeburg, J., 2007. The numerical simulation of liquid sloshing on board spacecraft. *Journal of Computational Physics*, **224**(1), 82–99. ISSN 00219991.

Versluis, M., Goertz, D. E., Palanchon, P., Heitman, I. L., van der Meer, S. M., Dollet, B., de Jong, N. & Lohse, D., 2010. Microbubble shape oscillations excited through ultrasonic parametric driving. *Physical Review E*, **82**(2), 026321. ISSN 1539-3755.

Watanabe, T. & Kukita, Y., 1993. Translational and radial motions of a bubble in an acoustic standing wave field. *Physics of Fluids A: Fluid Dynamics*, **5**(11), 2682. ISSN 08998213.

Weiser, M. A. H., Apfel, R. E. & Neppiras, E. A., 1984. Interparticle Forces on Red Cells in a Standing Wave Field. *Acustica*, **56**, 114–119.

Woodside, S. M., Bowen, B. D. & Piret, J. M., 1997. Measurement of ultrasonic forces for particle-liquid separations. *AIChE Journal*, **43**(7), 1727–1736. ISSN 0001-1541.

Xi, X., Cegla, F. B., Lowe, M., Thiemann, A., Nowak, T., Mettin, R., Holsteyns, F. & Lippert, A., 2011. Study on the bubble transport mechanism in an acoustic standing wave field. *Ultrasonics*, **51**(8), 1014–25. ISSN 1874-9968.

Xie, W. J., Cao, C. D., Lü, Y. J., Hong, Z. Y. & Wei, B., 2006. Acoustic method for levitation of small living animals. *Applied Physics Letters*, **89**(21), 214102.

Yamakoshi, Y. & Koganezawa, M., 2005. Bubble Manipulation by Self Organization of Bubbles inside Ultrasonic Wave. *Japanese Journal of Applied Physics*, **44**(No. 6B), 4583–4587. ISSN 0021-4922.

Yanagita, H., Abe, Y. & Nakabayashi, S., 2002. SBSL dynamics for bubbles modified by surfactants. *Chemical Physics Letters*, **362**(1-2), 79–84. ISSN 00092614.

Yasui, K., Iida, Y., Tuziuti, T., Kozuka, T. & Towata, A., 2008. Strongly interacting bubbles under an ultrasonic horn. *Physical Review E*, **77**(1), 1–10. ISSN 1539-3755.

Yoshikawa, H., Zoueshtiagh, F., Kurowski, P. & Petitjeans, P., 2010. Bubble splitting in oscillatory flows on ground and in reduced gravity To cite this version : Bubble splitting in oscillatory flows on ground and in reduced gravity. *European Physical Journal E*, **31**, 191–199.

Yosioka, K. & Kawasima, Y., 1955. Acoustic radiation pressure on a compressible sphere. *Acustica*, **5**(3), 167–173.

Zhang, J. & Fan, L. S., 2003. On the rise velocity of an interactive bubble in liquids. *Chemical Engineering Journal*, **92**(1-3), 169–176. ISSN 13858947.

Zoueshtiagh, F., Caps, H., Legendre, M., Vandewalle, N., Petitjeans, P. & Kurowski, P., 2006. Air bubbles under vertical vibrations. *European Physical Journal E*, **20**, 317–325. ISSN 12928941.

Appendix A

SpaceLoft XL

Experiments SL8 and SL9 were launched inside UP Aerospace's Inc. SpaceLoft XL sub-orbital rocket. The vehicle is a single stage rocket with solid booster propulsion. The rocket has a diameter of 26.4 cm and it is 6.1 m height. Its maximum lift-off weight is 254 kg for a standard mission configuration, including payloads. The rocket typically reaches 115 km allowing the experimenters to have about 4 minutes of microgravity. The launches took place in Spaceport America (New Mexico, USA) and touched down on White Sands Missile Range. The typical flight trajectory of the rocket can be observed in Figure A.1.

Before launch, the experiments on the rocket undergo a series of tests and checks to ensure the success of the mission (loads, balancing, integration, interference, launch simulation). Experiments interface with the rocket by means of the Payload Command Module (PCM), which allows each experiment to work independently. The ground station can send discrete signals to each payload and payloads should send its status to the ground segment.

It is important to consider the loads suffered on the vehicle due to the different events occurring during the flight. Table A.1 shows the data provided by UP

Event	Axial Load (g/g_0)	Radial Load (g/g_0)	Comment
Launch	14	4	-
Ascent Maximum Acceleration	16	18.5	Based on maximum spin rate and inner radius of the module
Payload Separation	18	5	1/100 s
Atmospheric Re-entre Deceleration	1-2	5-9	-
Recovery System Deploy	5-8	18-12	-
Vehicle Touchdown	14	8	1/10 s

Table A.1: Loads on the rocket caused by different events during the flight, as measured by the flight provider.

Aerospace Inc. about the different loads measured by the Inertial Measurement Unit (IMU).

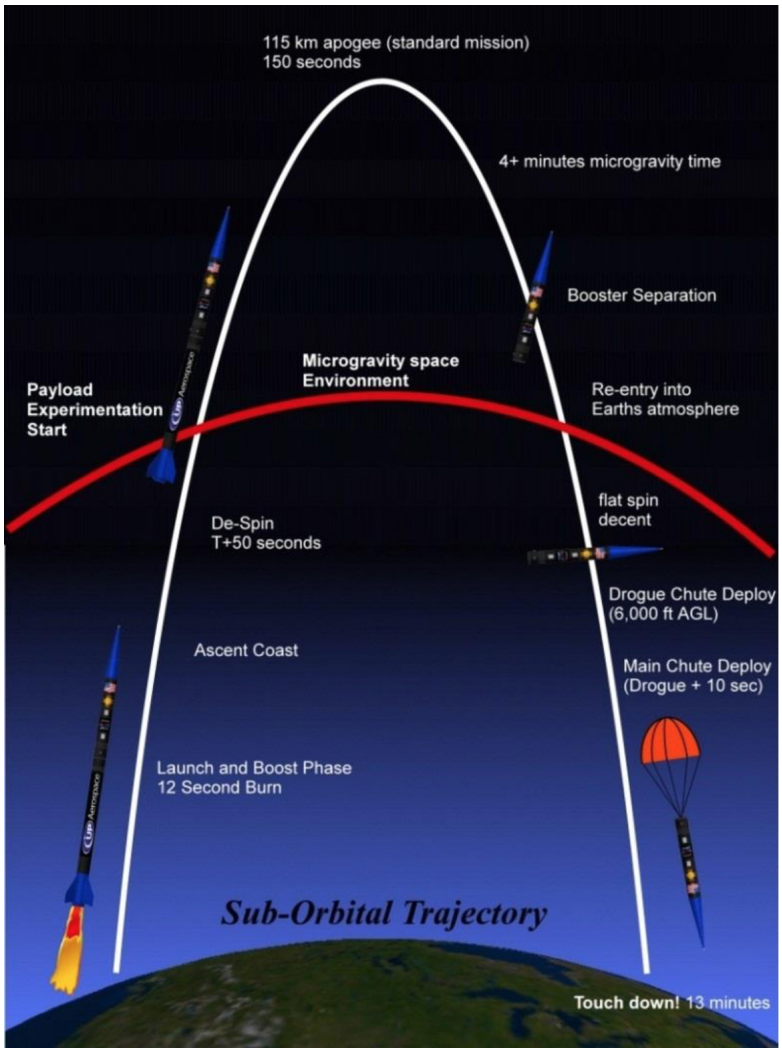

Figure A.1: Typical flight profile of the sub-orbital vehicle. Extracted from UP Aerospace (2012).

Appendix B

Pressure Measurements for SL-9 Protocol

In this appendix we show all the contours of the pressure measurements taken on the preliminary test cell for the SL-9 experiment preparations. We took pressure measurements for $f = 167$ kHz at 7 different z-planes, and on the plots, the PZT is always on the right and the units are all in kPa. Measurements were taken on $y = -1$, $y = 0$ and $y = 1$, and about 200 points along the x-axis, the figures were generated by means of the countour function in MATLAB.

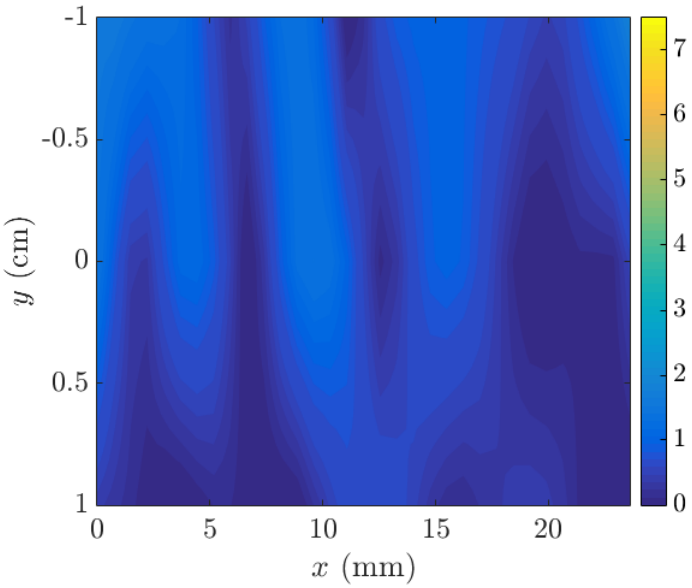

Figure B.1: Pressure contours at 3 cm from the bottom of the test cell.

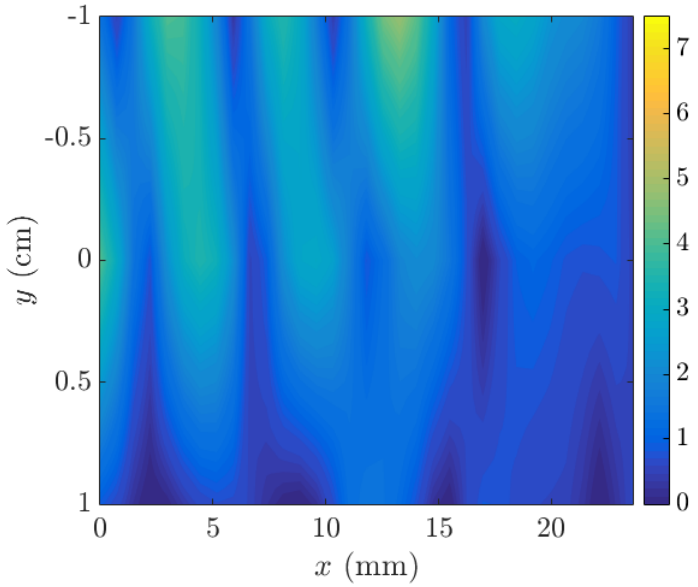

Figure B.2: Pressure contours at 2.5 cm from the bottom of the test cell.

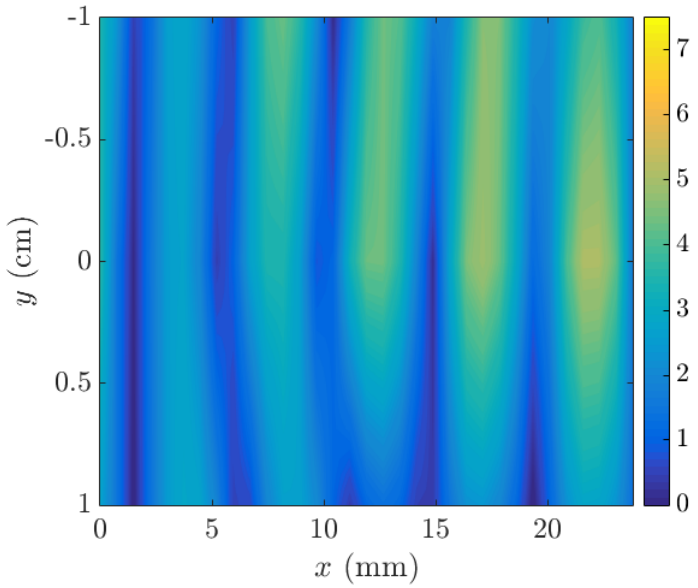

Figure B.3: Pressure contours at 2 cm from the bottom of the test cell.

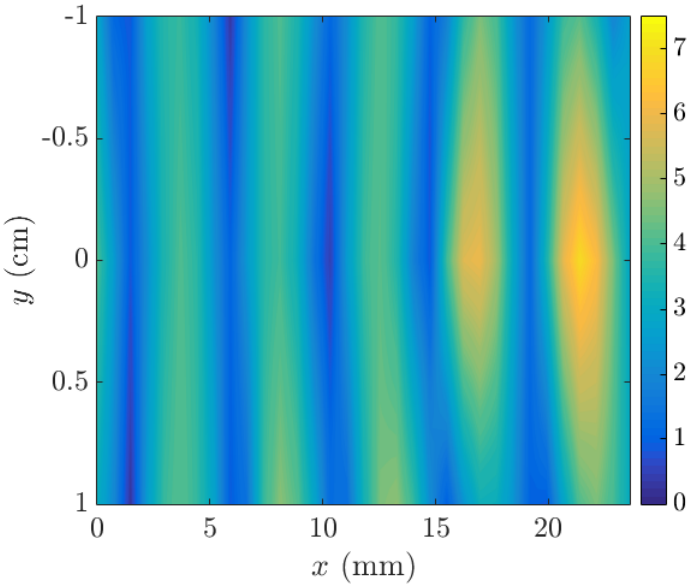

Figure B.4: Pressure contours at 1.5 cm from the bottom of the test cell.

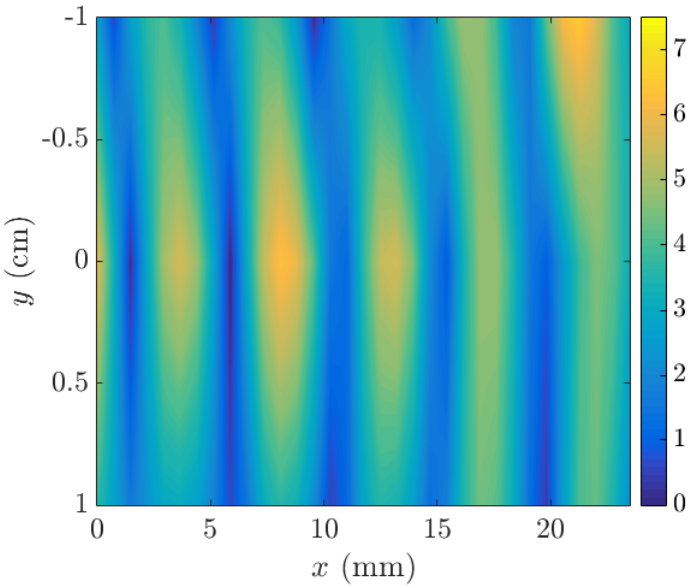

Figure B.5: Pressure contours at 1 cm from the bottom of the test cell.

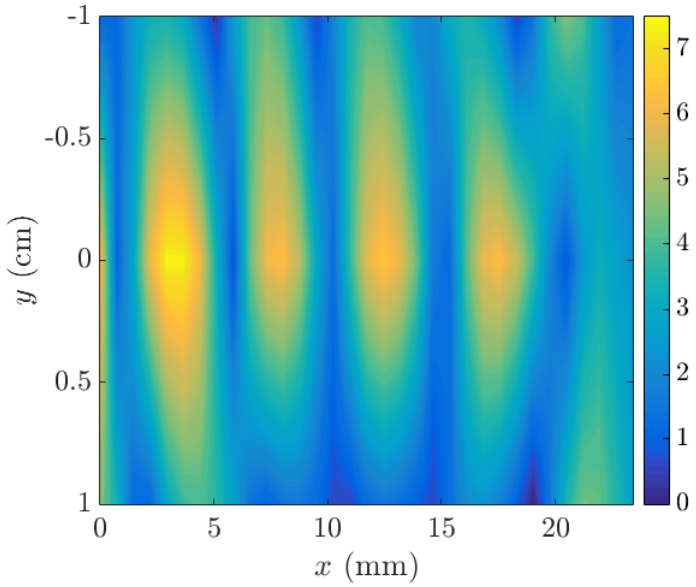

Figure B.6: Pressure contours at 0.5 cm from the bottom of the test cell.

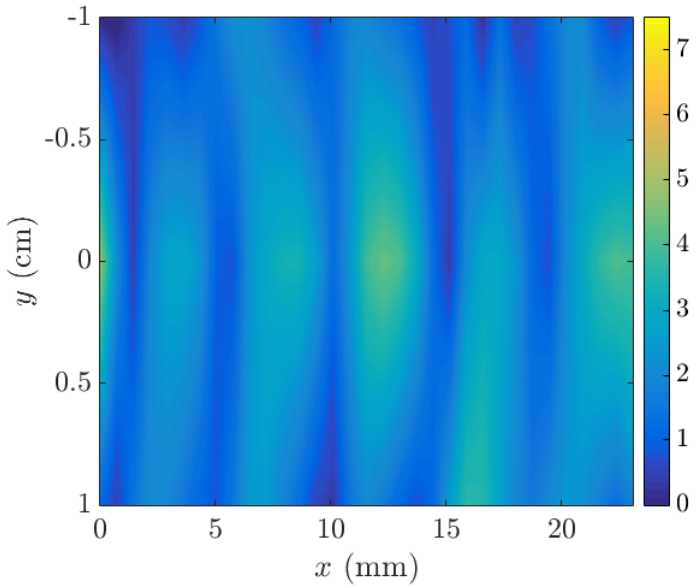

Figure B.7: Pressure contours at the bottom of the test cell.

Appendix C

Numerical Method and Development

C.1 Numerical Method

The fourth order method Runge-Kutta-Gill is used to solve the system of ordinary differential equations 5.14 to 5.17. The method takes into account the round-off error, and it solves

$$u_{i+1} = u_i + \frac{1}{6}(K_1 + K_4) + \frac{1}{3}(bK_2 + dK_3) \tag{C.1}$$

where K_n are parameters defined as

$$K_1 = hf(z_i, u_i) \tag{C.2}$$

$$K_2 = hf(z_i + \frac{1}{2}h, u_i + \frac{1}{2}K_1) \tag{C.3}$$

$$K_3 = hf(z_i + \frac{1}{2}h, u_i + aK_1 + bK_2) \tag{C.4}$$

$$K_4 = hf(z_i + h, u_i + cK_2 + dK_3) \tag{C.5}$$

and

$$a = \frac{\sqrt{2}-1}{2} \tag{C.6}$$

$$b = 1 + \frac{\sqrt{2}}{2} \tag{C.7}$$

$$c = -\frac{\sqrt{2}}{2} \tag{C.8}$$

$$a = 1 + \frac{\sqrt{2}}{2}. \tag{C.9}$$

C.2 Mathematical Development

In order to implement the equations into the code, for convenience, we have separated the different variables as follows

$$\begin{aligned} u(1) &= R & u'(1) &= Q \\ u(2) &= Q & u'(2) &= \frac{\mathrm{d}Q}{\mathrm{d}t} \\ u(3) &= z & u'(3) &= u_b \\ u(4) &= u_b & u'(4) &= \frac{\mathrm{d}u_b}{\mathrm{d}t} \end{aligned}$$

Equation 5.14 as is, needs some work before it can be implemented into the code. There are two terms on the right-hand side of 5.14 that need to be expanded, the Bjerknes force and the added mass force. The Bjerknes force becomes

$$-V\frac{\mathrm{d}P_l}{\mathrm{d}z} = -\frac{4}{3}\pi R^3 k P_{ac}\cos(\omega t)\cos(kz). \tag{C.10}$$

When operating with the added mass force, we obtain

$$\begin{aligned} -\frac{1}{2}\rho_l\frac{\mathrm{d}}{\mathrm{d}t}(Vu_r) &= -\frac{1}{2}\rho_l\frac{\mathrm{d}}{\mathrm{d}t}\left(\frac{4}{3}\pi R^3 u_r\right) \\ &= -\frac{2}{3}\rho_l\pi\frac{\mathrm{d}}{\mathrm{d}t}(R^3 u_r) \\ &= -\frac{2}{3}\rho_l\pi(R^3\frac{\mathrm{d}}{\mathrm{d}t}u_r + \frac{\mathrm{d}}{\mathrm{d}t}R^3 u_r) \\ &= -\frac{2}{3}\rho_l\pi\left[R^3\frac{\mathrm{d}u_b}{\mathrm{d}t} + R^3\frac{kP_{ac}}{\rho_l}\cos(\omega t)\cos(kz) + 3R^2\frac{\mathrm{d}R}{\mathrm{d}t}u_r\right] \end{aligned} \tag{C.11}$$

this equation can be rearranged into two terms, one if which will go to the left-hand side since it contains $\frac{\mathrm{d}u_b}{\mathrm{d}t}$

$$m_b \frac{\mathrm{d}u_b}{\mathrm{d}t} = \underbrace{-\frac{2}{3}\rho_l \pi R^3 \frac{\mathrm{d}u_b}{\mathrm{d}t}}_{\text{To LHS}} - \frac{2}{3}\rho_l \pi \left(R^3 \frac{kP_{ac}}{\rho_l} \cos(\omega t)\cos(kz) + 3R^2 Q u_r \right). \quad \text{(C.12)}$$

Finally, after some minor operations equation C.12 becomes

$$\begin{aligned}(m_b + \frac{2}{3}\pi\rho_l R^3)\frac{\mathrm{d}u_b}{\mathrm{d}t} = & \\ & -\frac{4}{3}\pi R^3 k P_{ac}\cos(\omega t)\cos(kz) \\ & -\frac{2}{3}\rho_l\pi\left(R^3\frac{kP_{ac}}{\rho_l}\cos(\omega t)\cos(kz) + 3R^2 Q u_r\right) \\ & -\frac{1}{2}\rho_l u_r^2 A C_d + V(\rho_l - \rho_g - \rho_v)g. \quad \text{(C.13)}\end{aligned}$$

Equation C.13 is implemented into the code, coupled with the Runge-Kutta-Gill method.

Appendix D

Force Balance FORTRAN Code

```
program main
  implicit none

  character :: filename*60

  print *, 'Write file name for output data, including .dat'
  read *, filename
  open ( unit = 1, file = filename )

  write ( 1, '(2x,a,2x,a,2x,a,2x,a,2x,a)' ) 't', 'R', 'dRdt', 'x', 'ub'
  call timestamp ( )
  write ( *, '(a)' ) ' '
  write ( *, '(a)' ) 'RKG_ForceBalance'
  write ( *, '(a)' ) '  FORTRAN90 version.'
  write ( *, '(a)' ) '  Solve force balance for bubble rising and
     acoustic field.'

    call forcebalance ( )
!
!  Terminate.
!
  write ( 1, '(a)' ) ' '
  write ( 1, '(a)' ) 'RKG_PRB'
  write ( 1, '(a)' ) '  Normal end of execution.'
  write ( 1, '(a)' ) ' '

  write ( *, '(a)' ) ' '
  write ( *, '(a)' ) 'RKG_PRB'
  write ( *, '(a)' ) '  Normal end of execution.'
  write ( *, '(a)' ) ' '
  call timestamp ( )

  close ( 1 )

  stop
```

```
35 end
36
37
38 subroutine forcebalance ( )
39   implicit none
40
41   integer ( kind = 4 ), parameter :: n = 4
42
43   real ( kind = 8 ), parameter :: dt = 5.00D-08
44   external forcebalance_f
45   real ( kind = 8 ), parameter :: pi = 3.141592653589793D+00
46   real ( kind = 8 ) t0
47   real ( kind = 8 ) t1
48   real ( kind = 8 ), parameter :: tmax = 1.0D+00
49   real ( kind = 8 ) u0(n)
50   real ( kind = 8 ) u1(n)
51   real ( kind = 8 ) timer
52
53   write ( 1, '(a)' ) ' '
54   write ( 1, '(a)' ) 'Force Balance'
55   write ( 1, '(a)' ) '  RKGVEC takes a Runge Kutta Gill step for a
       vector ODE.'
56   write ( 1, '(a)' ) ' '
57
58   write ( *, '(a)' ) ' '
59   write ( *, '(a)' ) 'Force Balance'
60   write ( *, '(a)' ) '  RKGVEC takes a Runge Kutta Gill step for a
       vector ODE.'
61   write ( *, '(a)' ) ' '
62
63   t0 = 0.0D+00
64   u0(1) = 0.391D-03      ! ! ! IMPORTANT: Initial radius must match R0
       in subroutine forcebalance_f
65   u0(2) = 0.0D+00
66
67 ! Other starting points options depending on the frequency
68 !0.03443877551 !19.6kHz from 0.45
69 !0.01989796 !19.6kHz from 0.26
70 !0.0308D+00 !14.58kHz start at x/lambda = 0.3
71 !0.022959 !19.6kHz from 0.3
72 !0.03461538 !13kHz from 0.3
73
74   u0(3) = 0.004988967D+00 ! Start from x/lambda = 0.2 for 60kHz
75   u0(4) = 1.00D-20
76   timer = 10000
77
78   do
79 !
80 !  Print (T0,U0).
81 !
82     if ( timer == 10000 ) then
```

```
83        write ( 1, '(2x,g14.6,2x,g14.6,2x,g14.6,2x,g14.6,2x,g14.6)' ) t0,
              u0(1), u0(2), u0(3), u0(4)
84  !       write ( *, '(2x,g14.6,2x,g14.6,2x,g14.6,2x,g14.6,2x,g14.6)' ) t0,
       u0(1), u0(2), u0(3), u0(4)
85        timer = 0
86      end if
87  !
88  !  Stop if we've exceeded TMAX.
89  !
90      if ( tmax <= t0 ) then
91        exit
92      end if
93  !
94  !  Otherwise, advance to time T1, and have RK4 estimate
95  !  the solution U1 there.
96  !
97      t1 = t0 + dt
98      call rkgvec ( t0, n, u0, dt, forcebalance_f, u1 )
99  !
100 !  Shift the data to prepare for another step.
101 !
102     t0 = t1
103     u0(1:n) = u1(1:n)
104     timer = timer + 1
105
106   end do
107
108   return
109 end
110
111 subroutine forcebalance_f ( t, n, u, uprime )
112   implicit none
113
114   integer ( kind = 4 ) n
115
116   real ( kind = 8 ) t
117   real ( kind = 8 ) u(n)
118   real ( kind = 8 ) uprime(n)
119   real ( kind = 8 ) lambda
120   real ( kind = 8 ) w
121   real ( kind = 8 ) k
122   real ( kind = 8 ) Pg0
123   real ( kind = 8 ) Pg
124   real ( kind = 8 ) Pl
125   real ( kind = 8 ) V
126   real ( kind = 8 ) ul
127   real ( kind = 8 ) ur
128   real ( kind = 8 ) A
129   real ( kind = 8 ) Cd
130   real ( kind = 8 ) coeff
131   real ( kind = 8 ) dPldx
```

```
132   real ( kind = 8 ) mb
133   real ( kind = 8 ) Re
134   real ( kind = 8 ), parameter :: pi = 3.141592653589793D+00
135   real ( kind = 8 ), parameter :: eta = 0.8902D-03 ! water dynamic
          viscosity 25Â°C
136   real ( kind = 8 ), parameter :: rho = 997.07D+00 ! rho water 25Â°C
137   real ( kind = 8 ), parameter :: rho_g = 1.1735D+00 ! rho air 25Â°C (
          for 101kPa)
138   real ( kind = 8 ), parameter :: rho_v = 0.77D+00 ! From eq rho =
          0.0022*Pv/T engineering toolbox
139   real ( kind = 8 ), parameter :: Pv = 3.1698D+03 ! water vapor pressure
           at 25Â°C
140   real ( kind = 8 ), parameter :: sigma = 72D-03 ! surface tension  25
          Â°C
141   real ( kind = 8 ), parameter :: ganma = 1.4D+00
142   real ( kind = 8 ), parameter :: Pl0 = 101325D+00 ! atmospheric
          pressure sea level
143   real ( kind = 8 ), parameter :: c = 1496.69D+00 ! Speed of sound in
          water at 25Â°C
144   real ( kind = 8 ), parameter :: f = 60000D+00 ! SYT2012 Axial
          Frequency 60kHz
145   real ( kind = 8 ), parameter :: Pac = 50.0D+03 ! Acoustic pressure
146   real ( kind = 8 ), parameter :: g = 9.81D+00 ! Gravity (1g)
147   real ( kind = 8 ), parameter :: R0 = 0.391D-03     ! ! ! IMPORTANT:
          Change initial radius as required
148
149   w = 2.0D0*pi*f
150   lambda = c/f
151   k = 2.0D0*pi/lambda
152
153   Pg0 = (2.0D0*sigma/R0) + Pl0 - Pv
154
155   uprime(1) = u(2)
156
157   Pg = Pg0*(R0/u(1))**(42./10.)
158   Pl = Pl0 + Pac*cos(w*t)*sin(k*u(3))
159
160   uprime(2) = ((Pg - Pl + Pv - 2.0D0*sigma/u(1))/rho &     ! Rayleigh
          Plesset from Abe2002 and Watanabe1993
161               - 4.0D0*eta*u(2)/(rho*u(1)) &                ! Comment if
                     bubble oscillations neglected
162               - (u(2)**2)*3.0D0/2.0D0)/u(1)
163
164 !  uprime(2) = 0            ! Uncomment if bubble oscillations neglected
165
166   uprime(3) = u(4)
167
168   V = 4.0D0*pi*(u(1)**3)/3.0D0
169   ul = -k*Pac*sin(w*t)*cos(k*u(3))/(w*rho)       ! Abe2002
170   ur = u(4) - ul
171   A = pi*u(1)**2
```

```
172   Re = 2.0D+00*abs(ur)*u(1)*rho/eta
173
174   Cd = 27.0D0*Re**(-78./100.)              ! Crum Cd
175 !   coeff = (1.0D0 + (8.0D0/Re + (1.0D0 + 3.315D0/sqrt(Re))/2.0D0)**(-1))
          ! Mei Cd
176 !   Cd = 16.0D+00*coeff/Re                                  ! Mei Cd
177
178   dPldx = k*Pac*cos(w*t)*cos(k*u(3))
179   mb = 4.0D0*pi*(R0**3)*rho_g/3.0D0     ! According to Mettin2009
180
181   uprime(4) = (-V*dPldx - 2.0D0*pi*rho*((u(1)**3)*k*Pac*cos(w*t)*cos(k*u
          (3))/rho &      ! Force Balance from Abe2002
182                 + 3.0D0*(u(1)**2)*u(2)*ur)/3.0D0 - rho*abs(ur)*ur*A*Cd/2.0
                        D0 &
183                 + (rho-rho_g-rho_v)*g*V)/(mb + 2.0D0*pi*rho*(u(1)**3)/3.0
                        D0)
184
185
186   return
187 end
188
189
190 subroutine rkgvec ( t0, m, u0, dt, f, u )
191   implicit none
192
193   integer ( kind = 4 ) m
194
195   real ( kind = 8 ) dt
196   external f
197   real ( kind = 8 ) f0(m)
198   real ( kind = 8 ) f1(m)
199   real ( kind = 8 ) f2(m)
200   real ( kind = 8 ) f3(m)
201   real ( kind = 8 ) t0
202   real ( kind = 8 ) t1
203   real ( kind = 8 ) t2
204   real ( kind = 8 ) t3
205   real ( kind = 8 ) u(m)
206   real ( kind = 8 ) u0(m)
207   real ( kind = 8 ) u1(m)
208   real ( kind = 8 ) u2(m)
209   real ( kind = 8 ) u3(m)
210   real ( kind = 8 ) a
211   real ( kind = 8 ) b
212   real ( kind = 8 ) c
213   real ( kind = 8 ) d
214   real ( kind = 8 ) k1(m)
215   real ( kind = 8 ) k2(m)
216   real ( kind = 8 ) k3(m)
217   real ( kind = 8 ) k4(m)
218
```

```
219 ! Define constants
220   a = (dsqrt(2.0D0)-1D0)/2.0D0
221   b = (2.0D0-dsqrt(2.0D0))/2.0D0
222   c = -dsqrt(2.0D0)/2.0D0
223   d = 1.0D0 + dsqrt(2.0D0)/2.0D0
224
225 !
226 !  Get four sample values of the derivative.
227 !
228   call f ( t0, m, u0, f0 )
229
230   t1 = t0 + dt / 2.0D0
231   k1(1:m) = dt*f0(1:m)
232   u1(1:m) = u0(1:m) + k1(1:m) / 2.0D0
233
234   call f ( t1, m, u1, f1 )
235
236   t2 = t0 + dt / 2.0D0
237   k2(1:m) = dt*f1(1:m)
238   u2(1:m) = u0(1:m) + a*k1(1:m) + b*k2(1:m)
239
240   call f ( t2, m, u2, f2 )
241
242   t3 = t0 + dt
243   k3(1:m) = dt*f2(1:m)
244   u3(1:m) = u0(1:m) + c*k2(1:m) + d*k3(1:m)
245
246   call f ( t3, m, u3, f3 )
247
248   k4(1:m) = dt*f3(1:m)
249
250
251 !
252 !  Combine them to estimate the solution U at time T1.
253 !
254
255   u(1:m) = u0(1:m) + (k1(1:m) + k4(1:m))/6 + (b*k2(1:m) + d*k3(1:m))/3
256
257   return
258 end
259
260
261
262 subroutine timestamp ( )
263   implicit none
264
265   character ( len = 8 ) ampm
266   integer ( kind = 4 ) d
267   integer ( kind = 4 ) h
268   integer ( kind = 4 ) m
269   integer ( kind = 4 ) mm
```

```
  character ( len = 9 ), parameter, dimension(12) :: month = (/ &
    'January  ', 'February ', 'March    ', 'April    ', &
    'May      ', 'June     ', 'July     ', 'August   ', &
    'September', 'October  ', 'November ', 'December ' /)
  integer ( kind = 4 ) n
  integer ( kind = 4 ) s
  integer ( kind = 4 ) values(8)
  integer ( kind = 4 ) y

  call date_and_time ( values = values )

  y = values(1)
  m = values(2)
  d = values(3)
  h = values(5)
  n = values(6)
  s = values(7)
  mm = values(8)

  if ( h < 12 ) then
    ampm = 'AM'
  else if ( h == 12 ) then
    if ( n == 0 .and. s == 0 ) then
      ampm = 'Noon'
    else
      ampm = 'PM'
    end if
  else
    h = h - 12
    if ( h < 12 ) then
      ampm = 'PM'
    else if ( h == 12 ) then
      if ( n == 0 .and. s == 0 ) then
        ampm = 'Midnight'
      else
        ampm = 'AM'
      end if
    end if
  end if

  write ( 1, '(i2,1x,a,1x,i4,2x,i2,a1,i2.2,a1,i2.2,a1,i3.3,1x,a)' ) &
    d, trim ( month(m) ), y, h, ':', n, ':', s, '.', mm, trim ( ampm )
  write ( *, '(i2,1x,a,1x,i4,2x,i2,a1,i2.2,a1,i2.2,a1,i3.3,1x,a)' ) &
    d, trim ( month(m) ), y, h, ':', n, ':', s, '.', mm, trim ( ampm )

  return
end
```

rkg_forcebalance.f90